MCCXXII

UNIVERSITÀ DEGLI STUDI DI PADOVA

DIPARTIMENTO DI FISICA ED ASTRONOMIA "G. GALILEI"

CORSO DI LAUREA MAGISTRALE IN FISICA

TESI DI LAUREA MAGISTRALE

Space and Time Clustering of High-Energy Photons detected by the *Fermi*-LAT

Laureando:
Giacomo PRINCIPE

Relatore:
Prof. Denis BASTIERI

Correlatore:
Dott. Sara BUSON

Anno Accademico 2014-2015

Contents

Abstract

Since its launch in 2008, the *Fermi* γ-ray telescope has spent $\sim 95\%$ of its time in all-sky-survey mode, in which the Large Area Telescope (LAT) scans the entire sky every two orbits, or approximately every 3 hours (Atwood et al. 2009 [16]). For each detected event are recorded the informations on location, time and energy. They result in a large, multi-dimensional database which provides you a wealth of information about the γ-ray sky.

The release of the new *Fermi*-LAT data, processed with the last Instrument Response Function (PASS8), has encouraged the *Fermi* collaboration to product new catalogs of sources at high energies. Among these catalogs there are the 3LAC (included in 3FGL catalog) and the 2FHL, both are objects of study and revision in my thesis. The method used to create these data set relied on wavelet-based algorithms. The source candidates were detected as fluctuations above the background. These were then followed up with a full likelihood analysis. However, in the last two decades and over many disciplines, there has been a substantial amount of work on clustering analysis as a major statistical technique for classifying large data sets into meaningful subsets.

In my thesis' work I developed and performed a clustering analysis to search new high energy sources. I chose to apply the clustering to the photons detected, between 50 GeV and 2 TeV, by the Fermi-Large Area Telescope (LAT) in 78 months of data.

The possibility of increasing the known VHE γ-ray population of TeVCat2 active galactic nuclei (AGN) is attractive, particularly in the light of framing the scientific priorities for the forthcoming Cherenkov Telescope Array (CTA; Actis *et al.* 2011 [12]).

Chapter 1 presents the objective of my thesis and the importance of my analysis: the space and time clustering.

Chapters 2 and 3 show the basics to understand the results presented in my thesis. Experienced readers in the field could skip them and go directly to the second part of the thesis.

Chapter 2 provides an overview about the *Fermi*-LAT data analysis, which presents the γ-ray data and the analysis methods.

Chapter 3 gives a general introduction, combined with main observed properties and interpretations, of AGNs.

Chapter 4 focus on the last *Fermi*-LAT catalogs: the 3LAC catalog and the 2FHL one. The 3LAC catalog, containing all the Active Galactic Nuclei detected by the LAT telescope in the first 4 years of observation, raised suspicions about the apparent anisotropy of BL LACs (the main class of AGN observed by *Fermi*-LAT) between the northern hemisphere and the southern one. This appears to be at odds with the cosmological principle, which says that the Universe is homogeneous and uniform at a large scale, as really are the observed AGNs. By means of a statistical analysis we found an explanation for this observation anisotropy. The 2FHL catalog, instead, encompasses the celestial sources emitting high energy photons, observed by the LAT during the first 80 months of observation (from September 2008 to May 2015). It extends the upper energy of the observed photon from 300 GeV to 2 TeV, which was made possible by the PASS8 IRF and provide a list of sources with emission from 50 GeV to 2 TeV. It was a starting point for the following space and time analysis, to check the efficiency of the clustering algorithm.

The last part of my thesis focus on the space and time analysis of high energy photons detected by the *Fermi*-LAT.

Chapter 5 describes the sliding window clustering. It explains: the clustering algorithm and and its parameters, the python programs, the comparison with the 2FHL catalog, and the likelihood analysis.

Chapter 6 shows the results of the Clustering analysis. In the first part there are the results of the Unbinned Likelihood of the clusters that didn't find association in the 2FHL catalog. The second part presents the flare phenomena of the Crab Nebula and the Markarian 421. In the last part there are the conclusions and the outlook of my thesis' work.

Chapter 1

The objective of my thesis

My thesis' work is inspired by the latest developments on the analysis data of the *Fermi*-Large Area Telescope. The output of the last Instrument Response Function (PASS8), thanks to the extended set of event-level reconstruction algorithms, allowed a considerable improvement of the performance of the instrument. It also led to greater accuracy, extending toward higher energies the acceptance of the instrument (see Instrument Response Function 2.2.1).

The release of the new *Fermi*-LAT data processed with PASS8 has encouraged the *Fermi* collaboration to produce new catalogs of sources at high energies. Among these catalogs there are the 3LAC (included in 3FGL catalog) and the 2FHL. Both are objects of study and revision in my thesis (see Chapter 4, the *Fermi*-LAT catalogs).

The objectives of my thesis are:

- to review some analysis by the 2FHL and 3LAC catalogs, and to shed light on their possible gap;
- to seek for new high energy sources;
- to observe the temporal variations of the luminous flux of high-energy sources and to study their flare phenomena.

The 3LAC catalog, containing all the Active Galactic Nuclei observed by the LAT telescope in the first 4 years of observation, raised suspicions about the apparent anisotropy of BL LACs (the main class of AGN observed by *Fermi*-LAT) between the northern hemisphere and the southern one. This appears to be at odds with the cosmological principle, which says that the Universe is homogeneous and uniform at a large scale, as really are the observed AGNs. By means of a statistical analysis I found an explanation for this observation anisotropy (see Chapter 4, BL LACs anisotropy). The 2FHL catalog, instead, encompasses the celestial sources emitting high energy photons, observed by the LAT during the first 80 months of observation (from September 2008 to May 2015). It extends the upper energy of the observed photon from 300 GeV to 2 TeV, which was made possible by the PASS8 IRF and provide a list of sources with emission from 50 GeV to 2 TeV. Sources in this catalog were detected by analysing the whole period of 80 months, tessellating the celestial sphere into Regions of Interest (ROI) with radius of 15°, properly overlapped so as to analyse with care every possible direction.

During my thesis I looked for new, high energy sources in shorter intervals, whose signal could have been diluted during the long 80 months period of the 2FHL. The research of these sources was done by a clustering algorithm in space and time, where the time interval could vary from one day to the whole period of observation (see Chapter 4, Spatial and Time Clustering, and Chapter 6, Clustering Results).

Thanks to the spatial and temporal clustering, it is possible to analyse the variation of the gamma-ray flux of the observed sources and to reconstruct the flares that have occurred. In the center of the AGN there is a super-massive black hole that accrues matter with variable speed: occasionally catastrophic transitions are observed, real earthquakes are resulting in a sudden increase of emitted flux, called flare. The flares from distant galaxies are important for two reasons: they provide indeed informations about the cosmic dynamics and they allow the study of eventual dependencies of the arrival time of the signal with respect to the photon's energy.

The importance of my thesis' work

Thanks to my thesis work, it was possible to clarify the remained doubts on the results obtained by the 3LAC catalog, and to revise and expand the sources' catalog observed by *Fermi*-LAT, in the energy spectrum from 50 GeV to 2 TeV . Of particular importance it is reviewing and widening of the 2FHL catalog for present and future observations of the Universe through the Cherenkov telescopes.

Astrophysics trend is to look at higher and higher energies, namely the observation of high and very high energy γ-rays (HE and VHE), through the use of ground-based telescopes that exploit the Cherenkov effect, analysing the electromagnetic showers produced by the interaction of γ-rays with the atmospheric nuclei.

The Large Area Telescope on board the *Fermi* satellite has been efficiently surveying the GeV sky detecting over 3000 sources in just four years of exposure (see the 3FGL catalog). These sources are detected in the 0.1 GeV $\div$ 2 TeV band and, given *Fermi*'s peak sensitivity at $\sim$1 GeV, they are representative of the GeV sky. On the other hand, Cherenkov telescopes, with their good angular resolution and excellent point-source sensitivity, but a rather small field of view, have been exploring only small patches of the $>$50 GeV sky. The aim of my work is to close this gap between ground-based Cherenkov telescopes and all-sky observations at GeV energies from orbit.

The energy band ranging from 50 GeV to 2 TeV, used in the production of the 2FHL catalog and in my analysis, coincides with the spectrum of energies that is observed by the *Fermi*-LAT and as well by various Cherenkov telescopes.

The Cherenkov telescopes are affected by an intrinsic systematic uncertainty which affect both the energy and the flux scale, due to the fact that they can not be calibrated. Instead this has been possible for the LAT, calibrated at accelerator facilities. It is therefore of great importance to rely on a good catalog of sources in those energies, in particular for a possible calibration of Cherenkov telescopes through the use of *Fermi*-LAT data (>50 GeV).

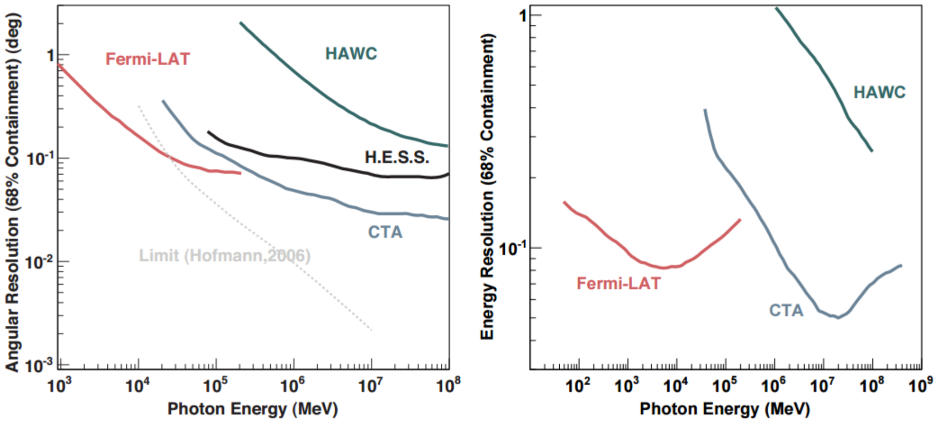

Figure 1.1: Left: Angular resolution for *Fermi*-LAT and CTA. H.E.S.S. and HAWC are shown as examples for a current-generation IACT and for a next-generation water Cherenkov detector. Also shown is the limiting angular resolution that could be achieved, if all Cherenkov photons emitted by the particle shower could be detected. Right: Energy resolution for *Fermi*-LAT and CTA. Shown is the 68% containment radius around the medium interval of the reconstructed energy. It is evident that the energy resolution of Fermi-LAT in the overlapping energy range is significantly better than the CTA resolution.

Figure 1.1 shows the comparison between the energy and angular resolution of the two different telescopes: the *Fermi*-LAT, which exploits the phenomenon of pair production to measure the gamma rays, and the Cherenkov Telescopes.[1]

---

[1] http://arxiv.org/abs/1205.0832v1 - Comparison of *Fermi*-LAT and CTA in the region between 10-100 GeV S. Funk, J. A. Hinton for the CTA Collaboration. [32]

Chapter 2

Fermi Gamma-Ray Space Telescope

The *Gamma ray Large Area Space Telescope* (GLAST) satellite was successfully launched on 11 June 2008. It is orbiting around Earth at an altitude of ~ 565 km and with an orbital inclination of $25.6°$. It was then renamed as *Fermi Gamma Ray Space Telescope* after starting its scientific mission on 11 August 2008.

The aim of the mission is to observe the sky in the gamma-ray energy band. In particular the main objectives are:

- to explore the most extreme environments in the Universe, where nature harnesses energies are far beyond anything possible on Earth;
- to determine the origin of the diffuse gamma-ray background and the nature of the unidentified sources;
- to study the process of particle acceleration which produce the high energy emission for Galactic and extragalactic sources;
- to study the energy of the Gamma-Ray Burst;
- to search for signs of new laws of physics and what composes the mysterious Dark Matter;
- to explain how black holes accelerate immense jets of material to nearly light speed;
- to answer long-standing questions across a broad range of topics, including solar flares, pulsars and the origin of cosmic rays;
- to constrain the Extragalactic Background Light (EBL) that is responsible of the absorption of the highest energy photons.

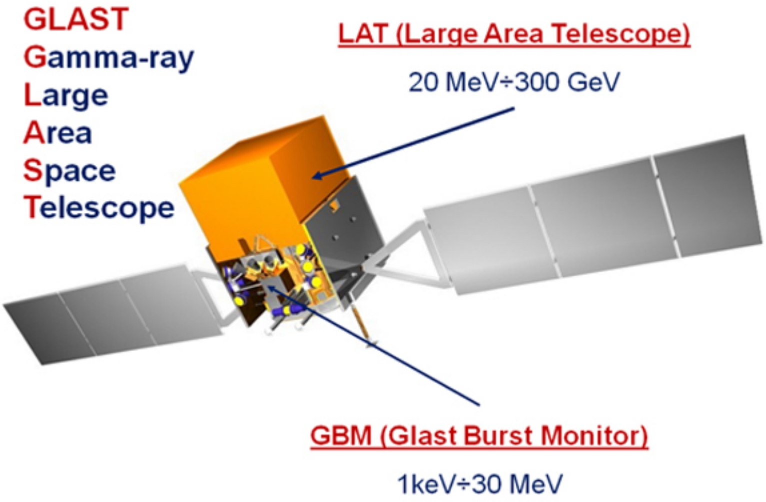

Figure 2.1: The *Fermi* satellite with the position of its two instruments: the LAT and GBM.

With its two instruments, the LAT telscope has an energy coverage that goes almost continuously from 8 keV to 300 GeV (until 2 TeV with the new Pass8). This makes the *Fermi* satellite a fundamental instrument to connect the X-ray observations with the data taken in the TeV band by ground-based Cherenkov Telescope.

The *Fermi* spacecraft operates in a number of observing modes. Transitions between modes may be operated from ground or autonomously by the spacecraft. The primary observing mode for *Fermi* is *survey mode*, where the satellite scans the whole sky. During the orbit it sweeps the sky from the local zenith to the celestial pole with an angle named *rocking angle*. At the end of each orbit, the satellite turns on the other side of the orbital plane and continues the observations looking the other hemisphere in the same way.

Uniformity of exposure is achieved by *rocking* the pointing perpendicular to the orbital motion. The default profile rocks the instrument axis 35 degrees north for one orbit, then 35 degrees south for one orbit, resulting in a two-orbit periodicity (one orbit lasts around 90 minutes). The maximum rocking angle is 60 degrees. The current rocking angle is 50°. Therefore thanks to the large field of view, *Fermi* can observe uniformly the sky every 3 hours. However, it occasionally operated in pointing mode to study interesting transient phenomena like Gamma-Ray Burst. After a pre-determined time the spacecraft is set to return to the scheduled mode. Currently the duration for such autonomous repointing is five hours. The pointing accuracy is <2 degrees (1σ, goal of <0.5 degrees), and the uncertainty of the pointing is <10 arcsec (goal <5 arcsec).

The spacecraft has two instruments onboard as shown in Figure 2.1:

- The *Gamma-Ray Burst Monitor* (GBM) that observe the band 8 keV - 40 MeV
- The *Large Area Telescope* (LAT) with an energetic range that goes from 20 MeV - 2 TeV

The GBM is dedicated to the analysis of transient sources like Gamma Ray Burst and transient phenomena. It is made by two different kind of scintillations detectors with a time resolution of 2 μs. There are 12 Sodium Iodide (NaI) disks, each one connected directly with a photomultiplier tube (PMT) and covering an energy range that goes from 8 keV to 1 MeV. Moreover, there is also a pair of Bismuth Germanate (BGO) cylinders, each of them with two PMTs connected, sensitive in a band from 150 keV to 40 MeV of energy, providing also an overlap with the NaI detectors. Three NaI detectors are located in each corner of the spacecraft, oriented in different direction for a better sky coverage. The BGO cylinders are instead on the opposite side of the satellite.

The LAT is a pair conversion telescope and it is the principal instrument of the spacecraft. With its large field of view (2.4 sr), in a single orbit it can cover 75% of the sky. The details of this telescope will be seen in the following section.

2.1 The Large Area Telescope

The Large Area Telescope (LAT) is a pair conversion detector. The principal objective is to conduct a long-term high-sensitivity γ-ray observations of celestial sources in the energy range from $\sim$20 MeV to $>$300 GeV. The LAT is a wide Field-of-View (FoV) imaging γ-ray telescope with large effective area combined with good energy and angular resolution. Its key feature is the wide effective area for the e^+e^- pairs production in the interaction of gamma photons with matter.

The LAT data have being used for:

- rapid notifying of γ-ray transient events and monitoring of variable sources
- constructing a catalog of celestial γ-ray sources along with spectra of several hundred of these sources
- localizing point sources to 0.3 - 2 arcmin
- spatial mapping and spectra of extended sources such as supernova remnants, molecular clouds, and nearby galaxies
- measuring the diffuse γ-ray background

- searching for signals from dark matter
- measuring the flux and spectrum of cosmic ray electrons.

The LAT is a pair conversion detector: γ-rays penetrate into the detector (the tracker) and interact with a high Z converter material, in this case tungsten, to produce an electron-positron pair (Atwood et al., 2007 [15]). This pair is tracked through the instrument by silicon strip detectors. Since the γ-ray energy is much larger than the rest mass of the electron and positron, both particles will travel predominantly in the direction of the incident photon. So the reconstructed direction on the incoming γ-ray is limited by multiple scatterings of the pair components in the tracker material, as well as the spatial resolution of the tracker. At the bottom of the LAT there is a calorimeter made of CsI (Tl) that is thick enough to provide an adequate energy measurement of the pairs in the LAT energy band.

2.1.1 LAT Structure

The LAT (Atwood et al., 2009 [16]) is an imaging, wide-field-of-view, γ-ray telescope, detecting photons from 20 MeV to more than 300 GeV. The instrument is a pair-tracking telescope, composed by a 4×4 array of towers (measuring 43.25 cm × 43.25 cm × 84 cm). They are inserted into an aluminium grid, the structural backbone of the instrument, which also conducts heat away to the radiators. A segmented anti-coincidence detector (ACD) covers the tracker array. In each tower a converter-tracker module is located on top of the corresponding calorimeter module, while on the bottom the Tower Electronics Modules (TEM) are placed with a programmable trigger and Data Acquisition System (DAQ). A foam thermal blanket surrounds everything, providing a light-tight cover and preventing damage by micro-meteor hits. Figure 2.2 provides a schematic illustration of the LAT.

The anti-coincidence detector The anti-coincidence detector is the first defence of the LAT against the large background given by charged cosmic rays. In fact it has the role to discriminate between photons and charged particles, the latter have a flux over five order of magnitude bigger than the gamma photon flux.

The shielding is made of segmented plastic scintillator in polyvinyltoluene (PVT) with 89 sections, each one connected through wavelength-shifting fibers to 2 PMTs. The design efficiency, in the rejection of unitary charged particles, is 99.97%, averaged on the 8.6 m^2 of the detector surface.

The structure is segmented to reduce the problem "self-veto", due to the *backsplash* effect, that is the rejection of a true photon caused by the escape of charged particles, originated in the electromagnetic shower, that crosses the ACD. This leads to a reduced efficiency in the detection of high energy photons, which easily undergo backsplash effect.

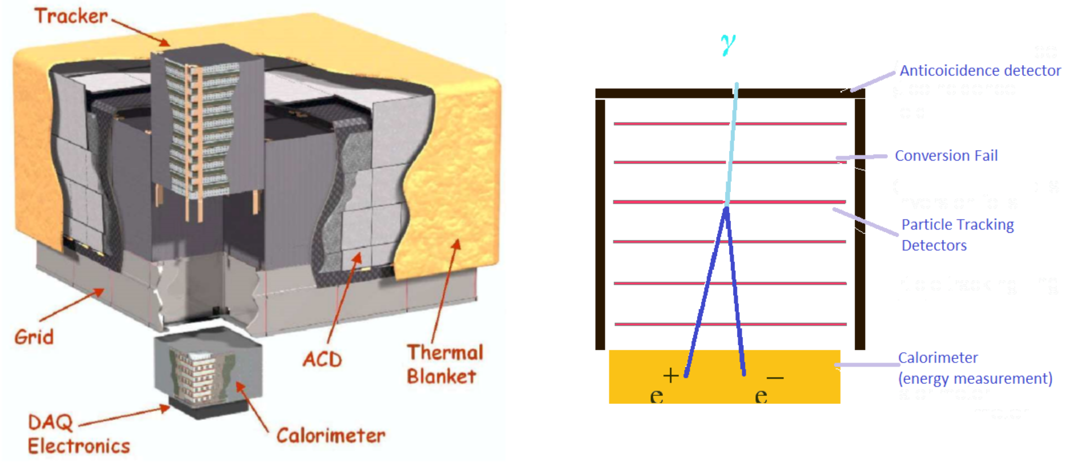

Figure 2.2: Structure of the Large Area Telescope. Its real dimensions are 1.8 m × 1.8 m × 0.72 m.

The tracker When a gamma-ray crosses the instrument, the tracker has two different aims: it has to convert the photon in a e^+e^- pair and to reconstruct the particles path to obtain the original photon trajectory. In order to do this, there is an array of 4×4 columns of 40×40 cm^2 with 18 trays in a carbon structure. The first 16 trays are made of 2 silicon strips detectors (SSD) in $x - y$ configuration, each one with 384 detection strips with a pitch of 228 μm, spaced by a tungsten foil. This metal has an atomic number $Z = 74$, in order to have enough pair production cross section (that is increasing as Z^2). Counting from the top of the LAT, the first 12 layers (the front part) have a metal foil of a thickness of 0.03 radiation lengths, the tungsten in the subsequent 4 trays (the back part) is instead 0.18 radiation lengths. The last 2 layers have no metal foils. The aim of this distinctions is that the front part maintain a good PSF (Point Spread Function) for the low energy photons. The back part extends the effective area with a loss of angular resolution due to Compton multiple scattering. The lack of the metal in the last 2 layers has instead the purpose to have a good spatial resolution of the entry point of the particles calorimeter.

The calorimeter Inside the tower is positioned a calorimeter module of 96 CsI crystals doped with Thallium. These are arranged in an eight-layer hodoscopic configuration so that each layer is rotated by 90° with respect to the previous one, forming an $x - y$ array. A calorimeter module is thus segmented in both depth and lateral directions to improve energy resolution, with a total thickness of $\sim$8.6 radiation lengths. Crystals are read out by photo-diodes at each sides, giving both longitudinal and transverse information about the energy deposition pattern. Each crystal provides three spatial coordinates: two discrete coordinates from the location of the crystal in the array and the third coordinate given by measuring the light yield asymmetry at the ends of the crystal along its long dimension.

The calorimeter provides the measurement of the energy deposited by the shower initiated by the e^+e^- pairs, and it also images the shower development, enabling the estimation of the energy leakage and discrimination of hadronic showers.

The DAQ The trigger and readout phase are managed by the Data Acquisition System. This module has also the duty to filter collected data, reduce the transmission event rate and provide a quick answer to transient phenomena. The LAT's DAQ performs onboard filtering in order to reduce the rate of background events that will be telemetered to the ground. The DAQ processes the captured event data into a data stream with an average bit rate of 1.2 Mbps for the LAT. The DAQ also performs the command control, instrument monitoring, housekeeping, and power switching. Onboard processes can be modified by uploading new software, if necessary.

The trigger The global trigger merges the primitive triggers of the tracker and the calorimeter. The trigger can be issued if there is a signal from at least three $x - y$ planes in a row. The calorimeter has instead two primitive triggers, the CAL-LO when is a single calorimeter log there is an amount of released energy > 100 MeV, and the CAL-HI when the amount of released energy is greater than 1 GeV.

From the ACD have two types of discriminating signals. The first is a simple signal with a threshold of 0.4 MIPs used as a possible veto on the tracker primitives. These signals can be grouped in a Region of Interest (ROI) to individuate a charged particle signal near a triggering tower. The second, a high level discriminated signal, has instead a threshold of 20 MIPs. It is generated by heavy nuclei of carbon, nitrogen and oxygen (CNO) and it is used for calibration purposed.

In addition to the *physical* triggers, there is also a periodic trigger, used to monitor the performance of the instruments.

2.2 Event Reconstruction and Classification

The event analysis process, performed on ground, starts as soon as data are downlinked to Earth. If one considers that the LAT detects several hundred events every second, this is particularly challenging as you have to transform the individual channel signals into a particle interaction pattern.

The main steps can be summarized as follows:

- Data are decompressed and individual channels information are converted to more physically motivated pattern (e.g. grouping signals in the ACD by tile).

- The reconstruction of the event is achieved applying pattern recognition and fitting algorithms commonly used in high energy particle physics experiments. Individual tracker tracks and energy clusters in the calorimeter are correlated to signals in the ACD.

- Figures of merit for the event are evaluated from the collections of tracks and clusters and then associated to the ACD information. Afterwards multivariate analysis techniques aim to determine the energy and direction of the event and to construct estimators that the event is in fact a γ-ray interaction.

- Event selection criteria are applied to populate the various γ-ray event classes.

In addition to these procedures, the processing pipeline automatically verifies the data integrity at each step and provides all the ancillary data products related to calibration and performance monitoring of the LAT.

The development of the analysis process initially was based and strongly relied on detailed Monte Carlo (MC) simulation of the instrument. During the first years of the mission the LAT team has gained considerable insight into the in-flight performance of the instrument. Accordingly, the experience accumulated with real data after launch has been exploited for updating the LAT data reduction. More the Instrument Response Functions (IRFs), which provide the description of the instrument performance used for data analysis, have been later corrected for discrepancies observed between flight and simulated data. I note that part of this thesis work makes use of the event analysis elaborated prior to launch known as PASS8.

LAT Monte Carlo modelling Fundamental, in the pre-launch phase for the design of the instrument and the development of the software infrastructures, are the Monte Carlo simulations. The MC modelling of the LAT has been crucial for both the event analysis and the studies of the instrument performance.

Validation of MC modelling of the LAT was performed through an on-ground calibration with muons and a beam-test campaign on a "calibration unit", made with detector modules with the same characteristics of those used to build the LAT, including two complete tracker/calorimeter towers. The calibration unit was exposed to photons (up to 2.5 GeV), electrons ($1 \div 300$ GeV), hadrons (π and p, from a few GeV to 100 GeV) and ions (C, Xe, 1.5 GeV/n) in different irradiation facilities (Baldini et al., 2007 [18]).

Parallel to the on-ground calibration, a further more detailed calibration was scheduled to be carried out in orbit. The calibration effort started after *Fermi* launch and the first results are provided in detail in Abdo et al.

(2009). The LAT performance was fine-tuned by optimizing internal delays and synchronizations, alignment constants and absolute timing.

Track and energy reconstruction Clusters of spatially adjacent hits in the tracker are combined to determine a three dimension position in the detector thus generating track hypotheses. Two different algorithms are used to generate tracks. The first is based on the centroid and axis of the energy deposition in the calorimeter. The furthest cluster is taken randomly in the appropriate temporal window; the second one is searched for on the line connecting the putative first hit to the deposition centroid in the calorimeter.

Concerning the energy reconstruction, at first raw signals are converted into energy depositions for each crystal end. In this way they provide the total energy and the hit position for each crystal, thus resulting in a three dimension array of energies. The sum of the energies deposited provides the first raw estimate of the event energy, while the the direction of the shower is derived from the 3D centroid and higher moments of the energy deposition.

The energy reconstruction starts by reading the position and the amount of energy released in each log of calorimeter. The first estimate is done summing all the energies released in the calorimeter, then, three different algorithms are correcting this rough estimate using the information obtained by the track reconstructions:

- a Parametric Correction (PC), based on the barycentre of the shower;
- a Shower Profile (SP) fit, which takes into account the longitudinal and transversal development of the shower and it is fully operative for energies greater than 1 GeV.
- a maximum likelihood method (LK) which correlates the information of the energy deposit in the tracker, considered as a segmented part of the calorimeter.
- the final step is to take into account the Instrument Response Function (IRF).

Event classification and Background rejection The purpose of the event classification is not only the estimate of the best event direction and energy, among those available for each event, together with their accuracy, but also the reduction of the background in the final data sample. For these aims a series of selection criteria and classification tree generated probabilities (Breiman,1984 [20]) are used.

For the determination of the direction, at first, a classification tree selects between the vertex solution, if available, and the best one-track solution. Events are then divided into four subclasses, according to the conversion point, in the front or back section of the tracker, and to the vertex properties, namely vertex or one-track events. At the end of the process a best energy and a best direction measurements are assigned to each event, along with the corresponding estimates of the accuracy of the measurements.

After energy and direction are selected, an additional background rejection stage is applied, improving the on-orbit filtering. The on-board filter is configured in order to reduce the data to fit the available band for data downlink at the Earth while keeping the largest possible efficiency for γ-ray detection (reducing the signal-to-noise ratio at $\sim 1 : 300$). On ground, informations from all LAT subsystems, are examined in detail and several figures-of-merit are evaluated using automated data-mining techniques.

The final outcome of the on-ground event analysis is the energy and direction for the event, with corresponding confidence levels, along with several estimates of the probability the event describes, after all, a γ-ray and not a background particle. All the described ingredients are used to define standard event classes optimized for a range of scientific objectives and, at the same time, accounting for an obvious trade-off between efficiency, purity and resolution.

The main event classes defined prior to launch and used in for the PASS8 dataset are the following:

- The *Transient* class, suitable for studying localized, intense, transient phenomena (e.g. Gamma-ray Bursts), has the largest efficiency at the expense of a high residual background rate;

- The *Source* class, suitable for study of localized sources with a residual background rate comparable to the extragalactic diffuse rate estimated from EGRET.

- The *Diffuse* class, expected to achieve a background-rejection factor of the order of 10^6, while keeping an efficiency for γ-ray detection $\sim 80\%$. The name derived by its specific aim to study diffuse γ-ray emission

2.2.1 The LAT Instrument Response Function

In the High Energy Astrophysics, the Instrument Response Functions (IRFs), conventionally represent a high-level model of the instrument response that enable the data analysis (IRFs; e.g. Davis, 2001 [25]). The main reasons for these are twofold:

- instrument analysis is complex and can be hardly managed by the "external" astrophysics community. Therefore only few useful estimated quantities (e.g. energy, direction, inclination angle with respect to the telescope axis) are provided;

- data from different instruments in different energy ranges can be compared, allowing a multi-wavelength analysis.

Canonically the detector response is factored into three terms: efficiency in terms of the detect or effective area, resolutions as Point Spread Function (PSF) and energy dispersion. The LAT IRFs were defined and parametrized prior to launch based on the MC simulations. The IRFs were subsequently updated to take into account effects measured in flight that were not considered in pre-launch performance estimates (Pass8).

The issues were primarily pile-up and accidental coincidence effects in the detector subsystems leave *ghost* signals in coincidence with good photon triggers.

IRF definition

The LAT performance is governed primarily by:

- LAT hardware design
- Event reconstruction algorithms
- Background selections and event quality selections

A result of the performance analysis is the production of full Instrument Response Functions (IRFs), describing the performance as a function of photon energy, incidence angle, conversion point within the instrument, and other important parameters. The IRF is the mapping between the incoming photon flux and the detected events. 'Detection' depends not only on the LAT hardware but also on the processing that calculates the event parameters from the observables and assigns probabilities that an event is a photon. Indeed, the different event cuts are based on tradeoffs between the non-photon background, the effective area and the spatial and energy resolution; the effect of these cuts should be considered in the analysis.

To evaluate the LAT response, a dedicated Monte Carlo simulation is performed. A large number of gamma-ray events are simulated in order to cover all possible photon inclination angles and energies with good statistics. This is based on the best available representation of the physics interactions, the instrument, and the on-board and ground processing are used to produce event classes. The comparison between the properties of the simulated events within a given event class and the input photons gives the Instrument Response Functions.

The IRF is factored into three terms: efficiency in terms of the detector's effective area, resolution as given by the point-spread function (PSF), and energy dispersion.

Conventionally IRFs are defined as a function R of true photon energy E' and direction $\hat{p}'$, measured photon energy E and direction $\hat{p}$ and time t. As a matter of fact the differential count rate in the instrument phase space (reconstructed energy and direction) is given by the convolution of the source differential flux per unit area at the detector with the IRFs.

$$\frac{dN}{dtdEd\hat{p}}(E,\hat{p},t) = \int dE'd\hat{p}'R(E,\hat{p}|E',\hat{p}',t)\frac{dN}{dtdE'd\hat{p}'dS}(E,'\hat{p}',t) \qquad (2.1)$$

The IRFs are factorized into three functions, representing the efficiency, the angular resolution and the energy resolution plus a temporal scaling factor.

$$R(E,\hat{p}|E',\hat{p}',t) = T(t)A(E',\hat{p}')P(\hat{p}|E',\hat{p}')D(E|E',\hat{p}') \qquad (2.2)$$

$T(t)$ is a scaling factor which accounts for temporal variations, such as instrument failures, temporary switching off, thermal expansion or the deterioration of instrument components. Noteworthy, the lack of consumables makes the LAT performance remarkably stable and therefore this term can be considered equal to 1. The three functions describing the IRFs are:

- the *effective area*, $A(E',\hat{p}')$, which is the detection efficiency for photons of true energy E' and arrival direction $\hat{p}'$ expressed as an area;

- the *PSF*, $P(\hat{p}|E',\hat{p}')$, the probability density that a photon with energy E' and arrival direction $\hat{p}'$ has a reconstructed direction $\hat{p}$;

- the *energy dispersion*,$D(E|E',\hat{p}')$, the probability density that a photon with energy E' and arrival direction $\hat{p}'$ has a reconstructed energy E.

The LAT IRFs are determined primarily by the hardware design, the event reconstruction algorithms and the event classification and selection. To evaluate the LAT response a dedicated MC simulation was produced before the launch and a huge amount of γ-ray events were simulated to cover with good statistics all possible photon inclinations and energies.

Pass8 There are multiple IRFs delivered with the *Fermi* Science Tools to allow the user the flexibility necessary for the different analysis types. The LAT data currently being released by the FSSC have been processed using the Pass8 event-level analysis. The Pass8 analysis uses an entirely new set of event-level reconstruction algorithms that improve the instrument performance and mitigate pile-up effects.

The main features of the *P8R2_V6* IRFs are:

- Inclusion of second order effects released previously that is the azimuthal and the livetime dependencies.

- Subdivision of IRFs into three event type partitions (FRONT/BACK, PSF, and EDISP). Previous IRF releases were partitioned only by conversion type into FRONT and BACK events.

- No flight-based corrections have been made to the effective area or PSF. Instead in the P7REP the correction created systematic uncertainties in the effective area and the PSF which were less than 5% between 100 MeV and 10 GeV.

- New tables that contain a correction for the bias in the LAT event direction reconstruction (fisheye effect) as a function of energy and incidence angle.

The current event classes are a nested hierarchy in which the higher probability photon selections are subsets of the less restrictive selections. Higher probability photon selections have smaller effective areas, narrower point spread functions (PSF), and lower contamination of background events. In this set of Pass8 data (called P8R2 by the LAT team) the background contamination in each class is calibrated to the best-fit power-law parametrization of the Isotropic Diffuse Gamma-Ray Background (IGRB) emission from Abdo et al. 2010 ([1]).

The loosest selection criteria (the TRANSIENT classes in Pass8) are designed for short duration events, such as gamma-ray bursts, and timing studies that benefit from increased photon statistics while tolerating a higher background fraction and broader PSF. These classes have background fluxes that are generally equal to or greater than the IGRB and are denoted by their background level relative to the A10 reference spectrum (e.g. the background in TRANSIENT020 is 2 times higher than the A10 reference spectrum). The cleaner photon selections (SOURCE through ULTRACLEANVETO classes in Pass8) provide lower background contamination at the expense of lower effective areas (particularly at low energies) and have background fluxes that are generally equal to or lower than the IGRB. An intermediate selection (SOURCE class in Pass8) is most favourable for analysis of moderately extended sources and point sources on medium to long time-scales. The most restrictive selection (the ULTRACLEANVETO class in Pass8) is ideal for analysis of large regions that are more sensitive to spectral features caused by instrumental backgrounds.

In the Pass8 data release the event classes are organized in three nested hierarchies: "Standard", "Extended", and "No-ACD". The Standard hierarchy contains all classes currently recommended for LAT analysis. The Extended classes are defined with a less restrictive fiducial selection that accepts events with projected trajectories that do not pass through the Calorimeter. This selection improves the LAT effective area at low energies and high incidence angles ($<$ 100 MeV and $\theta > 45$ deg) but also slightly worsens the energy resolution. The No-ACD classes are defined using selections that exclude variables associated with the Anti-Coincidence Detector and are therefore less susceptible to X-ray pile-up activity which can occur during the impulsive phase of solar flares. However these classes generally

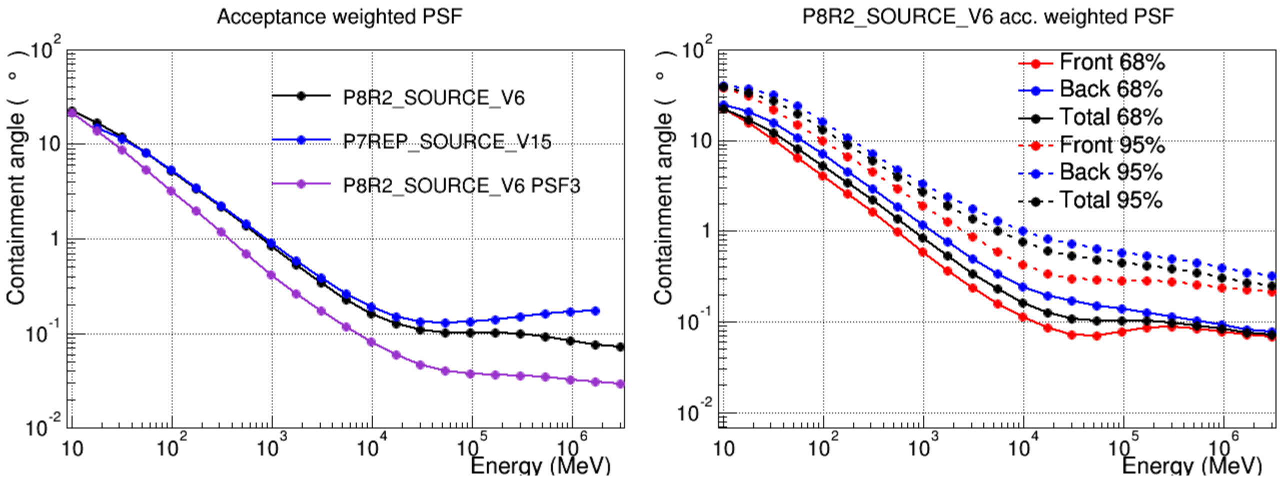

Figure 2.3: These plots correspond to the status of the analysis known as `P8R2_V6`, which has been optimized for the study of point-like sources and the production of the third LAT source catalog (3FGL). On the right there is the plot of 68% and 95% containment angles of the acceptance weighted PSF for the front/back.

have worse performance than the standard TRANSIENT selections when no pileup activity is present.

The list of event classes hierarchies defined in the Pass8 data:

- `P8R2_TRANSIENT010`: Transient event class with background rate equal to one times the A10 IGRB reference spectrum.
- `P8R2_SOURCE`: This event class has a residual background rate that is comparable to `P7REP_SOURCE`. This is the recommended class for most analyses and provides good sensitivity for analysis of point sources and moderately extended sources.
- `P8R2_CLEAN`: This class is identical to SOURCE below 3 GeV. Above 3 GeV it has a 2-4 times lower background rate than SOURCE and is slightly more sensitive to hard spectrum sources at high galactic latitudes.
- `P8R2_ULTRACLEAN`: This class has a background rate between CLEAN and ULTRACLEANVETO.
- `P8R2_ULTRACLEANVETO`: This is the cleanest Pass8 event class. Between 100 MeV and 10 GeV the background rate is between 2 and 4 times lower than the background rate of SOURCE class.

2.3 Data Analysis

The final results of the data reconstruction is the FT1 file. This is a FITS file, which is a common format in astronomy: the Flexible Image Transport System. The data are presented in a table with all the informations: each event is associated with an energy, a direction and some additional pre-computed quantities, as well as a flag which allows the user to select among the predefined event classes. To perform the analysis it also needed also the information about the spacecraft, like the position along the orbit and the inclination, that are grouped as entry on the FT2 FITS file. LAT photon data are publicly available through the *Fermi* Science Support Center (FSSC)[1], together with the orbital history of the telescope.

The analysis of the data is done with the *Fermi gttools*[2], a set of tools based on the general package of the *ftools* [3] to have the maximum compatibility with the analysis of other astrophysics missions.

To use the photon file, the first operation to do is selecting data specifying the Region of Interest (ROI) of the sky, the time and the energy interval. Systematics effects are well known above 100 MeV and going below this energy requires additional care, therefore, to be safe, it needs to set the lower energy of our analysis at 100 MeV. Other cuts made at this point are needed to avoid the contamination from the Earth albedo, caused by the gamma-rays produced in the atmosphere from the interaction with cosmic rays. Therefore are selected only the photons coming with an angle with the local zenith of the spacecraft below 100° and limiting also the rocking angle to values $< 50°$.

The second step is to extract data only from the so called *Good Time Intervals* (GTIs), when the event is considered to be valid. To do this, it is used the FT2 information about the pointing and the live-time history of the spacecraft.

Analysis for a specific Region or Source The subsequent analysis needs to take into account the dependence of the photon direction to the IRFs. It is necessary to calculate the *live-time cube* which is the exposure time for a given position at a given angle of observation with the LAT normal.

Then there is the calculation of the *exposure map*, that is the integration of the IRF over the entire ROI:

$$\varepsilon(E'.\hat{p}') = \int_{ROI} dE d\hat{p} dt dR(E, \hat{p}|E', \hat{p}', t) \tag{2.3}$$

---

[1] http://fermi.gsfc.nasa.gov/ssc/

[2] http://fermi.gsfc.nasa.gov/ssc/data/analysis/scitools/overview.html

[3] http://fermi.gsfc.nasa.gov/docs/software/ftools/ftools_menu.html

Given the expression, the predicted number of photons from the source i is:

$$N_{pred} = \int dE' d\hat{p}' S_i(E', \hat{p}') \varepsilon(E', \hat{p}') \tag{2.4}$$

S_i that is the photon intensity of the source i.

At this point, a model of the ROI has to be produced, considering all known point-like sources in this region and the diffuse emission from the Galactic and isotropic components. The model is written in a XML file, that contains the best guess at the locations and spectral forms for the sources.

Finally, you can proceed by checking how likely this model fits the data using the *Maximum Likelihood Estimation* approach (described in Mattox et al., (1996) [40]).

2.3.1 LAT Analysis: The Maximum Likelihood and Data Analysis

During its lifetime the LAT is collecting hundreds of millions of photons (counts), but by the most analyses a small subset, of only a few hundred or a few thousand, has been useful for scientific purpose. The data has been too sparse in many cases to allow the use of χ^2 as test statistic. Therefore a Poisson likelihood optimization is needed to estimate the model parameters of the GeV sky.

The application of the likelihood method to photon-counting experiments is applied in the analysis of *Fermi*-LAT data, because it is never possible to really isolate a source in high-energy γ-rays. This is mainly due to the limited statistics, the dependence upon energy of angular resolution, as well as the strong and structured diffuse emission of the galactic and isotropic components, still poorly known, especially if compared to other wavelengths.

The technique requires to assume a model for the signal detected by the telescope; in this case, the input model is the distribution of γ-ray sources of the sky, and it includes their intensity and spectra. This statistic is used to estimate how many extent observed data are consistent with a statistical hypothesis and to find the best fit model parameters. These parameters are, e.g. the description of the source's spectrum, its position, and its intensity.

The likelihood $\mathcal{L}$ represents the probability to obtain the data given a model. Assuming that, the model has m free parameters $\alpha_{k=1 \ldots m}$ the expected observed distribution of the hits is given by:

$$M(E, \hat{p}, \{\alpha_k\}) = \int dt dE' d\hat{p}' R(E, \hat{p} \mid E', \hat{p}', t) S(E', \hat{p}', t, \{\alpha_k\}) \tag{2.5}$$

where S is the differential flux of the model $S = d\phi/dE' = dN/(dt dE' dA)$, A is the effective area, and therefore $M = dN/dt$.

The counts expected in a given energy range (E_1, E_2), the solid angle Ω and the time interval (t_1, t_2) are obtained as the integral of the differential count rate in the detector:

$$\Lambda(\{\alpha_k\}) = \int_{t_1}^{t_2} dt \int_{\Omega} d\hat{p} \int_{E_1}^{E_2} dE dM(E, \hat{p}, \{\alpha_k\}) \tag{2.6}$$

In the best case, which however requires powerful computing facilities, you can bin events in energy E, direction $\hat{p}$ and arrival time t, in such a way that each bin contains only one single photon (unbinned analysis). If the time binning width is Δt, in each bin the expected number of photons can be calculated by:

$$N_{exp}(E, \hat{p}, t, \{\alpha_k\}) = M(E, \hat{p}, t, \{\alpha_k\}) \cdot \Delta t \tag{2.7}$$

Indicating with P the set of bins containing one photon and Q the set of bins containing no photons. The probability of observing a photon could follow the Poisson distribution:

$$f(n, \nu) = \frac{\nu^n}{n!} e^{-\nu} \tag{2.8}$$

the likelihood function associated with the parameters set $\{\alpha_k\}$ is defined as

$$\begin{aligned} \mathcal{L}(\{\alpha_k\}) = \prod_P N_{exp}(\{\alpha_k\}) e^{-N_{\rm exp}(\{\alpha_k\})} \prod_Q e^{-N_{\rm exp}(\{\alpha_k\})} = \\ \prod_P N_{\rm exp}(\{\alpha_k\}) \prod_{P \cap Q} e^{-N_{\rm exp}(\{\alpha_k\})} \end{aligned} \tag{2.9}$$

The likelihood is defined as the product for each pixel of the probability densities of observing $N_{\rm obs}$ counts given the expectation $N_{\rm exp}$. Given that the probabilities are represented by extremely small numbers, it is convenient to compute the logarithm of the likelihood. In addition, the logarithm changes products to sums, easing the computation:

$$\begin{aligned} \ln \mathcal{L}(\{\alpha_k\}) &= \sum_P \ln N_{\rm exp}(\{\alpha_k\}) - \sum_{P \cap Q} N_{\rm exp}(\{\alpha_k\}) \\ &= \sum_P \ln M(\{\alpha_k\}) + \ln \Delta t^{N_{\rm obs}} - N_{\rm tot}(\{\alpha_k\}) \end{aligned} \tag{2.10}$$

where $N_{\rm obs}$ is the number of observed photons and $N_{tot}(\{\alpha_k\})$ is the total number of photons expected from the model $S(\{\alpha_k\})$. Since you want to find the set of parameters that maximizes the likelihood $\mathcal{L}$, or maximizes the $\ln \mathcal{L}$, you can omit the constant term $ln \Delta t^{N_{\rm tobs}}$, and so you can find:

$$\ln \mathcal{L}(\{\alpha_k\}) = \sum_P \ln M(\{\alpha_k\}) - N_{\rm tot}(\{\alpha_k\}) \tag{2.11}$$

The maximum of the likelihood $\mathcal{L}$ corresponds to the minimum of -ln $\mathcal{L}$. The most probable set of parameters $\{\alpha_k\}$ are obtained by minimizing -ln $\mathcal{L}$ and the likelihood function allows to determine the parameter covariances. In fact, the Cramér-Rao's lower bound allows to give an upper limit for the covariance matrix terms:

$$\sigma^2_{ab} = \{-\frac{\partial^2 \ln \mathcal{L}}{\partial\alpha_a \partial\alpha_b} \mid_{\{\bar{\alpha}_k\}}\}^{-1} \tag{2.12}$$

In the case of the limited statistics, an unbinned likelihood method can be used. Let us to suppose to use a grid, fine enough that in each pixel the number of observed counts is either 0 or 1. Let P be the pixel set where $N_i = 1$, the logarithm of the likelihood is therefore simply:

$$\ln \mathcal{L}(\{\alpha_k\}) = \sum_{i\in P} \ln \Lambda_i(\{\alpha_k\}) - \Lambda_{\text{tot}}(\{\alpha_k\}) \tag{2.13}$$

In a small enough pixel you have $\Lambda_i(\{\alpha_k\}) = M(E_i, \hat{p}_i; \{\alpha_k\})\Delta t \Delta\hat{p}\Delta E$ so Eq. 2.13 yields:

$$\begin{aligned}\ln \mathcal{L}(\{\alpha_k\}) &= \sum_{i\in P}[\ln M(E_i, \hat{p}_i; \{\alpha_k\}) + \ln \Delta t + \ln \Delta\hat{p} + \ln \Delta E] - \Lambda_{\text{tot}}(\{\alpha_k\}) \\ &= \sum_{i\in P}[\ln M(E_i, \hat{p}_i; \{\alpha_k\}) + \ln \Delta t^{N_{obs}} + \ln \Delta\hat{p}^{N_{obs}} + \ln \Delta E^{N_{obs}}] - \Lambda_{\text{tot}}(\{\alpha_k\})\end{aligned} \tag{2.14}$$

where N_{obs} is the total number of observed photons. Being the mid terms independent from the model, they can be neglected for the likelihood maximization and Eq. 2.14 becomes:

$$\ln \mathcal{L}(\{\alpha_k\}) = \sum_{i\in P}[\ln M(E_i, \hat{p}_i; \{\alpha_k\}) - \Lambda_{\text{tot}}(\{\alpha_k\}) \tag{2.15}$$

where the first summation can be practically computed looping over the energies and directions of the observed photons.

The likelihood method can also be used to compare two different models. In fact, the hypothesis $\mathcal{H}$ of having a model $\mathcal{M}$ with m free parameters, described by $\mathcal{L}$, and the hypothesis $\mathcal{H}_0$ of having a model $\mathcal{M}_0$ with $h < m$ free parameters, described by $\mathcal{L}_0$, can be compared using the *Test Statistic* (TS) defined as

$$TS = 2\ln(\frac{\mathcal{L}_{max}}{\mathcal{L}_{0,max}}) \tag{2.16}$$

In the limit of a great number of counts, if the models are *nested*[4], according with the Wilks' theorem, the TS is distributed as a χ^2 with $(m-h)$ degrees of freedom.

---

[4] With our notation, $\mathcal{M}_0$ can be obtained by fixing $(m - h)$ parameters of $\mathcal{M}$

In particular, the TS is the key to measure a significance of a source. If $\mathcal{L}$ is the likelihood of a model that includes the presence of a particular source and $\mathcal{L}_0$ is the likelihood of the model without this object, the TS is distributed as a χ^2 with n degrees of freedom, where n is the number of free parameters that characterises the source.

The unbinned analysis method permits a lot of simplifications and it is the preferred method for processing the LAT data of point sources when the number of events is expected to be small, i.e. when analysing data over short time periods. Unbinned likelihood should provide the ultimate statistical precision, because it does not loose any spatial or energy information. But as the number of counts increases, the time to calculate the unbinned likelihood becomes prohibitive, and the binned likelihood must be used. In addition, since the memory required for the likelihood calculation scales with the number of photons multiplied by the number of sources, memory usage can become prohibitive for long observations of complex regions, requiring the use of binned analysis, where the memory scales with the number of bins. The binned analysis is thus recommended to analyse extended sources such as the diffuse emission from molecular cloud in our galaxy, or sources in regions with bright background (such as the Galactic plane) for large time bins.

Chapter 3

AGNs: the principal aim of the study by *Fermi*-LAT

Active Galactic Nuclei (AGNs) are a peculiar class of galaxies that displays an extraordinary luminosity, up to 10^{49} erg s^{-1}, originated mainly by the central region. They are also our principal probe of the Universe on a cosmological scale, so understanding them is essential to study the formation and evolution of the Universe. There are several types of active galaxies: Seyferts, quasars, and blazars.

They can be recognized by the following characteristics:

- a luminosity and compact core that can outshine completely the host galaxy;
- a flux variability with time scale from minutes to months;
- the presence of a broad and narrow emission lines originated by non-stellar processes;
- a continuum of non-thermal emission that can range from radio frequencies to the TeV band;
- the existence of jets of matter that propagates from the inner region emitting non-thermal radiation

3.1 Unified Model

At present, the most accepted model is illustrated in Figure 3.1. At the center lies a Super Massive Black Hole (SMBH), with a mass in the range $10^6 \div 10^{10} M_{\odot}$, and whose gravitational potential energy is the ultimate source of the AGN luminosity. Matter pulled toward the black hole loses angular momentum through viscous or turbulent processes forming an accretion disk, which glows brightly at ultraviolet and soft X-ray wavelengths.

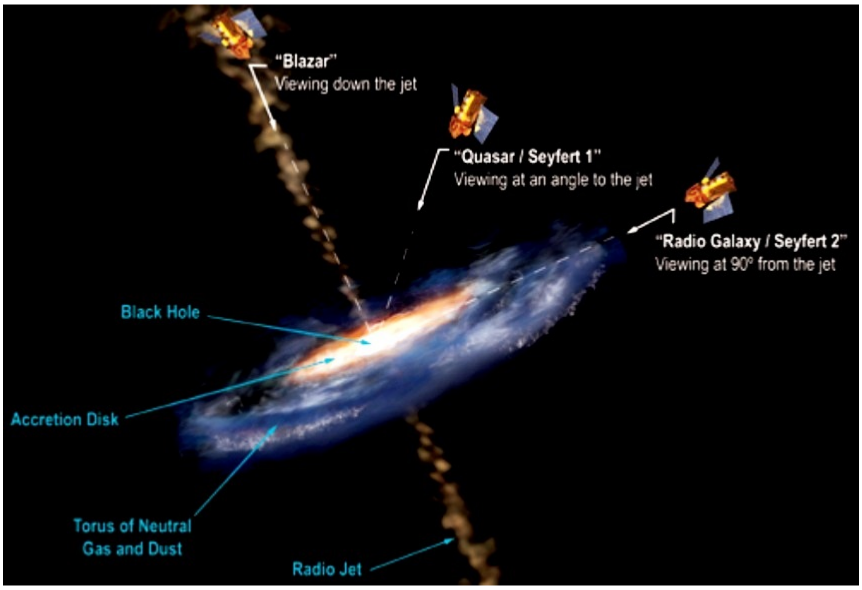

Figure 3.1: A schematic figure for radio-loud AGN (not to scale). Surrounding the central black hole, there is a luminous accretion disk. Broad emission lines are produced in clouds orbiting above the disk: this area is the Broad Line Region (BLR). A thick dusty torus (or warped disk) obscures the BLR from transverse line of sight; some continuum and broad-line emission can be scattered into those lines of sight by hot electrons that pervade the region. Narrow line are produced in clouds much farther from the central source, this area is the Narrow Line Region (NLR). Radio jets, shown here as the diffuse jets characteristic of low-luminosity, emanate from the region near the black hole, initially at relativistic speeds.

The SMBH have a Schwarzschild radius $r_S = \dfrac{2GM_\odot}{c^2}$, between 10^{-7} pc and 10^{-3} pc.

Strong optical and ultraviolet emission lines are produced in clouds of gas moving rapidly in the potential black hole, the so called "broad-line clouds". Optical and ultraviolet radiation may be obscured along the lines of sight by a torus or warped disk of gas and dust, located outside the accretion disk. Beyond the torus, slower moving clouds of gas produce emission lines with narrower widths. These are located in the Narrow Line Region (NLR), at about 100 pc from the SMBH.

In some objects, the outflows of energetic particles occur along the axis of the disk or torus, escaping and forming collimated radio-emitting jets. The plasma in the jets, at least on the smallest scales, streams outward at very high velocity, beaming the radiation relativistically in the forward direction. The jets can extend for more than 1 Mpc from the central black hole and emit radiation at all wavelengths.

This inherently anisotropic model of AGN implies radically different observational appearance depending on the viewing angle and historically led to different classes of sources, but all with the same underlying physical properties.

3.1.1 The Black-Hole Paradigm

The fundamental question about AGNs is, how such a huge amount of energy is generated in such a small region. Essentially the problem is that an AGN produces as much radiation as several trillion stars in a volume, that is significantly smaller than a cubic parsec. The current paradigm, or working model, for the AGN phenomenon is a “central engine” that consists of a hot accretion disk surrounding a Super Massive Black Hole. Energy is powered by gravitationally in-falling material which is heated to high temperatures in a dissipative accretion disk.

The fundamental process at work in an active nucleus is the conversion of mass to energy. This is done with efficiency η, so that energy available from a mass M is $E = \eta M c^2$. The rate at which energy is emitted by the nucleus ($L = dE/dt$) gives us the rate at which energy must be supplied to the nuclear source by accretion,

$$L = \eta \dot{M} c^2 \tag{3.1}$$

where $\dot{M} = dM/dt$ is the mass accretion rate onto the black hole. In general, for AGN, the efficiency is $\eta \sim 0.1$, it is an order of magnitude more efficient than the fusion of Hydrogen to Helium in stars, for which $\eta = 0.007$, and it is within a factor of ten of annihilation energy mc^2. In order to avoid disintegration, the outward force of radiation pressure must be counterbalanced by the inward force of gravity.

The outward energy flux at distance r from the center, is $F = L/4\pi r^2$, where L is the luminosity of the source. Noting that the momentum carried by a photon (of energy $E = h\nu$) is E/c, the outward radiation force on a single electron is thus obtained by multiplying the cross-section for the interaction with a photon:

$$F_{\text{rad}} = \sigma_e \frac{L}{4\pi r^2 c} \tag{3.2}$$

where σ_e is the Thomson scattering cross-section. The gravitational force acting on an electron-proton pair by a central mass M is of course $F_{\text{grav}} = -GM(m_p + m_e)/r^2 \approx -GMm_p/r^2$. The inward gravitational force acting on the gas must balance or exceed the outward radiation force to guarantee an efficient accretion, so it requires that $\mid F_{\text{rad}} \mid \leq \mid F_{\text{grav}} \mid$ so $\Rightarrow$ $L \leq \frac{4\pi G c m_p}{\sigma_e} M \approx 1.3 \cdot 10^{38} (M/M^{\odot})$ erg s^{-1}

This equation is known as the Eddington limit, and can be used to infer a minimum mass, the Eddington mass M_E, for a source of luminosity L. Equivalently, you can define the Eddington Luminosity

$$L_E = \frac{4\pi G c m_p}{\sigma_e} \tag{3.3}$$

which can be thought as the maximum luminosity of a source mass M, that is powered by spherical accretion.

3.2 Classification of Active Galactic Nuclei

The Unified Model differentiates the topologies of AGN classes by the different angle between the observer and the jet axis. If this angle is very small, the jet is almost pointing toward the observer, resulting a strong continuum and an extreme variability, and they are called *blazar*. Increasing the angle, at first you may see the BLR, but then the dust torus starts to obscure the central region, so that only the NLR can be observed.

Following the guidelines of the classification based on the radio/optical flux ratio, the conventional separation of AGN in *radio-quiet* and *radio-loud* objects depends on whether they have a radio (5GHz) - optical (B band) flux ratio ($R = F_{5\mathrm{GHz}}/F_B$) lower or higher than 10, respectively Kellermann 1989. In radio quiet objects the jet and jet-related emission can be neglected. On the contrary, in radio-loud objects the contribution from the jet (s) and the lobes dominates the luminosity of the AGN, at least in the radio, but possibly at other or even all wavelengths.

Based on the characteristics of their optical and ultraviolet spectra, AGN can be divided into the three main classes shown in table 3.1.

AGN taxonomy			
Radio Loudness	Type 2(Narrow Line)	Type 1(Broad Line)	Type 0(Unusual)
Radio Quiet	Seyfert 2	Seyfert 1, QSO	
Radio Loud	NLRG (FRI,FR II)	BLRG (SSRQ, FSRQ)	Blazars (BL Lac,FSRQ)

Decreasing angle to line of sight →

Table 3.1: AGN classification adapted from Urry and Padovani (1995)[48]. In the Unified Model the passage from one type to anoher is driven by the change of the angle between jet and the line of sight.

1. Those with bright continua and broad emission lines generated by hot, high velocities gas, are known as Type 1 AGN. In the radio-quiet group there are the Seyfert 1 galaxies which have relatively low luminosity, where the host galaxy can be resolved, and the higher-luminosity quasar (QSO), $L_{nuc} \sim 10^{43} \div 10^{45}$erg s^{-1}. The radio-loud Type 1 AGN are called Broad-Line Radio Galaxies (BLRG) at low luminosity and radio-loud quasars at higher luminosity, either Steep Spectrum Radio Quasars (SSRQ) or Flat Spectrum Radio Quasars (FSRQ) depending on the radio continuum shape.

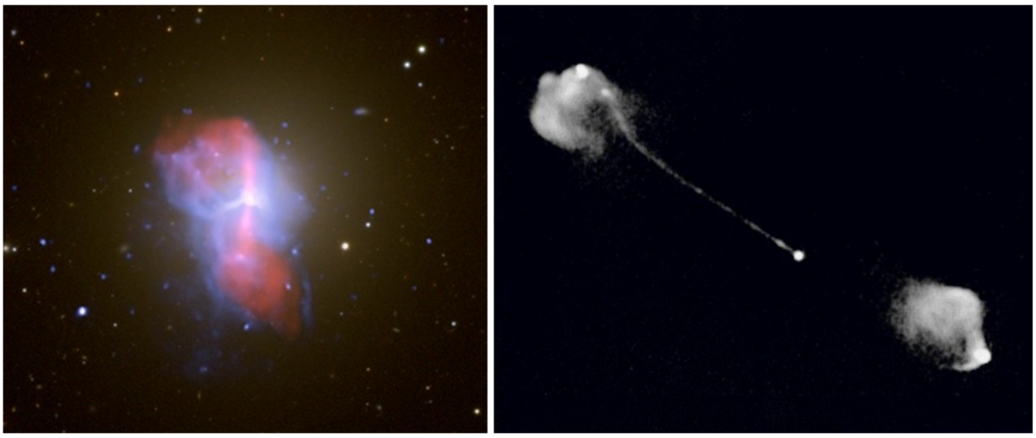

Figure 3.2: Comparison of the morphologies of a FRI radio galaxy (M84, left panel) and a FRII radio galaxy (3C 175, right panel). M84 is a massive elliptical galaxy in the Virgo cluster. The different appearance of the radio lobes is visible.

2. Type 2 AGN have a week continuum and only narrow emission lines, meaning either that they have no high-velocity gas, or the line of sight to such gas is obscured by a thick wall of absorbing material. Radio-quiet Type 2 AGN include Seyfert 2 galaxies at low luminosity, as well as the Narrow-Emission-Line X-ray Galaxies (NELG). The high-luminosity counterparts are the infrared-luminous IRAS AGN. Radio-loud Type 2 AGN, often called Narrow-Line Radio Galaxies (NLRG), include two distinct morphological types: the low-luminosity, $L_\nu \leq 10^{32}$erg s^{-1}, Fanaroff-Riley type I radio galaxies (Fanaroff and Riley 1974 [29]), which have often-symmetric radio jets whose intensity falls away from the nucleus, and the high-luminosity, $L_\nu \geq 10^{32}$erg s^{-1}, Fanaroff-Riley type II radio galaxies, which have more highly collimated jets leading to well-defined lobes with prominent hot spots.

3. A relatively small number of AGN have very unusual spectral characteristics, you can refer to these as Type 0 AGN and speculate that they are characterized by a small angle between the jet and the line of sight ("near 0 degrees"). These include the BL Lacertae (BL Lac) objects, which are radio-loud AGN that lack strong emission or absorption features. In addition, a small amount of radio-quiet AGN have unusually broad absorption features in their optical and ultraviolet spectra, and so their are known as BAL (Broad Absorption Line) quasars. BL Lac objects are characterized by very rapid variability, unusually high and variable polarization, high brightness temperatures and super-luminal velocities of compact radio cores.

The differences among the classes listed in Table 3.1 are caused mainly by orientation effects along the horizontal direction and by as-yet unknown physics in the vertical direction. Whether AGNs are classified Type 1 or Type 2, depends on obscuration of the luminous nucleus, and whether a radio-loud AGN is a blazar or a radio galaxy depends on the alignment of the relativistic jet with the line of sight. To summarize, the two causes of anisotropy are mainly the obscuration of infrared through ultra-violet light by the optically thick gas and dust torus and the presence of a relativistic jet.

3.2.1 Blazar Optical Classification

Blazar's classification depends on the details of their appearance in the optical band where they emit a mix of three types of radiation:

1. a non-thermal,jet-related, component;
2. thermal radiation coming from the accretion onto the super-massive black hole and from the broad-line region, hereinafter BLR (at least in most radio-selected sources); and
3. light from the host (giant elliptical) galaxy.

Blazars are divided into the following three subclasses (Padovani et al., 2001):

- Flat spectrum radio quasars (FSRQs), with the peak frequency of the synchrotron component detected in the IR-optical region and the high-energy γ-ray component dominating the luminosity;
- High-energy peaked BL Lac objects (HBLs, above all X-ray selected BL Lac objects), with the sync-peak frequency generally located in the UV/soft-X-ray region and the high and low energy components showing similar luminosity;
- Low-energy peaked BL Lac objects (LBLs, above all radio selected BL Lac objects) with luminosity and sync-peak frequency intermediate between the above sub classes[1].

---

[1] Giommi, Padovani et al. 2001 - A simplified view of blazars: clearing the fog around long-standing selection effects doi:10.1111/j.1365-2966.2011.20044.x [?]

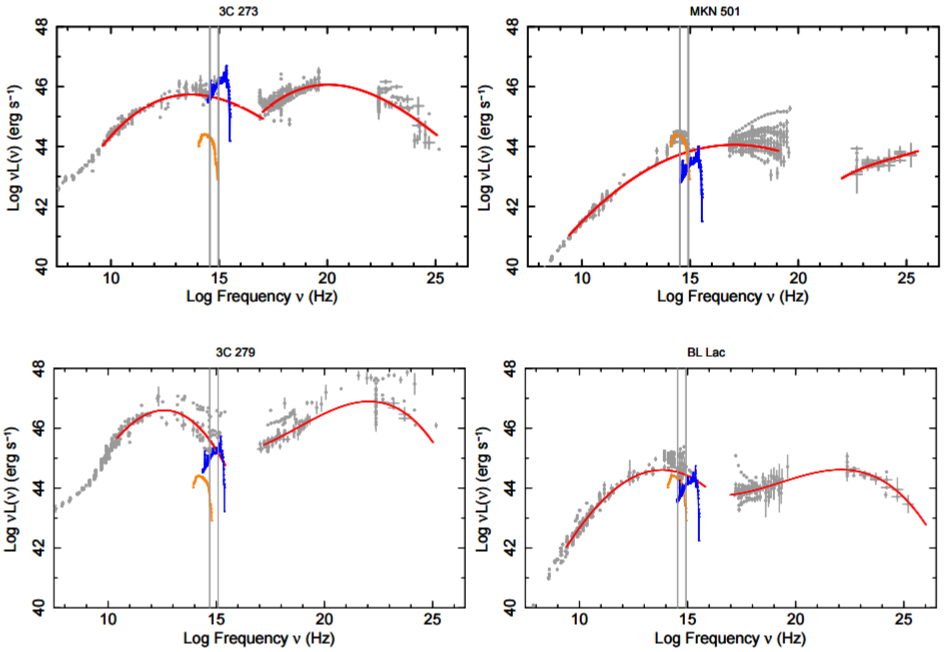

Figure 3.3: The SEDs of four representative blazars: two FSRQs, 3C 273 and 3C 279, and two BL Lac objects: Mrk 501 and BL Lac. The lines in colour denote the three main components of blazar SEDs, namely non-thermal radiation from the jet (red), emission from the disc and from the BLR represented by the composite QSO optical spectrum of Vanden Berk et al. (2001) (blue), and light from the host galaxy represented by the giant elliptical template of Mannucci et al. (2001) (orange). The two vertical lines indicate the optical observing window (3800–8000 Å).

Chapter 4

The *Fermi*-LAT's Catalogs

Since its launch in 2008, the *Fermi*-LAT has revolutionized our knowledge of the γ-ray sky. Its unique combination of high sensitivity, wide field of view, large energy range, and sky-survey operating mode, has enabled a complete mapping and continuous monitoring of the γ-ray sky to an unprecedented level. Several catalogs or sources lists, both general and specialized (AGNs, pulsars, supernova remnants, pulsar wind nebulae, gamma-ray bursts, very-high-energy candidates) have already been produced.

In this chapter I look at the two latest *Fermi*-LAT's catalogs, the 2FHL catalog and the third catalog of AGNs detected by the *Fermi*-LAT after four years of operation (3LAC), which follows the catalog 3FGL of all the sources.

4.1 2FHL: The second Catalog of hard *Fermi*-LAT sources

The second catalog of hard *Fermi*-LAT sources, named 2FHL, is a catalog of sources detected above 50 GeV by the Fermi-Large Area Telescope (LAT) in 80 months of data.

The Large Area Telescope, on board the *Fermi* satellite, has been efficiently surveying the GeV sky detecting over 3000 sources in just four years of exposure (see 4.2, the 3FGL catalog). These sources are detected in the $0.1 \div 300$ GeV band and, given that the LAT sensitivity peaks at $\sim$1 GeV, are representatives of the GeV sky. On the other hand, Cherenkov telescopes, with their good angular resolution and excellent point-source sensitivity but limited field of view, could explore only small patches of the $>$50 GeV sky. This catalog aims to close the gap between ground-based Cherenkov telescopes and all-sky observations at GeV energies from orbit.

Recently a new event reconstruction and characterization analysis (known as Pass8, [2.2.1]) has been developed by the *Fermi*-LAT collaboration. Pass8 significantly improves the background rejection, Point Spread Function (PSF), effective area of the LAT and help by understanding its systematic uncertainties. All these impressive improvements led to a significant increase of the LAT sensitivity. [1]

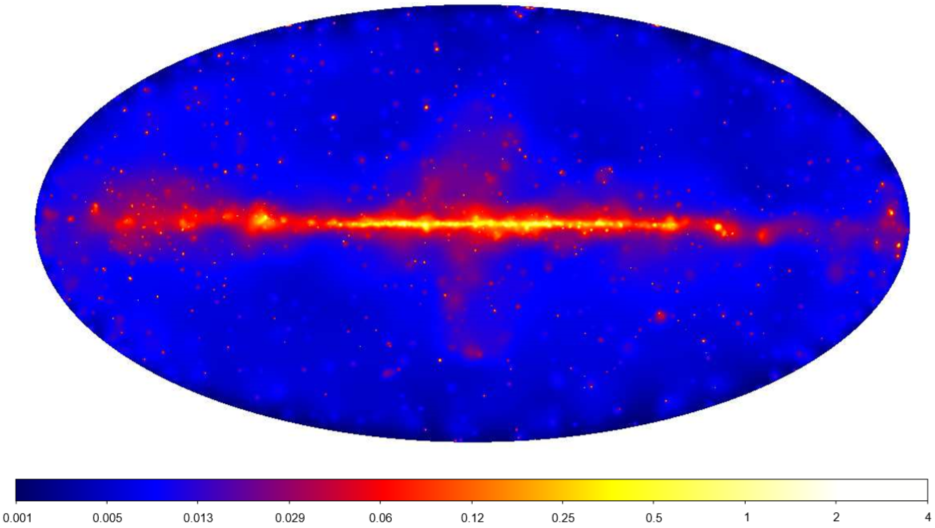

Figure 4.1: Adaptively smoothed count map in the 50 GeV - TeV band represented in Galactic coordinates. The color scale is logarithmic and the units are counts per (0.1 deg).

4.1.1 2FHL: Analysis

The catalog used 80 months (from August 2008 to April 2015) of Pass8-SOURCE photons with reconstructed energy in the 50 GeV - 2 TeV range. At these energies the LAT has an energy resolution of around 10-15% (1σ). Moreover, data were filtered removing time periods when the instrument was not in sky-survey mode. This leaves approximately 61,000 photons detected all over the sky.

The count map reported in Figure 4.1 shows that *Fermi*-LAT observes many point-like sources and large scale diffuse emissions in the direction of our Galaxy, some of which appears coincident with the so-called *Fermi* bubbles.

The analysis to detect sources is performed similarly to the other *Fermi*-LAT catalogs. The first step comprises the detection of source candidates (so called seeds) as fluctuations above the background. The sky is then divided into Region of Interests (ROIs), for which a sky model is built including all point sources in the ROI and also the Galactic and isotropic diffuse models. This model is fitted to the data using a standard maximum-likelihood

---

[1] Atwood et al. (2013) [17]

unbinned algorithm. The fit is typically repeated twice, using, at the beginning, a fast minimiser and then a slow but reliable minimiser (MINUIT). Between the two fits the source position is optimized using standard *Fermi* tools. Once a best fit has been found for a given ROI, the spectra of all sources are generated in three logarithmic energy bins from 50 GeV to 2 TeV.

Source Detection

The first step of the source detection stage comprises the identification of source seeds, which are the locations of potential sources whose significance is later to be tested through a maximum likelihood (ML) analysis. Seeds are identified via a sliding-cell algorithm as excesses above the background, as clusters of 3 or more photons, and via a wavelet analysis (Ciprini et al. 2007).

The analysis is performed in 154 regions of interest (ROIs), varying between 10° and 20° in radius, whose sizes and positions in the sky are optimized to cover all the seeds, ensuring that no more than 45 seeds are contained in a single ROI. For each ROI, it was build a sky model that includes all the potential sources in the region, as well as the Galactic and isotropic diffuse emissions.

The model is fit to the data via the unbinned ML algorithm provided within the *Fermi* Science Tools, and the spectrum of each source is modelled with a power law.

The fit is performed iteratively in order to ensure convergence, and to produce an optimal solution. It proceeds as follows:

1. Complex ML fits require approximate knowledge of the starting values of the parameters. For this reason, the first step aims to find those values by fitting each single source separately and to determine approximate spectral parameters. Throughout the entire process, the parameters of the diffuse emission models are left free to vary. The significance of each source is evaluated using the Test Statistic (TS). At each step in the procedure, marginal sources, those with TS <10 ($\approx 3\sigma$), are removed from the model.

2. In this second step, the positions of point-like sources, using the best-fit sky model derived at step 1, are optimized using the **gtfindsrc** tool. This step is done iteratively, as well by optimizing first the positions of the most significant sources.

3. The parameters and significances of the sources are estimated again (as in step 1) using the best-fit source positions. This step produces the best-fit sky model for any given ROI.

4. For each source is estimated the energy of the highest-energy photon (HEP), that the fit attributes robustly to the source model, selecting the HEP that has a probability $> 85\%$ to belong to the source.

5. A spectrum with three logarithmically spaced bins (boundaries of 50 GeV, 171 GeV, 585 GeV, 2 TeV) is generated for each source in the ROI that is detected with $TS \geq 25$ ($\approx 5\sigma$).

The procedure, described above, detected 360 point-like sources with $TS \geq 25$ and $N_{pred} \geq 3$ across the entire sky. The number of seeds kept in the ROI models with $10 \leq TS \leq 25$ is 453, while 7 are the seeds with $TS \geq 25$, but $N_{pred} < 3$.

Angular Resolution and the Comparison with pass7 Pass8 improves the PSF of the LAT at all energies. Above 50 GeV, the PSF has a 68% containment radius of ~0.1° and remains constant with energy. Such PSF, not dissimilar from the one of Cherenkov telescopes, allows *Fermi*-LAT to localize sources with an average precision of 4' at 95% confidence. Fig. 4.2 shows that *Fermi*-LAT can easily separate nearby sources like it is the case for NGC 1275 and IC 310. However, such resolution is most useful in the plane of the Galaxy, where it helps to solve crowded regions and resolve extended sources.

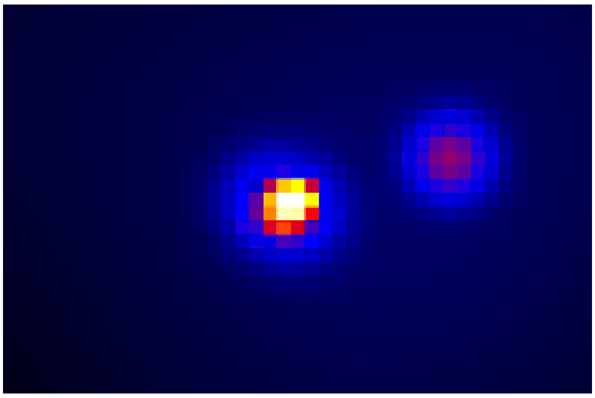

Figure 4.2: Adaptively smoothed count map of the region around NGC 1275 and IC 310 separated by roughly 0.6 degree.

In order to assess the improvement delivered by Pass8 at $\geq$50 GeV, the analysis procedure, described above, was applied also to 80 months of Pass7 reprocessed data. This analysis detected ~230 sources; ~ 35% fewer than the corresponding analysis of Pass8 data. The main difference is for the region $|b| > 10°$ where Pass8 data, because of the larger acceptance, and better PSF allow the detection of ~ 60% more sources than what could be achieved with Pass7. The improvements delivered by Pass8 above 50 GeV are clearly substantial.

Source Association

The approach for automated source association closely follows that used for the precedent *Fermi*-LAT catalogs: 2FGL, 1FHL, 3FGL and 3LAC catalogs[2]. They use catalogs of known or potential γ-ray source classes to determine the probability that a source from a given catalog or survey is associated with a 2FHL source.

The associations were derived with two different procedures: the Bayesian method and the likelihood-ratio method[3]. In the application of these two methods, potential counterparts were listed as associated if they were found to have a posteriori probability of at least 80%. For the Bayesian method, the catalogs relevant for associating 2FHL sources are the 5th version of the BZCAT (Massaro et al. 2015 [**?**]) and the ATNF Pulsar Catalog (Manchester et al. 2005 [38]).

For the likelihood-ratio association method, it was made use of a number of relatively uniform radio surveys. Almost all radio candidates of possible interest are in the NRAO VLA Sky Survey (NVSS)[4] or the Sydney University Molonglo Sky Survey (SUMSS)[5].

The 2FHL catalog was also cross-correlated with the TeVCat.

High-confidence associations allow to assess the systematic uncertainty in the accuracy of the LAT source positions. It was compared the angular separations' distribution of the γ-ray sources, with the highest confidence (probability $> 90\%$) counterparts (in units of 1σ errors), to a Rayleigh distribution, and found it slightly broader than expected.

4.1.2 2FHL: Results

The 2FHL catalog includes 360 sources detected over the whole sky, everyone with a likelihood test statistic of $TS \geq 25$ and number of associated photons, $N_{pred} \geq 3$.

The association procedure finds that the 75% of the sources in the catalog (274 sources) are extragalactic, the 11% (38 sources) are of Galactic nature, and the 13% (48 sources) are unassociated (or associated with a TeV source of unknown nature). The unassociated sources are divided between 23 sources located at $|b| < 10^\circ$, and 25 sources at $|b| \geq 10^\circ$. Therefore the fraction of extragalactic sources in the sample is likely larger than 80%.

---

[2] Nolan et al. 2012 [42]; Ackermann et al. 2013 [9]; Acero et al. 2015 [10]; Ackermann et al. 2015 [11]

[3] Described in detail in Ackermann et al. 2015 [11]; Acero et al. 2015 [6]

[4] Condon et al. 1998 [24]

[5] Mauch et al. 2003 [41]

Description	Associated Designator Number
Pulsar psr	1
Pulsar wind nebula pwn	14
Supernova remnant snr	16
Supernova remnant / Pulsar wind nebula spp	4
High-mass binary hmb	2
Binary bin	1
Star-forming region sfr	1
BL Lac type of blazar bll	180
BL Lac type with prominent galaxy emission bll-g	13
FSRQ type of blazar fsrq	10
Non-blazar active galaxy agn	2
Radio galaxy rdg	4
Radio galaxy / BL Lac rdg/bll	2
Blazar Candidate of Uncertain type I bcu I	7
Blazar Candidate of Uncertain type II bcu II	34
Blazar Candidate of Uncertain type III bcu III	19
Normal galaxy (or part) gal	1
Galaxy cluster galclu	1
Total associated	312
Unassociated	48
Total in 2FHL	360

Table 4.1: 2FHL Source Classes, http://arxiv.org/abs/1508.04449v1

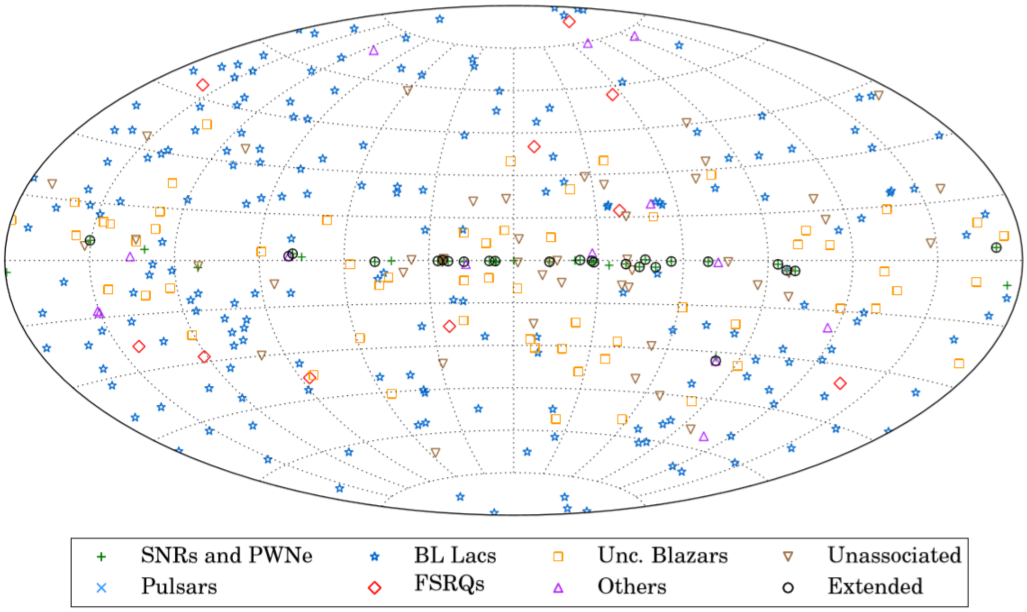

Figure 4.3: Sky map, in Galactic coordinates, showing the sources in the 2FHL catalog classified by their most likely association.

The number of 2FHL sources that have not been reported in 3FGL is 57, 47 of which have not been previously reported in any *Fermi*-LAT catalog nor in the TeVCat and are thus new γ-ray sources. The results of the association procedures are summarized in Table 4.1. Figure 4.4 shows the location of 2FHL sources color-coded according to their source class.

2FHL: Galactic Source Population

The narrow PSF core (about 0.1°) and moderate Galactic diffuse emission (in comparison with the > 100MeV band) allows the LAT to characterize and to study well the emission of sources in the plane of our Galaxy above 50 GeV. Within $|b| < 10°$, *Fermi*-LAT has detected 103 sources. Of those, 38 sources are associated with Galactic sources, 42 to blazars, 14 are unassociated and 9 are associated with other γ-ray sources whose origin is not known.

Figure 4.4 shows cut-outs of the Galactic plane with all detected sources labelled. Among the 38 Galactic sources, 16 are spatially coincident with SNRs, 13 are coincident with PWNe, 4 are associated with PWN/SNR complexes and the other 5 sources are X-ray binaries (3), one pulsar (PSR J0835-4510)and the Cygnus Cocoon.

It is clear that the majority of Galactic sources detected above 50 GeV are associated with objects at the final stage of stellar evolution.

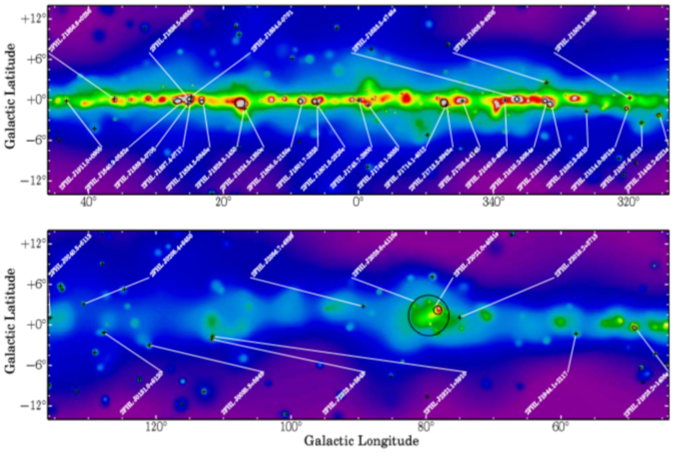

Figure 4.4: Adaptively smoothed count map showing the whole Galactic plane $0° \leq l \leq 360°$ at Galactic latitudes $-14° \leq b \leq 14°$ divided in four panels. Here are presented only the first two. Detected point sources are marked with a cross, whereas extended sources are indicated with their extensions.

Thus, Galactic surveys at above 50 GeV have the capability to detect new SNRs that might have been previously missed.

2FHL: The Extragalactic Sky

Most of the sources detected in 2FHL are extragalactic, 83% (299) are either located at $|b| \geq 10°$ or associated with an extragalactic source. BL Lacs represent the most numerous source class (54% of the full 2FHL catalog and 65% of the extragalactic sample), while there are a few detected FSRQs (10 sources, 3% of the full 2FHL catalog).

Such a low number of FSRQs is expected due to their soft spectra at >50 GeV. Most of the detected BL Lacs belong to the high-frequency synchrotron peak (HSP) class, rather than to the low-frequency synchrotron peak (LSP), or intermediate-frequency synchrotron peak (ISP) class.

There are 198 2FHL sources in the extragalactic sample that are detected both in the 3FGL and 1FHL catalogs. There are 33 other sources that are neither in the 3FGL nor in the 1FHL catalog .

One of the 33 exclusive 2FHL sources is 2FHL J1944.1-2117 that is associated with HESS J1943-213 [6]. This source is potentially an extreme high-frequency peaked BL Lac, classified as bcu II, located in the Galactic plane. The 2FHL J0537.4-6908, with a very hard spectral index is an extragalactic PWN in the LMC detected by H.E.S.S. up to 18 TeV [7].

The other 31 sources (out of the 33 2FHL exclusive sources) are not detected by Cherenkov telescopes yet. Of the 31 sources, 16 are classified as some type of blazar, whereas 14 are unclassified.

The number of FSRQs is strongly reduced from 1FHL (71 sources) to the 2FHL (10 sources). This is mainly due to the softer indices and spectral curvature that characterize the spectrum of this blazar population at these higher energies. Another indication of this effect is that only 2 sources at z > 1 (out of a total of 7) are FSRQs, while the rest are BL Lacs.

The 2FHL catalog will report, for every source, 3 energy-bin spectra in the energy range 50 GeV - 2 TeV. An example is reported, for Mkn 421, in Fig. 4.5. High synchrotron peaked (HSP) blazars, like Mkn 421, are detected by *Fermi*-LAT, typically, as power-law sources with a photon index of ~ 1.8. The data from the 3FGL, 1FHL and 2FHL catalogs allow to characterize the emission at the peak of such sources rather well.

---

[6] Abramowski et al. 2011

[7] Abramowski et al. 2012, 2015

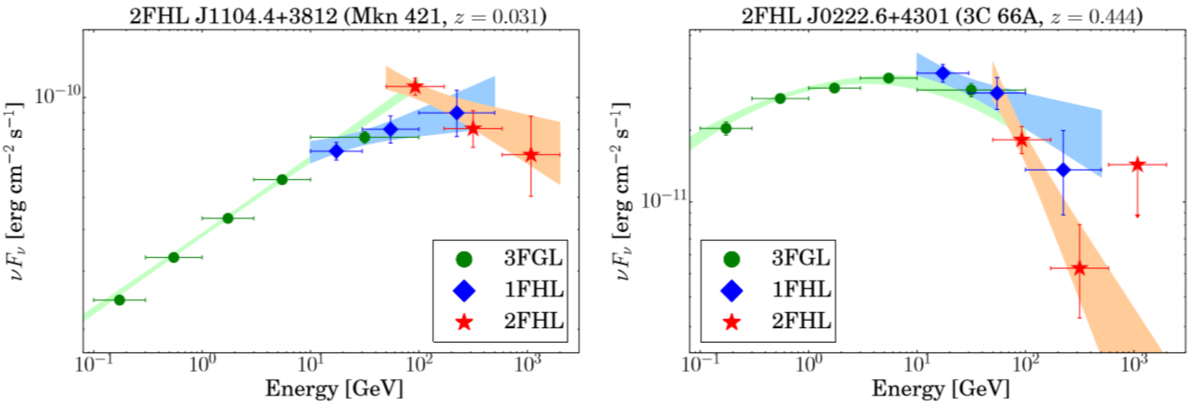

Figure 4.5: The spectral energy distributions of Mrk 421 (left panel) and 3C 66A (right panel) over four decades in energy. The higher energy peak is well characterized by combining data from the 3FGL (green diamonds), 1FHL (blue circles), and 2FHL (red stars).

Gamma-ray attenuation The comparison of the 2FHL and 1FHL redshift distributions presents that, on average, 2FHL sources lie at lower redshifts than the 1FHL ones. This might be because FSRQs and LSP blazars, which tend to be located at higher redshifts, have soft spectra and are faint in the 2FHL band.

The improved reconstruction and increased acceptance allow *Fermi*-LAT to detect photons up to ∼2 TeV. Both these aspects enable studies of the Extragalactic Background Light (EBL) which can absorb high-energy photons emitted from sources at cosmological distances.

BL Lacs with substantial high-energy emission, at e.g. >100 GeV are excellent probes of the EBL and have already been used with success to constrain the γ-ray opacity of the Universe.

High redshift sources appear even fainter because of the extragalactic background light (EBL) attenuation. The EBL contains all the photons, from the ultraviolet to the infrared, that have been emitted by star formation processes and super-massive black hole accretion throughout the history of the Universe [8].

The spectrum of extragalactic γ-ray sources, in the whole energy range of our analysis, is modified by pair-production interaction of the γ-ray photons with the EBL. This interaction produces an attenuation of the observed fluxes that is energy and redshift dependent (the larger the γ-ray energy and/or the redshift, the larger the attenuation).

The effect of the EBL attenuation is clearly seen in Figure 4.6. This

---

[8] e.g. Dwek and Krennrich 2013 [27]

figure shows the significant dependence of the spectral index on the redshift at the 2FHL energies whereas that dependence is reduced at lower energies where the EBL interaction is less relevant.

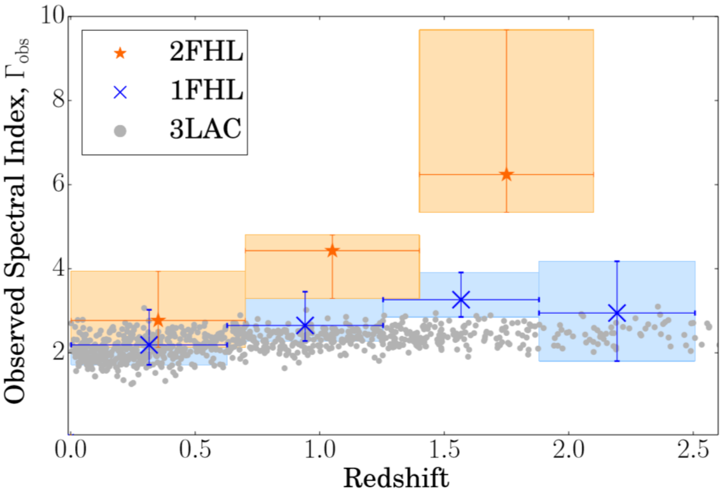

Figure 4.6: Observed spectral index versus redshift of the 3LAC sources (energy range, 0.1 GeV - 100 GeV), the median spectral index of the 1FHL sources (10 GeV - 500 GeV) in 4 redshift bins, and the median spectral index of the 2FHL sources (50 GeV - 2 TeV) in 3 redshift bins. The uncertainties are calculated as the 68% containment around the median. There is a dependence of the spectral index on redshift at the energies where the EBL attenuation is significant.

The EBL attenuation can be parametrised by an optical depth τ that can be derived from empirical EBL models. In fact, the EBL sets a distance limit from where γ-ray photons of a given energy are expected to reach, the cosmic γ-ray horizon.

4.2 The 3LAC Catalog

The third catalog of AGNs, detected by the *Fermi*-LAT after four years of operation (3LAC), is a follow-up of the precedent catalog 2LAC (Ackermann et al. 2011 [7]) and makes use of the results of the 3FGL catalog (the third Fermi Large Area Telescope source catalog of sources in the 100 MeV - 300 GeV range) [9]. In addition to dealing with more data, the 3FGL benefits from improved data selection, instrument response functions and analysis techniques, like an updated model for Galactic diffuse γ-ray emission and an improved methods for associating LAT sources with potential counterparts at other wavelengths.

The 3FGL catalog includes 3033 sources with $TS > 25$, 2192 sources of which are detected out of the galactic plane, at $|b| > 10°$ where b is the Galactic latitude. Among these 2192, 1591 (71%) are associated with high confidence with AGNs, which constitute the 3LAC. The 3LAC catalog represents a sizeable improvement over the 2LAC as it includes 70% more sources (1591 vs. 929).

4.2.1 Observation with LAT: Analysis Procedures and Source Classification

The data were collected over the first 48 months of the mission, from 2008 August 4 to 2012 July 31 (MJD 54682 to 56139). Time intervals during which the rocking angle of the LAT was greater than 52° were excluded and a cut on the zenith angle of gamma rays of 100° was applied to limit the contribution of Earth-limb gamma rays. The reprocessed `Pass7REP_V15` Source event class was used with photon energies between 100 MeV and 300 GeV.

An all-sky likelihood analysis produced an "optimized" model, where parameters characterizing the diffuse components, in addition to sources, were fitted. The analysis of the residual TS map provided new seeds, that were included in the model for a new all-sky likelihood analysis. This iterative procedure yielded over 4000 seeds, that were then passed on to the maximum likelihood analysis for source characterization.

The analysis was performed with the binned likelihood method below 3 GeV and the unbinned method above 3 GeV. These methods are implemented in the *pyLikelihood* library of the *Science Tools* [10] (v9r23p0).

Different spectral fits were carried out with a single power-law function ($dN/dE = N_0(E/E_0)^{-\Gamma}$) and a log-parabola function ($dN/dE = N_0(E/E_0)^{-\alpha-\beta} log(E/E_0)$), Massaro et al. 2004, where N_0 is a normalization factor, Γ, α and β are spectral parameters and E_0 is an arbitrary reference energy adjusted on

---

[9] Ackerman et al. (astro-ph.HE) 30 April 2015 , http://arxiv.org/abs/1501.02003v2

[10] http://fermi.gsfc.nasa.gov/ssc/data/analysis/documentation/Cicerone/

a source-by-source basis, to minimize the correlation between N_0 and the other fitted parameters over the whole energy range (0.1 to 300 GeV).

A threshold of $TS = 25$, as calculated with the power-law model, was applied to all sources, corresponding to a significance of approximately 4σ. At the end of this procedure, 3033 sources survived the TS cut and constitute the 3FGL catalog.
A map of the LAT flux limit, calculated for the four-year period covered by this catalog, a $TS = 25$ and a photon index of 2.2, is shown in Galactic coordinates in Figure 4.7.

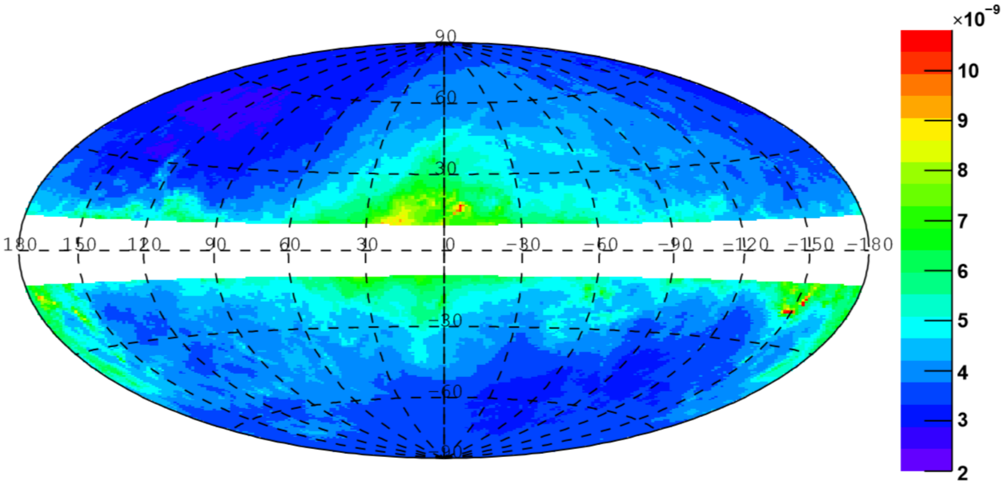

Figure 4.7: Point-source flux limit in units of photons $\mathrm{cm}^{-2}\mathrm{s}^{-1}$ for $E > 100$ MeV and photon spectral index $\Gamma = 2.2$ as a function of sky location (in Galactic coordinates) for the 3LAC time interval. http://arxiv.org/abs/1501.06054 (3LAC - Ackermann et al. 2015 [10])

The 3LAC catalog looked for candidate counterparts to 3FGL gamma-ray sources, which show typical blazar/radio-loud AGN characteristics, such as radio loudness, a flat (for blazars) or steep (for misaligned AGNs) radio spectrum between 1.4 GHz and 5 GHz, broadband emission and polarization. In the context of AGNs, an identification is only firmly established when correlated variability with a counterpart detected at other energies has been reported.

So far, only 26 AGNs have met this condition (see 3FGL). For the rest, it was used statistical approaches to find associations between LAT sources and AGNs. It was applied the Bayesian Association Method to catalogs of sources that were already classified and/or characterized. This method uses Bayes' theorem to calculate the posterior probability that a catalog source is the true counterpart of a LAT source.

AGN Optical classification

To optically classify a source you can use different resources, in decreasing order of precedence: optical spectra from the intensive follow-up programs (Shaw et al. 2013 [46]), the BZCAT list (i.e., FSRQs and BL Lacs in this list, Massaro et al. 2009 [39]), spectra available in the literature (SDSS, 6dF, etc.) when more recent than BZCAT version 4.1.1 (August 2012).

The resulting classes are as follows:

- confirmed classifications: FSRQ, BL Lac, radio galaxy, steep-spectrum radio quasar (SSRQ), Seyfert and NLSy1 these are sources with a well-established classification in the literature and/or through a well evaluated optical spectrum (with clear evidence for or lack of emission lines).
- tentative classifications: BCU-blazar candidates of uncertain type: these are considered candidate blazars because the association methods select a candidate counterpart that satisfies at least one of the following conditions:
    a) a BZU object in the BZCAT list;
    b) a source with multi-wavelength data in one or more of the WISE, AT20G, VCS, CRATES, PMN-CA, CRATES-Gaps, or CLASS lists, that indicates a flat radio spectrum, and shows a typical two-humped, blazar-like spectral energy distribution (SED);
    c) a source included in radio and X-ray catalogs not listed above and for which it was found a typical two-humped, blazar-like SED.

  The BCU sources are divided into three sub-types:

    – BCU I: the counterpart has a published optical spectrum but not sensitive enough for a classification as an FSRQ or a BL Lac;
    – BCU II: the counterpart is lacking an optical spectrum but a reliable evaluation of the SED synchrotron-peak position is possible;
    – BCU III: the counterpart is lacking both an optical spectrum and an estimated synchrotron-peak position but shows a blazar-like broadband emission and a flat radio spectrum;
    – AGN: these candidate counterparts are considered radio-loud generic AGNs (active galaxies with broadband emission) which do not fit into the above classifications (i.e., confirmed blazars, known misaligned AGNs, or BCUs) due to a lack of detailed information. An object in this category does not have a typical blazar SED or other blazar characteristics. Its SED resembles that of a radio-loud AGN but the (current) poor literature information suggested

that they are more likely dealing with a misaligned AGN (radio galaxy, SSRQ etc) than with a blazar. These radio-loud AGNs can not be put into another category.

AGN Type	Entire 3LAC	3LAC Clean Sample	Low-Latitude Sample
FSRQ	467	414	24
BL Lac	632	604	30
Blazar of Unknown type	460	402	125
...BCU I	57	49	11
...BCU II	346	308	85
...BCU III	57	45	29
Other AGN	32	24	3
...AGN	6	2	0
...CSS	2	1	0
...NLSy1	5	5	0
...RG	14	13	2
...SSRQ	5	3	0
All	**1591**	**1444**	**182**

Table 4.2: 3LAC Catalog

SED classification

To better characterize the candidate counterparts of the 3FGL sources, that are considered candidate blazars or more generally radio-loud AGNs, it was studied their broadband spectral energy distributions by collecting all data available in literature. It was used the estimated value of the (rest-frame) broadband-SED synchrotron peak frequency ν^s_{peak} to classify the source as either a low-synchrotron-peaked blazar (LSP, for sources with $\nu^s_{peak} < 10^{14}$ Hz), an intermediate-synchrotron-peaked blazar (ISP, for 10^{14} Hz $< \nu^s_{peak} < 10^{15}$ Hz), or a high-synchrotron-peaked blazar (HSP, if $\nu^s_{peak} > 10^{15}$ Hz).

The ν^s_{peak} distributions for FSRQs and BL Lacs are displayed in Figure 4.8. The FSRQ distribution is sharply peaked around $log\nu^s_{peak} = 13$ while BL Lacs span the whole parameter space from low (LSP) to the highest frequencies (HSP). The BCU distribution resembles that of BL Lacs with an additional fairly weak component akin to FSRQs at this low ν^s_{peak} end.

4.3 BL Lacs Anisotropy

In this part I observe and try to explain the apparent anisotropy of the BL Lac objects, between the northern and southern hemisphere. This anisotropy is in contrast with the cosmological principle. It predicts that the

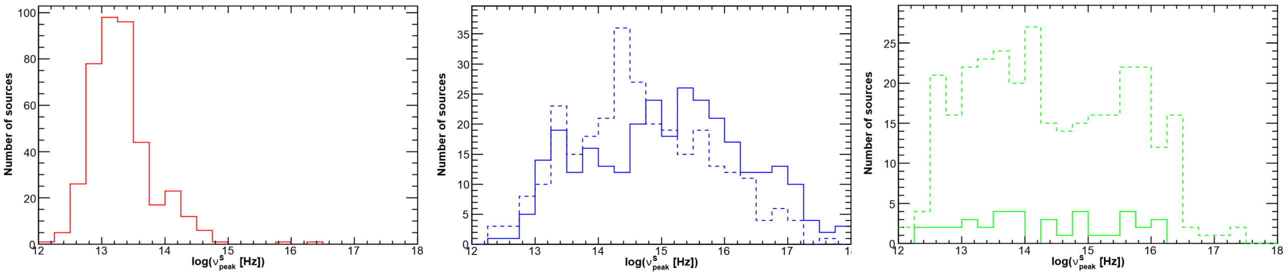

Figure 4.8: Distributions of the synchrotron peak frequency ν^{s}_{peak} for FSRQs (left), BL Lacs (middle) and BCUs (right) in the Clean Sample. The solid and dashed histograms correspond to sources with and without measured red-shifts, respectively. http://arxiv.org/abs/1501.06054 (3LAC - Ackermann et al. 2015 [**?**])

distribution of matter in the Universe is homogeneous and isotropic when it is viewed on a enough large scale, as in fact are the observed AGNs.

In the 3LAC catalog, the deficit in the classification of the AGNs in the region of the celestial south pole, already reported in 2LAC, is clearly visible, while a relative excess is seen in the region of celestial north pole. This anisotropy is mainly driven by BL Lacs, with 51% more sources in the northern Galactic hemisphere (362) than in the southern one (242).

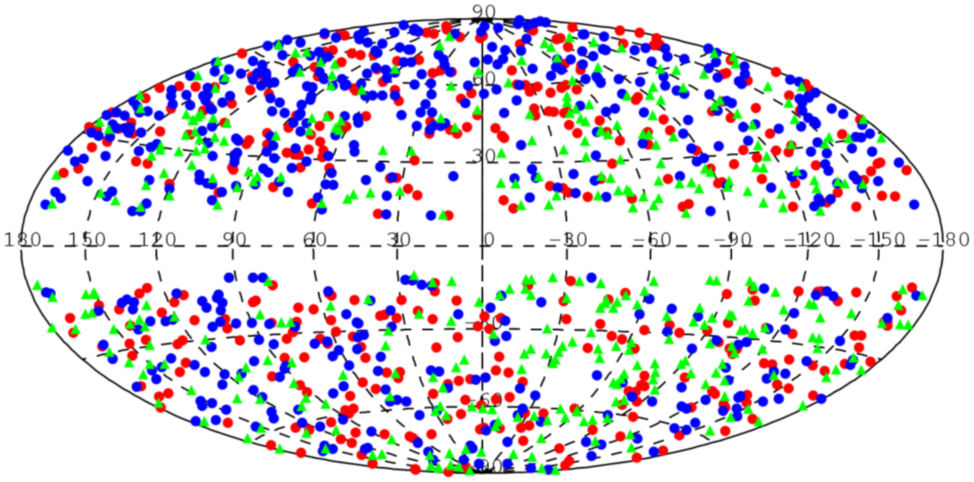

Figure 4.9: Locations of the sources in the Clean Sample in Galactic coordinates. Red: FSRQs, blue: BL Lacs, magenta: radio galaxies, green: AGNs of unknown type. http://arxiv.org/abs/1501.06054 (3LAC - Ackermann et al. 2015 [10])

The Figure 4.9 presents a visible anisotropy for the division in the two hemisphere of the BL Lac galaxies (blue points).

4.4 Analysis AGN Distribution

In the analysis on the distribution of AGNs, I restrict the ensemble to the Clean Sample AGNs, so as to operate with well-defined sources. For studying this non-uniform subdivision, I divided the sources in eighteen classes depending on the declination angle. In this case the declination $0 \div 90$ is referred to the northern hemisphere, instead the declination angle $0 \div -90$ is referred to the southern one. These classes have an opening angle of 10° with a surface area, different from every class, that depends on the declination, it is maximum at the equator and decreases closer to the poles:

$$sup_{sphere-ring} = \int_0^{2\pi} d\varphi \int_{\theta_1}^{\theta_2} r^2 sen\theta d\theta = 2\pi R^2 (cos\theta \,|_{\theta_1}^{\theta_2} \tag{4.1}$$

where so the total area of the spherical surface is $Sup_{tot} = 4\pi R^2$.

The cosmological principle is expected to produce an uniform distribution of sources in each direction. This leads, for the different area of the rings of spherical surface, to a number of AGN in the ring between the angles $\theta_1 \div \theta_2$, in case of an uniform distribution equal to:

$$n_{\theta_1 \div \theta_2} = N \frac{2\pi(cos\theta_1 - cos\theta_2)}{4\pi} \tag{4.2}$$

with θ between $0 \div \pi$ and N is the number of the total objects,

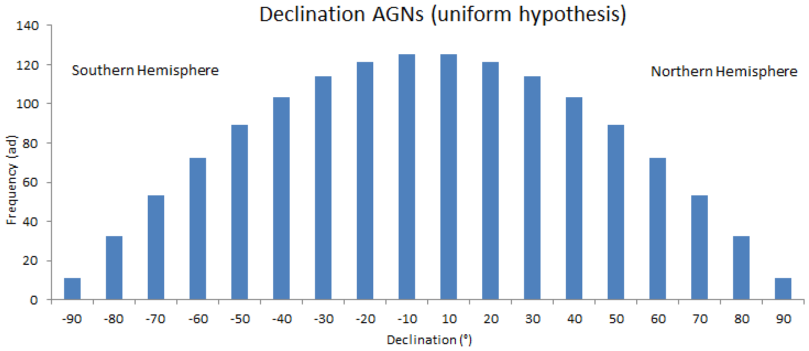

Figure 4.10: Distributions of the AGN frequency respect the ring of the sphere's area, in case of homogeneous distribution provided by the cosmological principle.

In Figure 4.10 there is the uniform distribution expected from the cosmological principle. I compared the expected distribution with the observed AGNs from the catalog 3LAC *Fermi*, to test the null hypothesis, in which the cosmological principle is followed. Since the expectation value of each class follows a Gaussian distribution, you can use the statistical method of calculation of the chi-square test, for studying the compatibility between the expected distribution and the observed one, made by taking all the Clean Sample AGNs from 3LAC *Fermi* catalog.

$$\chi^2 = \sum_{i=1}^{M} \frac{(O_i - A_i)^2}{A_i} \tag{4.3}$$

where $M = 18$ is the classes' number, A_i are the expected values of the classes provided for the cosmological principle and O_i are the experimental values from the 3LAC catalog. The free degree's number, for comparing the χ^2 calculated with the tabulate value, is $n = M - 1$.

AGN homogeneity

Considering the full set of AGN observed a fairly symmetrical distribution with an average angle of $\bar{\alpha} = (3.85 \pm 0.90)^\circ$ not compatible with zero, but not too far from it .

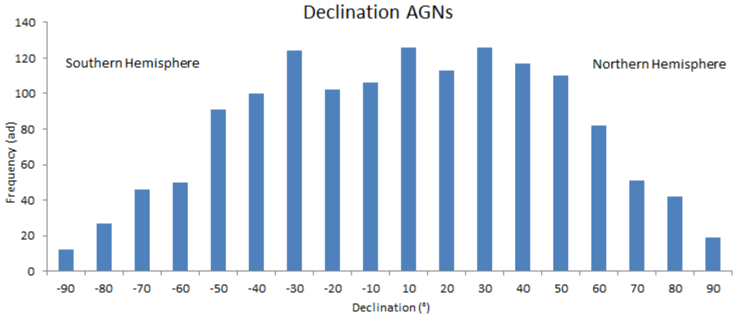

Figure 4.11: AGNs' distribution along the declination angle.

Figure 4.11 is the graph, derived from the catalog 3LAC, of the AGN distribution. It has a good symmetry between the two hemispheres and a distribution similar to the uniform one. The central region, defined by an angle included between $-20^\circ < \theta < 20^\circ$, is affected by the diffused light of our galaxy, which overlaps the extra-galactic sources, leading to a decrease in the number of observed AGNs in the band around the equator.

Table 4.3 shows a comparison of the value of the chi-square, obtained from the compatibility between the experimentally observed distribution of AGN and the theoretical expected cosmological principle, and one taken from the statistic tables.

Experimental χ^2	Degree of freedom	Tab. χ^2 at 99.9%	Tab. χ^2 at 99.5%
34.71	18	40.79	35.72

Table 4.3: Comparing the distribution of AGNs with uniform distribution. The experimental distribution is compatible with the uniform one within 3σ

Data are observed to be compatible, within 3 σ, with the uniform distribution.

In addition, as shown in Figure 4.12, the other major class of AGN, the Flat Spectrum Radio Quasars (FSRQ), has a distribution that is skewed towards the northern hemisphere while maintaining compatibility with the homogeneous and uniform distribution expected from the cosmological principle.

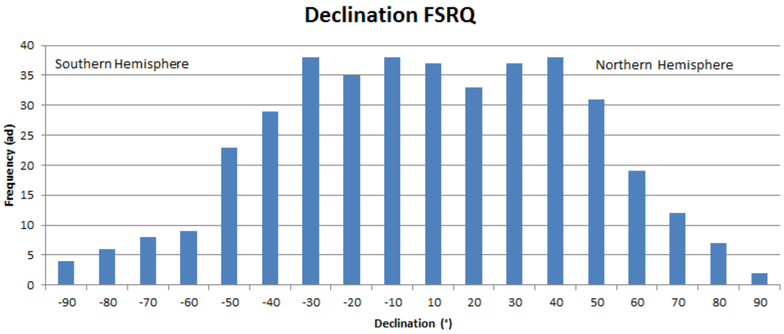

Figure 4.12: FSRQs' distribution along the declination angle. Average angle $(2.20 \pm 0.6)^\circ$.

BL LACs apparent dis-homogeneity

In the graphs in Figure 4.13, You can observe that the BL LACs declination's distribution is asymmetrical with respect to the equator. You can compute the average angle $\bar{\alpha} = (13 : 36 \pm 0.6)^\circ$, which appears to be incompatible with zero and skewed towards the northern hemisphere. You can compare in Figure 4.13 the difference between the observed distribution of BL Lacs taken by all Clean Sample catalog 3LAC and distribution of the same number of sources in the case of uniformity.

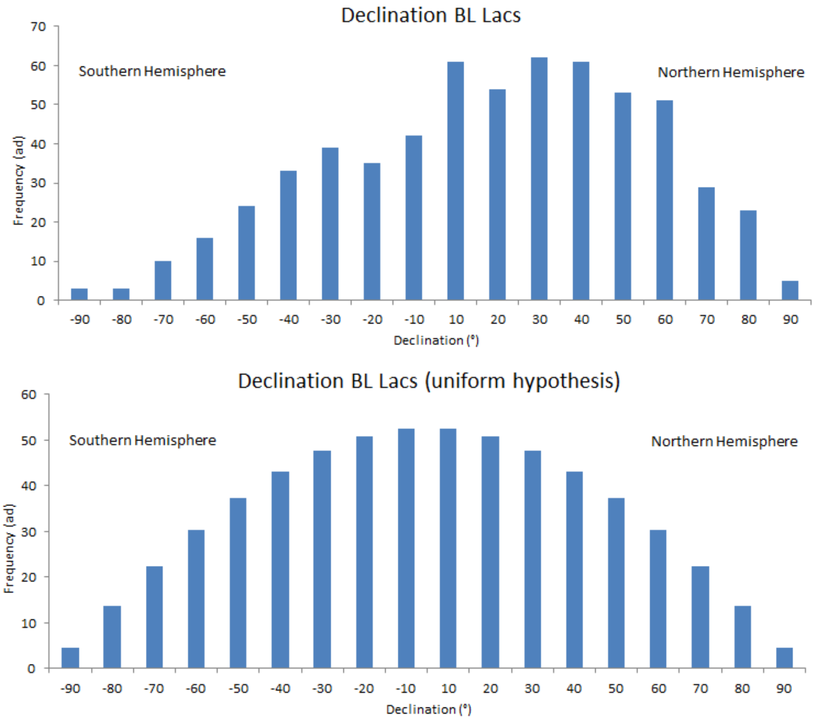

Figure 4.13: Top: BL LACs' distribution along the declination angle. Bottom:BL LACs' distribution, along the declination angle, under the assumption of the cosmological principle.

Experimental χ^2	Degree of freedom	Tab. χ^2 at 99.9%	Tab. χ^2 at 99.99%
80.78	18	40.79	47.56

Table 4.4: Comparing the distribution of AGNs with uniform distribution. The experimental distribution is not compatible with the uniform one.

The χ-square value turns out to be incompatible with the hypothesis of uniformity far beyond the value of 5 σ. This result, as opposed to discrete uniformity views for the Active Galactic Nuclei, brings out the question of what could be the reason for this unexpected observed anisotropy.

Explanation of BL LACs apparent dis-homogeneity

The compatibility of the distribution of the AGNs with the uniform hypothesis led us to think that the asymmetry of BL Lacs was due, not to a lack of homogeneity of the AGNs in the universe, but to a problem in the production of the catalog. I believe that this anisotropy is only apparent and due to the fact that there are fewer counterparts in the Southern hemisphere. As a matter of fact, there are not currently enough optical telescopes to completely map the southern hemisphere.

As a support to my hypothesis the BCU distribution is skewed towards the southern hemisphere (Figure 4.14).

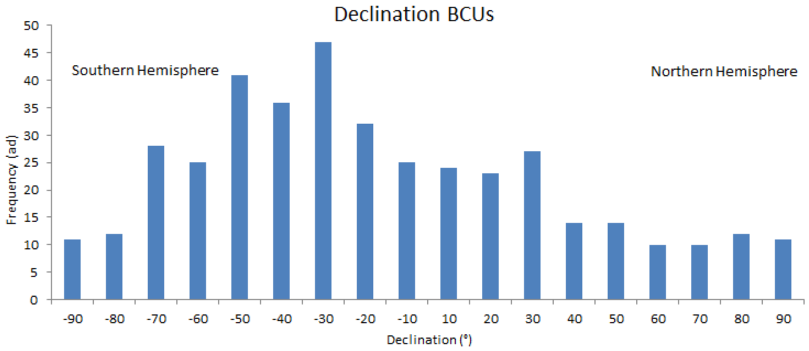

Figure 4.14: BCU distribution along the declination angle.

If you could classify all the BCU galaxies as BL Lacs, you would get a distribution, which would be compatible within 3.5 σ with that one provided by the cosmological principle (as can be seen in Figure 4.15 and values in Table 4.5).

Experimental χ^2	Degree of freedom	Tab. χ^2 at 99.9%	Tab. χ^2 at 99.5%
39.52	18	40.79	35.72

Table 4.5: Comparing the distribution of BL LAc + BCU with uniform distribution. The experimental distribution is compatible within 3.5σ

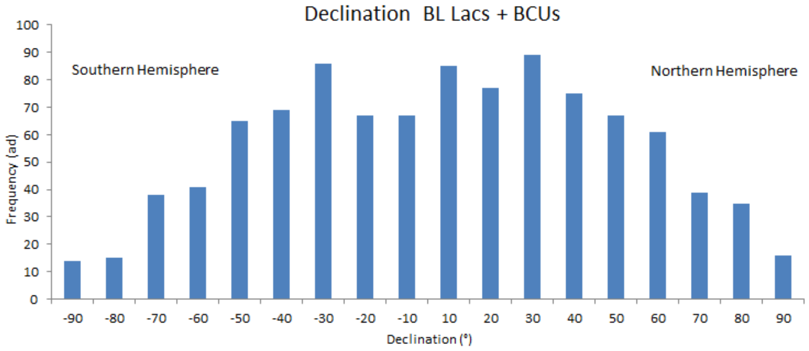

Figure 4.15: BL LACs + BCUs distribution along the declination angle.

You can therefore think of ascribing this apparent anisotropy to an incomplete cataloging of the sources, due to a lack of optical/radio telescopes in the southern hemisphere. When more data from the southern hemisphere would be available, you could expect that many BCU will be classified as BL Lacs and will fill the anisotropy between the two hemispheres, following the requests of the cosmological principle (see Figure 4.15).

To fill this observational gap in the southern celestial hemisphere, the ESO (European Southern Observatory) has designed and will begin to construct a new telescope, the E-ELT, at the Paranal Observatory in Chile. The E-ELT will be the largest optical/near-infrared telescope in the world and it will gather 15 times more light than the largest optical telescopes operating today. The main mirror will consist of almost 800 hexagonal segments, each 1.4 metres across. Standing at 39-metre of diametre, it will be the world's biggest eye on the sky.

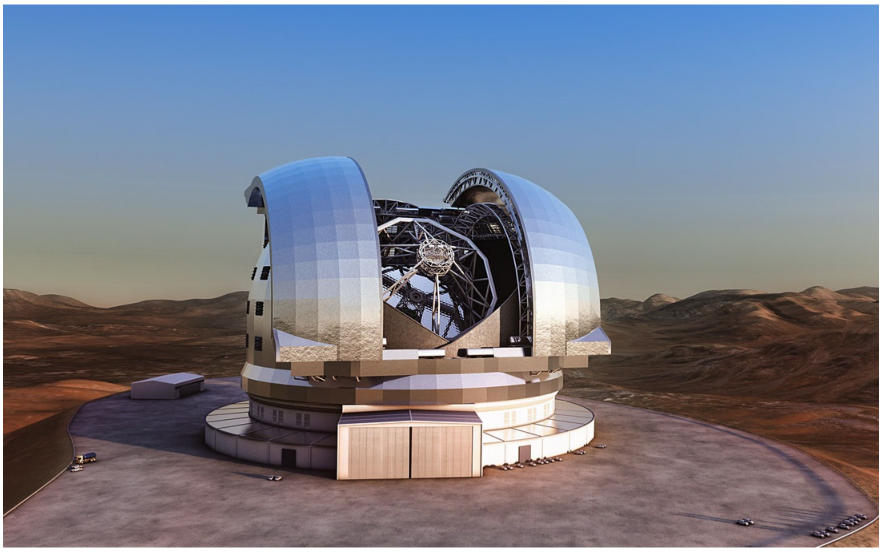

Figure 4.16: The European - Extremely Large Telescope (E-ELT).

Chapter 5

Space and time clustering

The objective of the data analysis, presented in this chapter, is to cluster photons detected by the LAT. The analysis was made using constraints on space and time, in order to detect new potential sources hidden in the cosmic gamma-ray noise. The analysis studies also some local flux variations, that are caused by the flare phenomena in the active galactic nuclei.

The aims of my analysis work are:

- to seek new high energy sources;
- to observe the temporal variations of the luminous flux of high-energy sources;
- to research flare phenomena.

The analysis of this thesis concentrates on data taken by *Fermi*-LAT from September 2008 to March 2015 with the PASS8.

The events taken in consideration were those ones gathered by *Fermi*-LAT with energies between 50 GeV and 2 TeV.

The choice of select the photons with very high energy allows, as you can see in the LAT PASS8 paragraph, to have an excellent angular resolution, of about 0.15 degrees.

5.1 Clustering Algorithm

In the 2FHL catalog were researched and analysed both point sources and extended ones. In my analysis, however, I confined the study only at point sources.

I used the python library to build the analysis code. The clusters are computed as it follows:

- for each events I take the follow ones that stay inside the time period t;

- for each point p in a set of events, the distances between the other points are calculated;
- for each point if there is a number of photons, greater than k,that have a distance less than ϵ. I can add the cluster in a list;
- for each cluster I calculate the mean direction (ra, dec), the time-interval (tstart, tstop), the duration and the number of its events.

I used k as the minimum number of photons to constitute a cluster, ϵ as the cluster radius and t as the interval of analysis.

In Table 5.1 there are the selection criteria for the clustering analysis.

Cut Name	Value
Science tools version	10-01-01
Instrument Response Function	PASS8
E_{min}	50 GeV
E_{max}	2 TeV
T_{start} (MET)	239557417
T_{stop} (MET)	440748803
evclass	source
ABS (ROCKING ANGLE)	$< 52°$
Cluster Radius ϵ	0.3

Table 5.1: Selection criteria for the data to which the clustering analysis was applied. The number of the analysed events is 57813.

Clustering Algorithm: the Radius

The cluster radius ϵ was chosen based on the current Point Spread Function PSF. It detects the maximus distance between the selected photons and the other ones in the same cluster.

The *Fermi*-LAT Instrument Response Functions give a PSF of 0.12° at 100 GeV for a 68% containment radius and 0.5° for 95% (Ackermann et al. 2012 [8]). In my analysis I investigated a radius within these values.

At the beginning, a radius of 0.5° was used for a preliminary search of the clusters. Later, considering the proper functioning of the algorithm of clustering, the search was confined to a radius of 0.3°. I decided to use a radius equal to two times the PSF, namely to consider the events within a distance of 2σ as coming from the same point source.

In Figure 5.1 you can see an example of a cluster. In this analysis I have used a space and time analysis with a sliding window of a week. The graph shows the position of the photons into the cluster. You can compare the Point Spread Function and the radius, that it was used like a maximum distance between the events that belong to the cluster. In the comparison with the 2FHL catalog, I find that this source is the famous Markarian 421 (Mrk 421). The Mkn 421 is a blazar located in the constellation Ursa Major. The object is an active galaxy and a BL Lacertae object, and it is a strong source of gamma rays. It is about 397 million light-years (redshift: z=0.0308 eq. 122Mpc) to 434 million light-years (133Mpc) from the Earth. It is one of the closest blazars to Earth, making it one of the brightest quasars in the night sky.

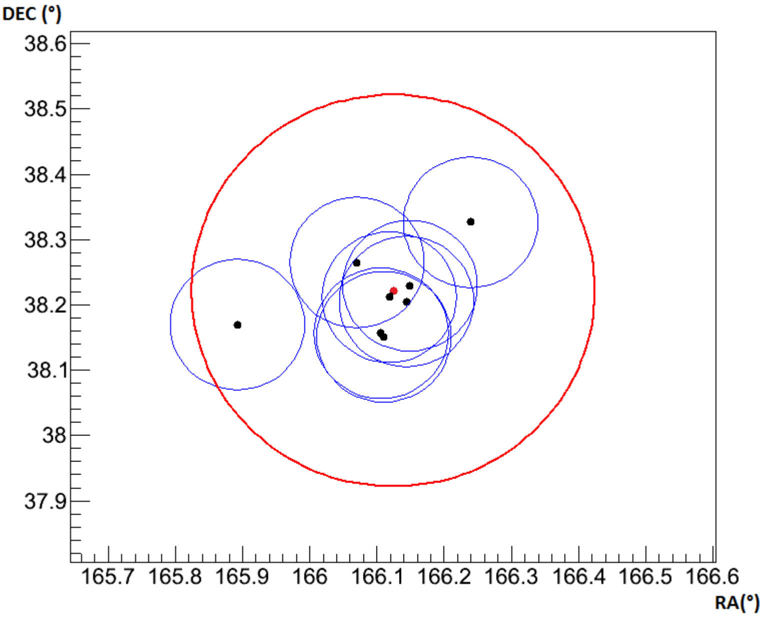

Figure 5.1: Cluster n° 196 of the space and time clustering analysis with a sliding window of a week (Cluster 196- number of events:9; T$_{start}(MET)$ =363575548 ; T$_{stop}(MET)$ =364132925; Duration:557376 s; Ra:166.08; Dec:38.19). This source is the important Markarian 421. The red circle represents the radius 0.3°, that it was used like a maximum distance to find the photons that belong to the cluster. The black points are the events and the blue circles around them indicate the Point Spread Function (PSF=0.15° at 50 GeV).

Clustering Algorithm: the Time Sliding Window

The aim of my research is to find new extragalactic sources and to observe the variation in the luminous flux of those ones already listed.

Imaging Atmospheric Cherenkov Telescopes (IACTs) allow to observe Active Galactic Nuclei (AGNs) in the high energy range with high sensitivity, similar at the Fermi-LAT observations. The TeV γ-ray observations of some blazars, detected in this energy range, reveal a rapid flux and a spectral variability on time scales of several hours or days.

For this reason I decided to take an interval of analysis, for the cluster's discovery, of one day and one week.

In a preliminary search was used an algorithm, with fixed bins, to control the operation of the programs. Subsequently, it is always used an algorithm of sliding windows. It performed the clustering analysis of a groups of events: from a selected one I take the follower photons that stay at most one week (or a day) from the considered event. This analysis was cyclically repeated for each sliding windows. The use of the sliding windows maximized the chances of finding a group of events coming from the same direction within a restricted period of time. The preliminary analysis, made by an algorithm with fixed bin-time, in fact, lost clusters with events that took place between an interval of analysis and the next one.

I would like to obtain clusters with a greater number of events in a narrow time-interval so as to restrict the emission and to have a greater probability for discovering the presence of a new source through the maximum likelihood method. In fact, the longer is the time-interval, the more is the the probability to observe, among the photons counted in the cluster, other photons caused by the galactic and extra-galactic background.

Clustering Algorithm: the Minimum Number of Events

In this analysis it was also essential to set a minimum number of events, in order to take into account the possibility that a set of events, enclosed the radius ϵ, was produced by a real source.

At gamma-ray energies, above 10 MeV, the analysis of diffuse emission becomes difficult, cause the accurate accounting for the Galactic diffuse emission. A precise analysis was adopted for the EGRET data. The extra-galactic intensity was then derived by a straight line fit to a plot of observed emission versus model prediction of Galactic emission (Sreekumar et al. 1998 [?]). The spectrum was determined to be consistent with a single power law of index (2.1 ± 0.03). The intensity above 100 MeV is $(1.45 \pm 0.05) \cdot 10^{-5}$ cm^{-2} sec^{-1} sr^{-1}, may include some unaccounted extended Galactic diffuse emission. The spectrum derived by Sreekumar et al. (1998) is also shown in Figure 5.1.

Another simple way, for understanding which is the maximum value of the expected background, is to consider the observed photons carried out by the galactic and extragalactic diffuse emission, so that they have an uniform distribution. Knowing the value of the radius ϵ, you can estimate the value of k (the minimum number of photons to create a cluster). The number of circles of radius $\epsilon = 0.3°$ that you can be traced on the celestial sphere is

$$N_{circles} = 4\pi \cdot \frac{1}{\epsilon^2 \cdot \pi} = 145903.8 \tag{5.1}$$

Assuming all the photons considered (whose number is $N_{photons} = 57813$) are coming from the background, the mean rate of arrival from each circle

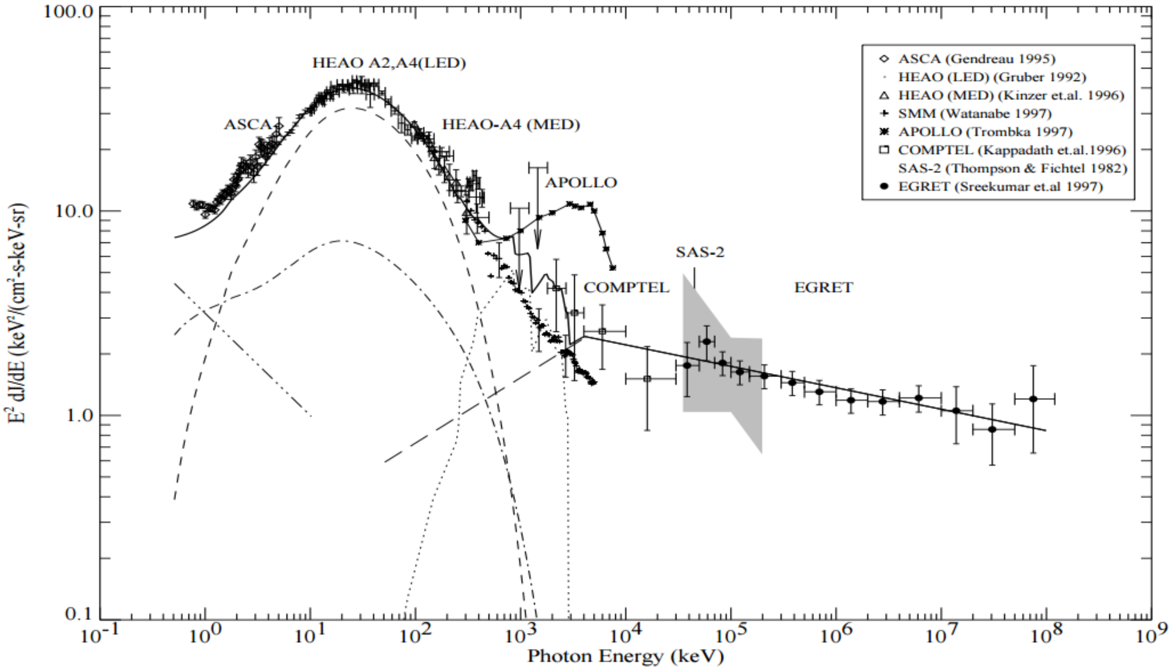

Figure 5.2: Multi-wavelength spectrum of the diffuse extragalactic emission from X-rays to gamma-rays taken from Sreekumar et al. (1997) [47].

of radius $\epsilon = 0.3°$, in the whole *Fermi*-LAT observed time period, is

$$\lambda = \frac{N_{circles}}{N_{photons}} = 2.5237 \tag{5.2}$$

The expected background distribution is the Poisson one with a mean equal to λ:

$$P(k) = \lambda^k \cdot \frac{e^{-\lambda}}{k!} \tag{5.3}$$

The probabilities to find k random photons from the background inside the same circle of radius ϵ, in 78 months, were calculated:

$$k = 2 \; \lambda^2 \cdot \frac{e^{-\lambda}}{2!} = 0.25 \tag{5.4}$$

$$k = 3 \; \lambda^3 \cdot \frac{e^{-\lambda}}{3!} = 0.21 \tag{5.5}$$

You can see that, even for the whole *Fermi*-LAT observed period, the probability to find two or three photons from the background in the same cluster, is less than 25%. By the sliding window analysis, using a time period of a day or a week, the number of expected background photons is 0.007, for a week process, and 0.001, for a day one. The probability to find more than one background photon in a cluster is extremely little.

Therefore, it seemed like good choice to take $k = 2$ and $k = 3$ as the minimum number of photons for each cluster ($< 10^{-5}\%$).

5.2 Python Scripts

For my analysis I used a SLAC's account [1] to access at the *Fermi* Science Tools. I wrote some python scripts: to find the clusters, to compare the list with the 2FHL catalog and to to perform the likelihood analysis. I also utilized some scripts, written for the GRB-analysis, to measure now the distance between the photons and to calculate some clusters parameters like mean direction, start-time. stop-time, duration and size.

The control program for the analysis is *test-50GeV.py.* It takes the duration of the sliding window interval Δ_T, the radius of the cluster ϵ, the location and the name of the output files and passes the information to the script *BlindSearch.py.* This script have four purposes:

- it subdivides, for the sliding window, the whole events' sample in a various sets that it stars from a selected photon and it contains the following ones that stay inside a week (or a day);
- it executes the clustering analysis for every set. It recalls the script *EventsCluster.py* to find the clusters;
- it cancels the identical clusters that were found for a consecutive intervals of analysis;
- it makes a list with the whole clusters and their properties;
- it draws the plot about every cluster and their general properties.

The first program that I modified and used for my analysis is *EventCluster.py.* It finds the clusters and returns their mean-direction (RA,DEC), time-start, time-stop, duration and size.

Its principal functions are:

- Find-cluster: it calculates for each photon the distance among the other ones and it appends in a list the clusters and their photons;
- Cluster-sizes: it returns the number of photons into the cluster;
- Mean-dir: it estimates the mean direction of the cluster;
- Dist-cluster: it measures the distance between two clusters;

---

[1] http://www.slac.stanford.edu/comp/unix/public-machines.html

- localize: it finds the clusters around a specified direction.

The coordinate of the clusters are calculated like a weighted average based on the energy of the photons.

$$DEC_{clust} = \frac{\Sigma DEC_i \cdot E_i}{\Sigma E_i} \tag{5.6}$$

where RA_i is the declination angle and E_i is the energy of the i-photon.

5.2.1 Compare to the 2FHL catalog

To test the main accuracy of the programs, at the end of the clustering analysis, I compared the obtained clusters' list of the whole period (78 months) with the 2FHL catalog that contains all the high-energy sources observed in the first 80 months by the *Fermi*-LAT.

I created a python script that controls, for each 2FHL source, if there is a cluster in that position. I used a strength tolerance radius of $\Delta_R = 0.3°$ to check the position of the catalogued source with the mean direction of the cluster, only if the distance between them is less than 0.3°, I considered that the same source was found in the process. The choice of the radius was performed comparing the Point Spread Function (0.15°), that it is connected to the errors in the mean direction of the clusters, and the maximum error in the source position in the 2FHL catalog (0.14°).

After the analysis check, in the same way, I used the list obtained from the sliding window analysis of a week (and a day) to compare it with the 2FHL catalog. The aim of this comparison is to see if there are candidates for new high energy sources.

I also used, to make the plots and a preliminary comparison between the clusters' list and the sources of the 2FHL catalog, the TOPCAT program. TOPCAT is an interactive graphical viewer and editor for tabular data. Its aim is to provide a lots of facilities that astronomers need for analysing and manipulating source catalogues and other tables, though it can be used for non-astronomical data as well. It understands a number of different astronomically important formats (including FITS, VOTable and CDF) and more formats can be added.

In Figure 5.2.1 you can see that almost the sources, contained in the 2FHL catalog, are detected in the clustering analysis in the whole period observed by *Fermi*-LAT.

In the plot you can see that there are a lot of detected clusters in the Galactic plane. This is caused by the considerable Galactic diffuse emission during the six years of observation. There is a great probability to observe three or more photons in a circle of radius 0.3° around the Galactic plane during the six years. Instead, outside the Galactic plane the Extra-galactic Background Light (EBL) is lesser than the Galactic ones.

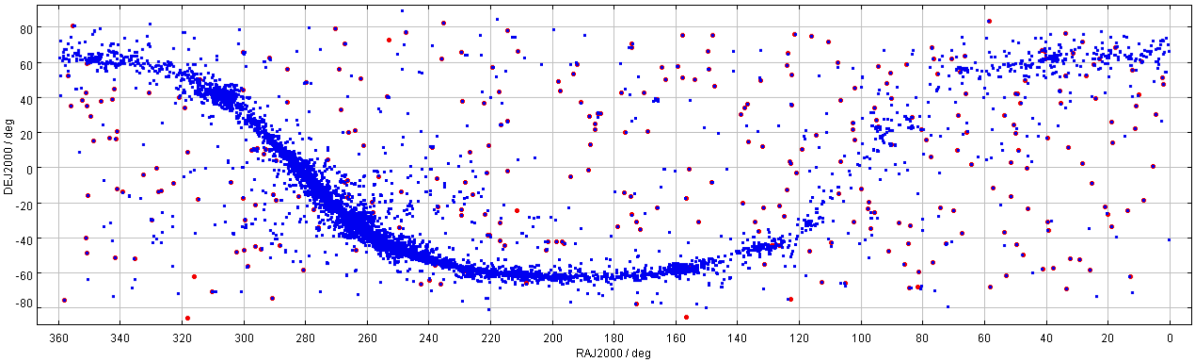

Figure 5.3: Plot of the celestial sources detected in the 2FHL catalog (red-point) and the cluster detected with an analysis of the whole period observed by *Fermi*-LAT (blu-point). The 2FHL catalog contains 360 high energy sources. The number of clusters detected in the first 78 months of *Fermi*-LAT observation is 12204, most of the clusters stay in the Galactic plane and they are produced by the galactic diffuse emission.

There are some 2FHL sources (5 over 360) that don't match with a cluster. I suppose that it is caused by the analysis method. While I used a clustering analysis method, in the 2FHL catalog it was directly performed the likelihood analysis. It compared directly the photons flux with the near sources and diffuse emissions. The 2FHL source were preliminary identified via a sliding-cell algorithm as excesses above the background.

5.3 *Fermi Tools* Likelihood Analysis

To analyse every singular cluster, I used the Unbinned Likelihood Analysis. It is the preferred method for time series analysis of the LAT data, where the number of events in each time bin is expected to be small. I wrote a python script that use the *Science Tools* to perform the analysis.[2] For this study I used the *`ft1-50GeV_p8_NOrockCut.fits`*[3] event data file, the *allsky-446373057-ft2-30s.fits* spacecraft data file (also referred to as the 'pointing and livetime history' file), and the current background models (`gll_iem_v06.fits` and *`iso_P8R2_SOURCE_V6_v06.txt`*). The Unbinned Likelihood analysis consists in this steps:

- Make sub-selections from the Event Data: it is useful to filter out any events that are not within the extraction region used for the analysis. For each cluster, that it is taken from the cluster list, a set of selection data was used in the selection analysis (see table 5.2).

---

[2] http://fermi.gsfc.nasa.gov/ssc/data/analysis/scitools/python-tutorial.html

[3] /afs/slac.stanford.edu/u/gl/principe/`ft1-50GeV_p8_NOrockCut.fits`

- Make Counts Maps from the Event Files: by making simple FITS images you can inspect our data and pick out obvious sources. I create a counts map of the ROI, summed over photon energies, in order to identify candidate sources and to ensure that the field looks sensible as a simple sanity check.

- Create a Source Model XML File: the source model XML file contains the various sources and their model parameters to be fit using the *gtlike* tool.

- Compute the diffuse responses: Each event must have a separate response precomputed for each diffuse component in the source model.

- Make an Exposure Map: this is needed in order to analyse diffuse sources, and derive absolute fluxes. The type of exposure map used by Likelihood differs significantly from the usual notion of exposure maps, which are essentially integrals of effective area over time. The exposure calculation that Likelihood uses consists of an integral of the total response over the entire ROI.

  There are two tools needed for generating exposure maps. The first is *gtlcube*. This tool creates a livetime-cube, which is a HealPix table, covering the full sky, of the integrated livetime as a function of inclination with respect to the LAT z-axis. The tool *gtexpmap* creates an exposure map based on the event selection used on the input photon file and the livetime cube. The exposure map must be recalculated if the ROI, zenith, energy selection or the time interval selection of the events is changed.

- Perform the Likelihood Fit: fitting the data to the model provides flux, errors, spectral indices, and other information.

- Make Test-Statistic Maps: these are used for point source localization and for finding weaker sources after the stronger sources have been modelled.

For each cluster, that it is taken from the cluster list, a set of selection data was used in the selection analysis (see table 5.2).

For the creation of the model I took and modified the *make3FGLxml.py* script. At the beginning it created models using the 3FGL catalog, so I modified it to use the 2FHL catalog, because it contains more high energy sources (>50 GeV) than the 3FGL.

I used the *gtfindsrc* tool to determine the correct position of the source. I took, as a trial for new HE sources, a TS greater than 25, like it is usually used in the other *Fermi*-LAT catalogs.

Parameter	Value
Search Center	(RA, DEC)
Radius	5°
Start Time (MET)	Time of the cluster's first photon
Stop Time (MET)	Time of the cluster's last photon
Minimum Energy	50 GeV
Maximum Energy	2 TeV
Event Class	SOURCE
Maximum Zenith Angle	100°

Table 5.2: Selection data for the Unbinned Likelihood Analysis. The choice to use a radius of 5 degree is due by the intention to focus the analysis in a restrict area around the cluster to discover if it is a celestial source.

Chapter 6

Clustering Results

In this chapter there are the results of the space and time clustering analysis. The first section contains the general results and the plots of the detected clusters. In this part you can find the details of the comparison with the 2FHL catalog. The second section contains the candidates for a new high energy sources. In particular two significant sources are described. The section three focuses on the flare phenomena that were observed in the sliding window process. Especially there are two paragraphs that illustrate the time analysis of the Crab Nebula and the Markarian 421.

The last section is dedicated to the conclusions and the outlook of my thesis' work.

6.1 Sliding Window Results

In this part there are the general results of the space and time clustering. I performed four sliding window clustering analysis, each one with different interval of analysis or minimum number of photons per cluster. I used for the analysis' interval a week or a day. For each analysis, as I already presented in the precedent chapter, I took as minimum number of photons within the cluster 2 and 3 photons.

The table 6.1 contains the summary results of the sliding window analysis. The complete list of the detected clusters is in the appendix 6.4. You can see in the table that there are some clusters that didn't find an associated source in the 2FHL catalog. These sources are excellent candidates for new high energy sources.

Figures 6.1-6.1-6.1-6.1, present the detected clusters (red circle) and the 2FHL sources (blue points), in order to easily see the correspondence between some of them. As expected, the most part of the clusters is detected around the Galactic plane. Furthermore the number of them increase with the duration of the interval of analysis. In the plots 6.1,6.1, you can see as green crosses the clusters that weren't found in the 2FHL catalog. These

File-Name	bin-time	Minimum ph.	N clusters	Not in the 2FHL
slid1dayclmin3	1day	3	22	1
slid1dayclmin2	1day	2	239	54
slid1weekclmin3	1week	3	408	7
slid1weekclmin2	1week	2	1505	382
listallperiod	78 months	3	12204	-

Table 6.1: General data of the sliding window clustering. For a comparison, in the last line there is the result of the analysis in the first 78 months observed by LAT.

clusters were processed with the Unbinned Likelihood analysis to study their characteristics.

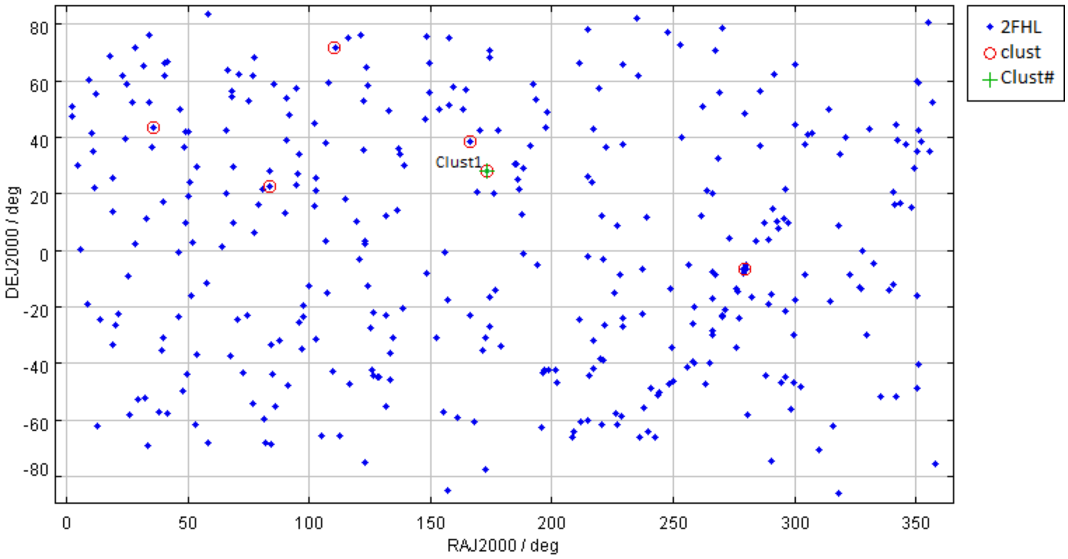

Figure 6.1: Plot of the detected clusters with a bin-time of a day and three minimum photons per cluster. The red points are the clusters and the blue ones are the 2FHL sources. The green cross represents the cluster that didn't find an association in the 2FHL catalog.

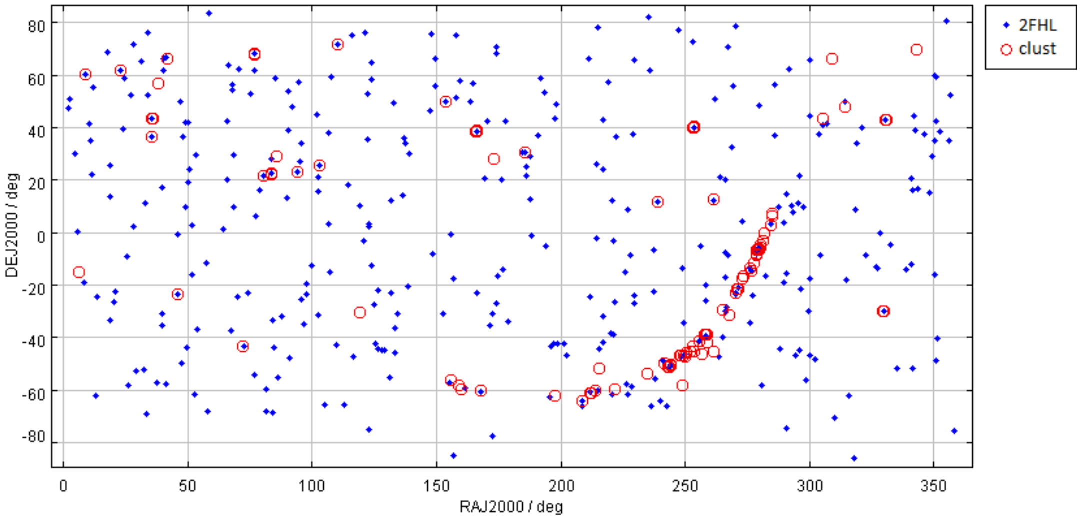

Figure 6.2: Plot of the detected clusters with a bin-time of a day and two minimum photons per cluster. The red points are the clusters and the blue ones are the 2FHL sources.

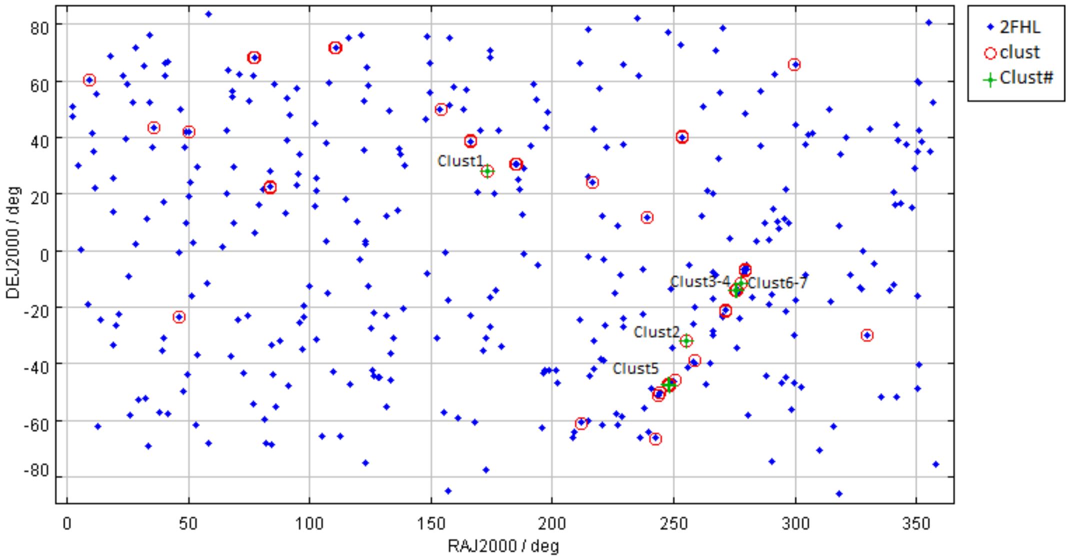

Figure 6.3: Plot of the detected clusters with a bin-time of a week and three minimum photons per cluster. The red points are the clusters and the blue ones are the 2FHL sources. The green crosses represent the clusters that didn't find an association in the 2FHL catalog.

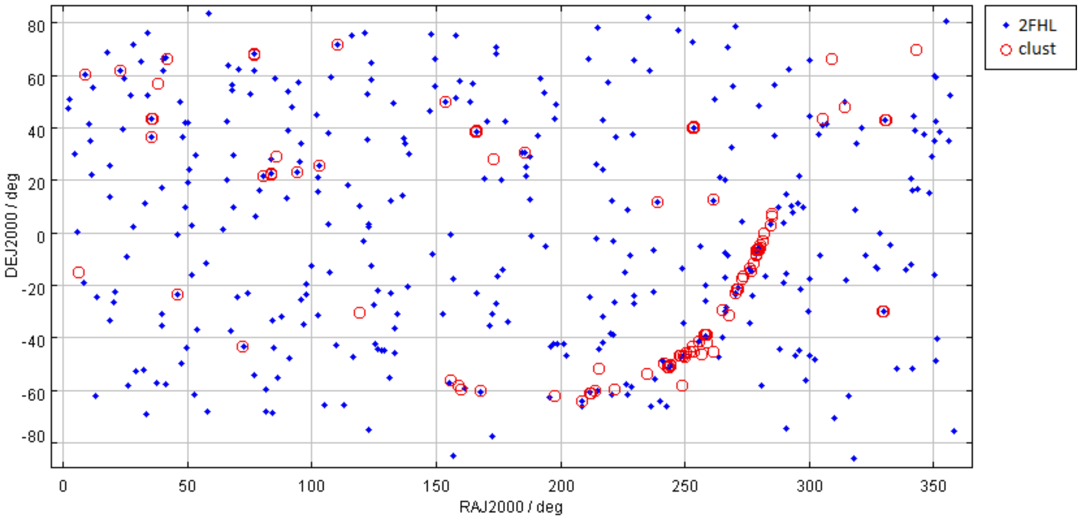

Figure 6.4: Plot of the detected clusters with a bin-time of a day and two minimum photons per cluster. The red points are the clusters and the blue ones are the 2FHL sources.

6.2 New High Energy sources

As you can see in table 6.1, in my analysis I found a lot of new little clusters that contain at least two or three photons. A likelihood analysis with only two photons risks to lose its statistical significance. If you would estimate the Test Statistic (TS) of this cluster, you could find that the most of them have a $TS > 25$, but it isn't acceptable to consider a results of fit with only two points. For this reason I restricted the Unbinned Likelihood analysis only to the clusters with at least three photons.

In the appendix you can find a table with the list of all clusters detected in the sliding window analysis of a week, with at least three photons per cluster. Here I show the likelihood analysis of the seven clusters that didn't appear in the 2FHL catalog. You can see in Table **??** the list of this sources' candidates. The interval of the sliding window is one week. The minimum number of photons per cluster is 3. The Test Statistic (TS), Index, Flux e LogLikelihood (LogLike) were found using the Unbinned Likelihood analysis with a fit quality of 3. The first two sources are those ones that were found significative (TS>25).

The Clust1 and Clust2 are two new sources detected with a Test Statistic more than 25. This two sources are described in the following paragraphs.

The other clusters (Clust3, Clust4, Clust5, Clust6, Clust7) are inside the Galactic plane, so they are more influenced by the Galactic diffuse emission than the first two clusters. This could be a possible explanation for their TS less than 25.

ID	RA°	DEC°	Err°	Gal-Long	Gal-Lat	T_{start} (MET)	T_{stop} (MET)	Flux (10^{-9})	Index	TS	-LogLike
Clust1	173.17	27.66	0.05	206.63	72.53	388741648	388741886	577.36±471.76	0.38 ± 0.24	75.521	29.081
Clust2	255.47	-32.44	0.15	351.81	5.80	432722981	433163412	2.24±1.38	1.60 ± 0.11	28.298	48.899
Clust3	275.73	-14.59	0.08	16.73	-0.46	310830210	311156398	4.87±3.10	1.46 ± 0.11	17.923	48.050
Clust4	275.73	-14.61	0.12	16.72	-0.47	310985110	311465961	3.72±2.36	1.51 ± 0.11	20.595	105.050
Clust5	248.17	-48.10	0.03	336.24	-0.062	399791310	400317426	4.53±2.70	1.32 ± 0.60	21.757	88.464
Clust6	277.35	-11.70	0.44	20.03	-0.51	414650623	415102803	4.08±2.14	1.49 ± 0.09	20.591	145.077
Clust7	277.35	-11.70	0.27	20.02	-0.50	429404818	429677845	2.68±1.90	1.56 ± 0.12	15.107	146.974
Clust3-4	275.73	-14.60	0.08	16.73	-0.46	310830210	311465961	3.39±1.95	1.52 ± 0.10	21.554	123.60

Table 6.2: Results for the clusters detected in the energy range between 50 GeV and 2 TeV, that weren't find in the 2FHL catalog.

The Clust6 and Clust7 are coming from the same direction but they were observed in two different periods that are distant between themselves above 5 months. The Clust6 was detected from the 21st to the 27th February 2014. Instead the Clust7 was detected from the 10th to the 16th of August 2014.

The Clust3,Clust4 come also from the same direction, but they belong to two adjacent periods that are in part overlapped. I found them, as two different clusters, because there are 4 photons into an interval of time longer than a week (1 week and 4 hours). The program created two separated clusters.

In a following analysis I studied the Clust3-Clust4 position using a period from the T_{start} of the first cluster to the T_{stop} of the second one, in order to test the whole period with the two detected clusters. In the last line of the table 6.4 (Clust3-4) there are the results of this analysis.

6.2.1 Discovery of new HE sources

Thanks to the sliding window clustering analysis I found two new significant (that have a TS>25) sources. The first of them is the famous GRB 130427A. It was observed on 27 April 2013. This source presents a great emission in a short periods of time. The cluster duration is less than 4 minutes (237 s). If the first new sources is far from the Galactic plane, the second one is near it (Galactic Latitude = 5.80).

Clust1: the GRB 130427A GRB 130427A was a record-setting gamma-ray burst, discovered starting on April 27th, 2013. This GRB was associated to SN 2013cq. Its optical signal was predicted on 2 May 2013 and detected on 13 May 2013.

The observations of the exceptional bright gamma-ray burst (GRB)130427A by the Large Area Telescope on board the *Fermi* Fermi satellite, provide constraints on the nature of such unique astrophysical sources. GRB 130427A had the largest flux, highest-energy photon (95 GeV), longest γ-ray duration (20 hours), and one of the largest isotropic energy releases ever observed from a GRB. The GeV emission from the burst lasted for hours, and it remained detectable by the LAT for the better part of a day, setting a new record for the longest gamma-ray emission from a GRB. Temporal and spectral analyses of GRB 130427A challenge the widely accepted model that the non-thermal high-energy emission in the afterglow phase of GRBs is synchrotron emission radiated by electrons accelerated at an external shock. [1].

It was simultaneously detected by the Burst Alert Telescope aboard the Swift telescope and was one of the brightest bursts Swift had ever detected.

---

[1] arXiv:1311.5623v2 [astro-ph.HE] 9 Dec 2013

It was one of the five closest GRBs, at about 3.6 billion light-years away, and was comparatively long-lasting.

In my analysis, above 50 GeV, I observed three photons, from this GRB, in a period less than 4 minutes. In Figure 6.2.1 you can see the detected events of the GRB 130427A.

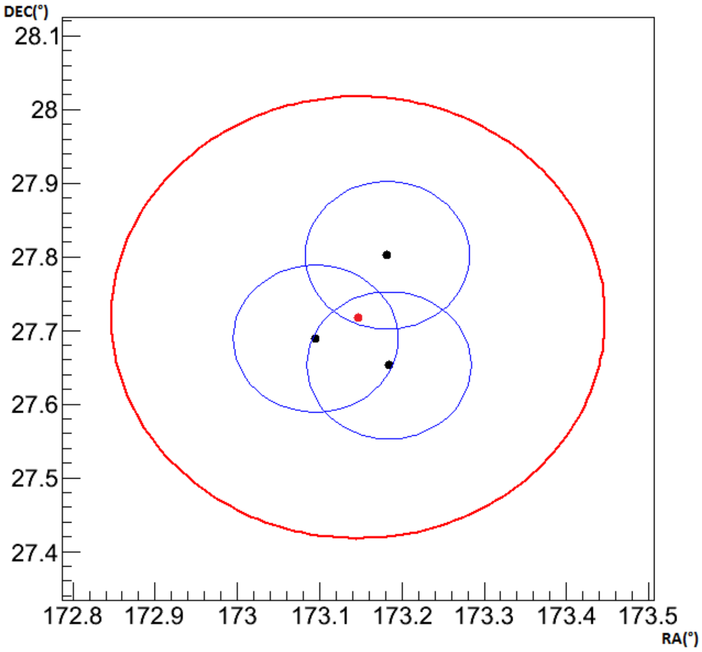

Figure 6.5: Plot of the GRB 130427A cluster (Clust1), detected by *Fermi*-LAT, in the energy range between 50 GeV and 2 TeV.

In Figure 6.2.1 you can see the GRB 130427A observations simultaneously in the Gamma Ray Burst and Large Area Telescope. In particular you can observe, in the last layer (LAT), two photons that belong at the Clust1. The third photon of the Clust1 is absent in the graph, because the picture's period of time is only 30 seconds. Instead it is distant 237 seconds from the first one.

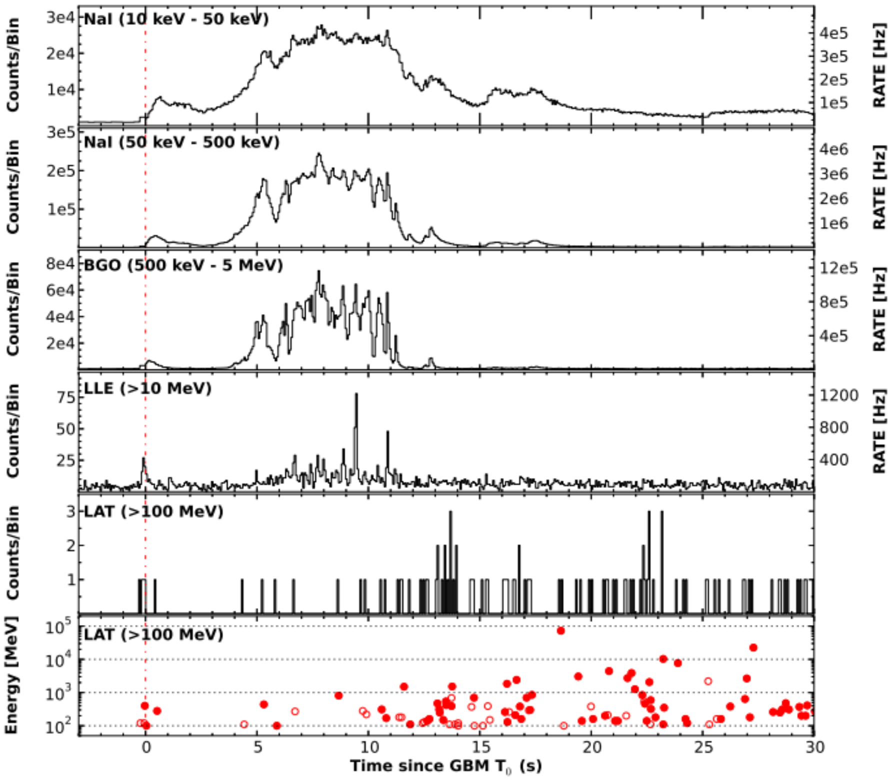

Figure 6.6: Light curves for the *Fermi*-GBM and LAT detectors during the brightest part of the emission in 0.064-s bins, divided into five energy ranges. The NaI and BGO light curves were created from a type of GBM data. The open circles in the bottom panel represent the individual LAT γ *Transient* class photons and their energies, and the filled circles indicate photons with a >0.9 probability of being associated with this burst. (arXiv:1311.5623v2)

The Clust2 The Clust2 stays near the band of the Galactic plane (Galactic Latitude 5.80). It doesn't find an associated source in the other gamma-ray catalogs. In Figure 6.2.1 you can see the observed photons of the Clust2.

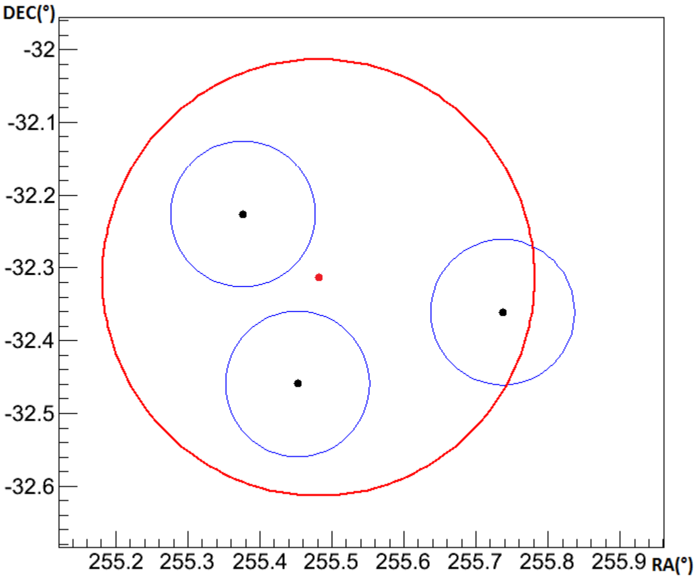

Figure 6.7: Plot of the photons that belonged at the Clust2 , detected by *Fermi*-LAT, in the energy range between 50 GeV and 2 TeV.

6.3 Flare phenomena: Mkn 421 and Crab Nebula

An important result from the space and time analysis is the possibility to observe the temporal variation of the sources' flux. This section contains the result coming from the clustering analysis with a slinding window of a week and three minimum photons per cluster.

In Figure 6.3 you can see the time-distribution of the resulting clusters. In particular you can see that there are some time's intervals in which were detected a lot of them. The flare phenomena of the Markarian 421 and Crab Nebula produced the most part of these data. The Markarian 421 and the Crab Nebula are the sources that appear almost among the detected clusters. For this reason they are the best candidates to observe their flare phenomena.

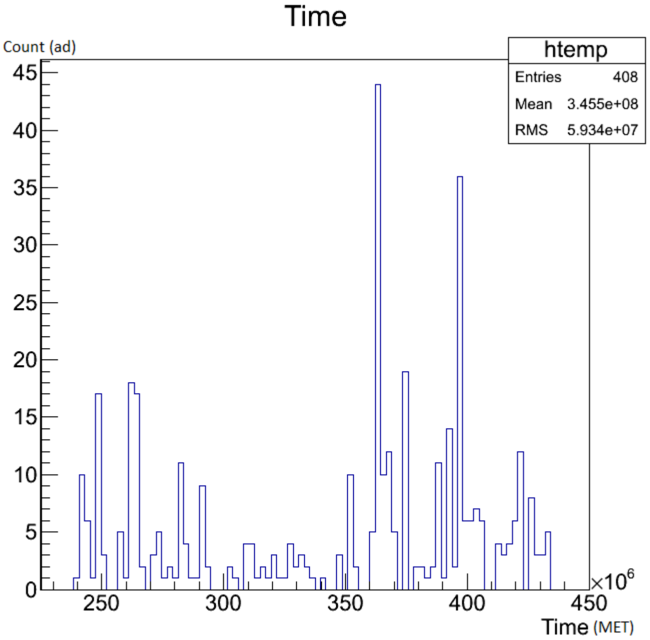

Figure 6.8: Graph of the detected cluster's time-distribution. In the x-axis there is the T_{start} (MET) of the clusters.

The Crab Nebula

The Crab Nebula is a supernova remnant and pulsar wind nebula in the constellation of Taurus. At the center of the nebula lies the Crab Pulsar, a neutron star 28–30 kilometres across with a spin rate of 30.2 times per second, which emits pulses of radiation from gamma rays to radio waves. At X-ray and gamma-ray energies above 30 keV, the Crab is generally the strongest persistent source in the sky, with measured flux extending to above 10 TeV.

In the analysis, I found 122 clusters caused by the Crab Nebula. Most of them are subgroups of the biggest ones. Therefore the Crab Nebula was observed 71 times.

Figure 6.3 presents the detected clusters that are associated at the Crab Nebula.

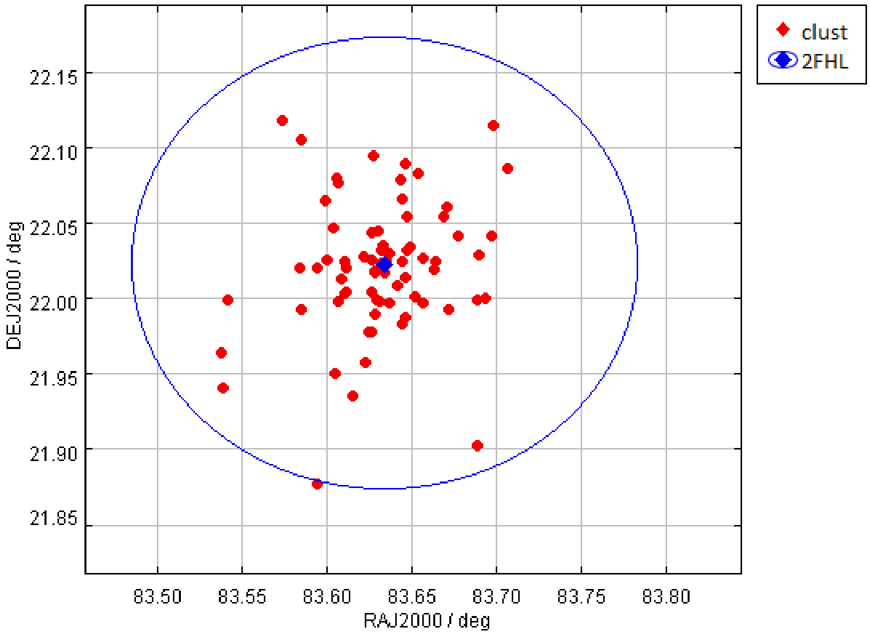

Figure 6.9: In this plot you can see the Crab Nebula. The red points are the detected clusters. The blue point is the position of the Crab Nebula founded in the 2FHL catalog. The blue circle represents roughly the area of the clusters that are associated to the Crab Nebula.

Figure 6.3 shows when the Crab Nebula was detected as a cluster in my analysis. You can see, in this plot, that the Crab Nebula regularly emits a large number of gamma-rays. Furthermore you can observe that the biggest number of photons, detected in a week by the *Fermi*-LAT, is six.

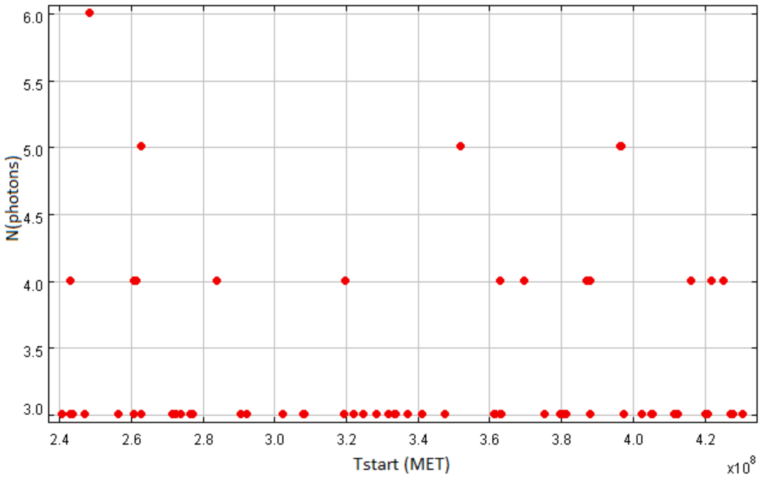

Figure 6.10: This graph shows when the Crab Nebula was detected as a cluster in the analysis. In the x-axis there is the T_{start} (MET) of the clusters.

6.3.1 The Markarian 421

The Mkn 421 is a blazar located in the constellation Ursa Major. The variability of the blazar Markarian 421 in TeV gamma rays over a 14-year time period were explored with the Whipple 10 m telescope. It was shown that the dynamic range of its flux variations is large and similar to that in X-rays. The peak energy response of the telescope was 400 GeV with 20% uncertainty.

In the analysis with time-bin of a week and three minimum photons per cluster I found 199 of them caused by the Markarian 421. The most of these are subgroups of the biggest ones. For this reason the Mkn 421 was observed only 58 times, in the sliding window analysis.

Figure 6.3.1 presents the detected clusters of the Markarian 421. Their colour depends from the number of photons inside them.

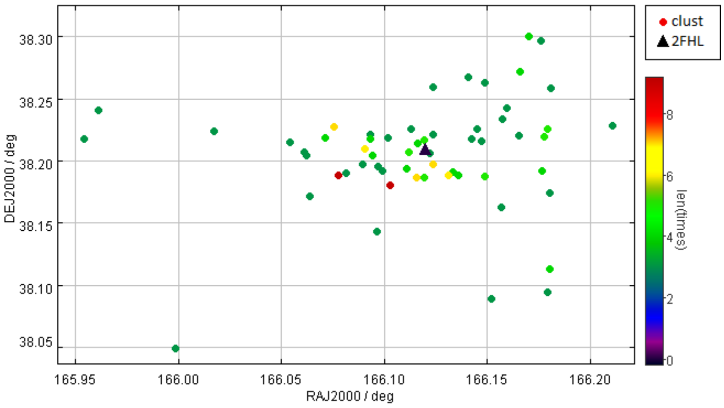

Figure 6.11: Graphic of the Mkn 421. The black triangle, in the plot, is the position of the Markarian 421. The other points are the detected clusters that are associated at the Mkn 421. Their colour depends from the number of photons inside them.

Figure 6.3.1 shows when the Mkn 421 was detected as a cluster in the analysis. You can see in this plot that the Markarian 421 didn't emit a large number of gamma-rays as Crab Nebula. There is a long period where the LAT didn't observe at least 3 photons in a week coming from the Mkn 421. This lack is normally caused by the fact that the MKn 421 emission is less than the Crab's one. The time-averaged flux from Markarian 421 over this period was 0.448±0.008 Crab flux units. The flux exceeded 10 Crab flux units on three separate occasions (Acciari et al. 2013). [2] In the graph, you can recognize this flare phenomena where the Mkn 421's flux exceed 10 Crab flux units (the three peaks). Furthermore you can observe in this plot

---

[2] Observation of Markarian 421 in TeV gamma rays over a 14-year time span, Acciari et al. 2013 [5]; arXiv:1310.8150v1 [astro-ph.HE]

that the biggest number of photons, detected in a week by the *Fermi*-LAT, is nine.

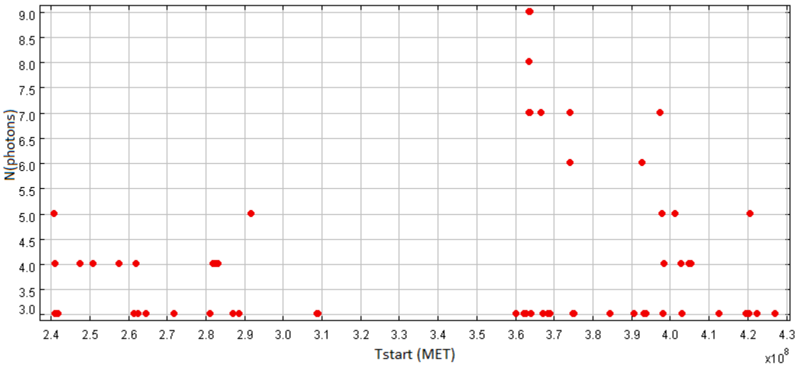

Figure 6.12: This graph shows when the Markarian 421 was detected as a cluster in the analysis. In the x-axis there is the T_{start} (MET) of the clusters.

6.4 Conclusions and Outlook

The study of the extragalactic sky at γ-ray energies has been revolutionized after the launch of the Fermi satellite. In particular, filling the gap in the MeV-GeV band, the LAT has promoted a remarkable impulse in the framework of the high-energy astrophysics phenomena, especially in blazars.

The first result of this thesis is about the investigation of the observed anisotropy of the BL LACs. I shed light on this observation, that it was in contrast with the cosmological principle. With a statistical analysis you can understand that there is only an apparent anisotropy caused by a lack in the optical observation in the southern hemisphere. The problem is that now there are a lot of unidentified blazars, the most in the southern hemisphere. In the near future, with the development of E-ELT, it is important to verify this hypothesis and check, if really the blazars distribution is uniform and homogeneous and if it respects the cosmological principle.

In the second part of my thesis I performed a space and time clustering analysis, that gave a lot of interesting results. The principal ones are the clusters' lists with a sliding window method of a day and a week. This list contains a lot of time information about the celestial sources. In particular I discovered 2 new high energy sources.

The next step of my analysis is to decrease the lower energy limit to 10 GeV. This decrease permits to increase the number of processed photons. It is important for producing the likelihood analysis. In my thesis I found a lot of little clusters that have only two photons. A likelihood test with only two photons risks to lose its statistical significance. This is also the explanation of why I restricted the Unbinned Likelihood only at the clusters with at least three photons. You can see in Table 6.1 that there are 54 clusters with only two photons, that weren't detected in the 2FHL catalog. If you would estimate the Test Statistic (TS) of these clusters, you could find that a lot of them have a $TS > 25$ but, it isn't reasonable to consider results of fit with only two points. In addition to the studied sources, in Table 6.4 are shown some source candidates detected in the energy range between 50 GeV to 2 TeV. They present a $TS > 25$, but they have only two photons, so I can't now consider them in the new sources search.

$N_{photons}$	T_{start} (MET)	T_{stop} (MET)	duration (s)	RA°	DEC°	TS
2	255179521	255226791	47268	308.59	65.92	44.657
2	382248517	382272877	24358	118.85	-30.76	30.310
2	396721265	396766623	45357	6.33	-15.37	54.867

Table 6.3: Three of the new high energy sources candidates, on which I tried to perform the likelihood analysis. In the future analysis, by an energy range between 50 GeV and 2 TeV, it will be interesting to check if, with more photons, these sources' candidates will be recognized as real new sources. These clusters have a time duration less than a day. The error in the RA and DEC coordinates is about 0.01 degree.

The next step for improving my work is to perform the likelihood at the whole detected clusters. In particular it is important to estimate, for each cluster, its energy flux and variability. This could be a brilliant space and time analysis to near the 2FHL catalog. If only a space test was performed to search the celestial objects in the 2FHL catalog, my thesis could describe also the variations of the sources' flux and the flare phenomena.

Thanks to my thesis work, it has been possible to expand the sources' catalog observed by *Fermi*-LAT, in the energy spectrum from 50 GeV to 2 TeV. Therefore I discovered two new high energy sources: the Clust1 (GRB 130427a) and the Clust2.

This energy band, used in the production of the 2FHL catalog, and in my analysis, coincides with that one observed by various Cherenkov telescopes.

In particular, in the near future, with the development of Cherenkov Telescope Array (CTA), and an improvement of a factor 5-10 in sensitivity in the 100 GeV-10 TeV range and an extended energy range both above and below these values, the simultaneous operation of ground-based and space facilities will continue the broadband γ-ray observation with unprecedented sensitivity. This will provide a guaranteed benefit to the AGN science.

The Cherenkov telescopes are yet affected by systematic intrinsic uncertainty, on the energy's scale and specific revealed flux, caused by the fact that they can not be calibrated in the laboratory, using known sources, which instead has been possible for the LAT. The results obtained in my analysis, together with 2FHL catalog, could be an important starting point for a possible calibration of Cherenkov telescopes by using the *Fermi*-LAT data (>50 GeV).

It is therefore to be of great importance to possess a good sources' catalog in those energies, in particular for a possible calibration of Cherenkov telescopes through the use of *Fermi*-LAT data (>50 GeV).

The improved capabilities in the detection and study of the celestial objects, using a space and time clustering, will allow a more detailed investigation of VHE emissions by galactic and extra-galactic sources, not only AGNs, and will not only increase our knowledge about the sources themselves, but will also be a valuable mean to deepen our knowledge of the Universe. In fact, AGN observations, and blazars in particular, have also been suggested as probes of other physical phenomena, such as the acceleration and propagation of ultra-high energy cosmic rays and more speculatively, the production of axion-like particles. All of this in addition to other field already explored nowadays, like providing constraints on the EBL and on the strength of the Intergalactic Magnetic Field (e.g. Ackermann et al., 2012 [8]).

Appedix

List of the clusters detected in the Sliding Window Clustering Analysis (1 week's interval of analysis and at least three photons for cluster)

ID	$N_{photons}$	T_{start} (MET)	T_{stop} (MET)	duration (s)	RA°	DEC°
1	3	240723290	240906664	183374	166,08	38,24
2	3	240583579	241122670	539091	83,64	22,08
3	4	240723290	240962847	239556	166,11	38,21
4	3	240675579	241191940	516361	83,57	22,12
5	5	240723290	241274502	551211	166,11	38,21
6	4	240872934	241274502	401567	166,12	38,20
7	5	240872934	241400146	527212	166,12	38,19
8	4	240906664	241400146	493482	166,12	38,17
9	3	240962847	241400146	437299	166,14	38,16
10	3	241274502	241761472	486970	166,10	38,14
11	3	241761472	242100633	339162	166,16	38,16
12	3	242896161	243170595	274435	83,63	22,00
13	3	243135883	243526032	390149	83,58	22,08
14	4	243135883	243635417	499534	83,60	22,06
15	3	243170595	243635417	464822	83,59	22,07
16	3	243526032	243801772	275739	83,61	22,08
17	3	244885386	245390050	504664	35,66	42,99
18	3	246916692	247306670	389978	83,63	22,02
19	3	247491564	247824307	332742	166,15	38,18
20	4	247491564	247893319	401754	166,14	38,19
21	3	247560851	247893319	332467	166,13	38,19
22	3	248281580	248528945	247365	83,64	22,05
23	4	248281580	248551265	269685	83,63	22,05
24	5	248281580	248769170	487590	83,63	22,05
25	6	248281580	248803894	522314	83,63	22,04
26	5	248408308	248803894	395587	83,63	22,04
27	6	248408308	248919209	510901	83,63	22,04
28	5	248528945	248919209	390264	83,62	22,04
29	4	248551265	248919209	367944	83,62	22,04
30	3	248769170	248919209	150039	83,62	22,04

ID	$N_{photons}$	T_{start} (MET)	T_{stop} (MET)	duration (s)	RA°	DEC°
31	3	248688192	248917559	229367	329,70	-30,26
32	4	248769170	249222373	453203	83,63	22,04
33	3	248803894	249222373	418479	83,62	22,03
34	3	248876310	249456986	580676	329,70	-30,26
35	3	248919209	249429261	510052	83,65	22,04
36	3	250916573	251203097	286524	166,06	38,22
37	4	250916573	251283381	366808	166,07	38,22
38	3	250916573	251283381	366808	166,07	38,18
39	3	256404942	256589652	184710	83,54	21,96
40	3	256503114	257098276	595162	83,54	21,94
41	3	257448860	257850756	401897	166,19	38,20
42	4	257448860	257932202	483342	166,18	38,19
43	3	257794598	257932202	137604	166,18	38,17
44	3	260615696	261034716	419020	83,67	21,99
45	3	260770135	261252202	482067	83,67	22,03
46	4	260770135	261321585	551450	83,65	22,03
47	3	261034716	261321585	286869	83,64	22,03
48	3	261252202	261739062	486859	83,63	22,02
49	4	261252202	261744737	492535	83,63	22,02
50	3	261321585	261744737	423152	83,63	22,02
51	3	261499986	261895934	395948	166,14	38,22
52	3	261739062	262135365	396304	83,58	21,90
53	3	261855832	262417621	561789	166,14	38,25
54	4	261855832	262440386	584554	166,17	38,27
55	3	261895934	262440386	544452	166,17	38,28
56	3	262417621	262926395	508774	166,18	38,30
57	3	262639595	262847301	207706	83,70	22,04
58	4	262639595	263092698	453103	83,70	22,03
59	5	262639595	263116811	477216	83,68	22,04
60	4	262835262	263116811	281549	83,64	22,03
61	5	262835262	263357263	522001	83,64	22,03
62	4	262847301	263357263	509962	83,63	22,03
63	3	263092698	263357263	264565	83,63	22,03
64	3	263149686	263682778	533092	35,63	43,01
65	4	263149686	263711785	562098	35,70	43,01
66	5	263149686	263718003	568317	35,69	43,02
67	6	263149686	263750637	600951	35,73	43,04
68	5	263407274	263750637	343364	35,74	43,04
69	6	263407274	263877627	470354	35,73	43,03
70	3	263474999	263663928	188929	253,46	39,82
71	5	263682778	263877627	194849	35,78	43,05
72	6	263682778	264119517	436739	35,75	43,07
73	7	263682778	264280090	597312	35,73	43,05
74	6	263711785	264280090	568306	35,74	43,05
75	5	263718003	264280090	562087	35,71	43,07
76	4	263750637	264280090	529453	35,71	43,07
77	3	263877627	264280090	402463	35,64	43,04
78	3	264144668	264547140	402472	243,72	-51,97
79	3	264597922	264804744	206822	166,18	38,26
80	3	265362143	265746293	384150	279,31	-6,91

ID	$N_{photons}$	T_{start} (MET)	T_{stop} (MET)	duration (s)	RA°	DEC°
81	3	265882458	266456342	573884	185,34	30,17
82	3	271450543	271898927	448384	83,66	22,02
83	3	271852870	272334904	482034	166,15	38,21
84	3	271898927	272316365	417437	83,61	22,00
85	3	272305290	272596769	291480	83,54	22,00
86	3	273445987	273961363	515375	76,99	67,64
87	4	273445987	274011104	565117	76,97	67,64
88	3	273850452	274011104	160652	76,96	67,64
89	3	273859577	274146093	286516	83,59	21,88
90	3	276384561	276613449	228888	83,66	22,00
91	3	277146644	277541587	394943	83,71	22,09
92	3	277736040	278194316	458277	77,05	67,61
93	3	279757164	280065420	308256	76,97	67,62
94	3	280951230	281282657	331427	166,18	38,17
95	3	281551174	281837702	286528	329,76	-30,24
96	3	281915246	282363038	447792	166,12	38,19
97	4	281915246	282386112	470866	166,11	38,19
98	3	282303611	282386112	82501	166,09	38,19
99	4	282303611	282627486	323874	166,09	38,20
100	3	282363038	282627486	264448	166,10	38,20
101	3	282954952	283517368	562416	250,31	-46,31
102	3	283175896	283675230	499334	166,05	38,24
103	4	283175896	283755771	579875	166,09	38,22
104	3	283179724	283597951	418227	329,74	-30,22
105	3	283453245	283755771	302526	166,16	38,20
106	3	283852567	284401882	549314	83,62	21,99
107	4	283852567	284415308	562741	83,65	21,99
108	3	283874412	284415308	540896	83,74	21,90
109	3	286973000	287432285	459286	166,10	38,19
110	3	288534045	289049838	515793	166,02	38,22
111	3	290368236	290877555	509319	83,65	22,09
112	3	291597437	292056602	459164	166,19	38,21
113	4	291597437	292056602	459164	166,18	38,22
114	5	291597437	292080122	482685	166,18	38,22
115	4	291597437	292080122	482685	166,19	38,22
116	4	291643513	292080122	436609	166,18	38,24
117	3	291643513	292080122	436609	166,19	38,23
118	3	291701765	292080122	378357	166,06	38,30
119	3	292043615	292479481	435865	83,67	22,05
120	3	292717429	293165659	448230	248,54	-47,97
121	3	294381276	294520577	139301	45,84	-24,12
122	3	301327597	301742078	414481	49,95	41,52
123	3	302338095	302544534	206439	83,65	22,05
124	3	304078765	304102121	23356	279,68	-6,97
125	3	307999324	308394244	394919	83,61	22,00
126	3	308176209	308613390	437181	83,59	22,02
127	3	308819439	309349590	530151	166,06	38,21
128	3	309072600	309485525	412925	166,05	38,21
129	3	310633217	310977831	344614	184,48	30,13
130	3	310830211	311156397	326187	275,71	-14,48

ID	$N_{photons}$	T_{start} (MET)	T_{stop} (MET)	duration (s)	RA°	DEC°
131	3	310985110	311465961	480850	275,78	-14,62
132	3	311410259	311928043	517785	35,67	43,03
133	3	313271032	313846717	575685	253,46	39,77
134	3	314965175	315566351	601176	271,41	-21,83
135	3	315187569	315763310	575741	248,15	-47,95
136	3	319177244	319537772	360528	83,63	21,98
137	3	319537599	319796568	258969	83,63	21,97
138	4	319537599	319876561	338962	83,62	21,98
139	3	319537772	319876561	338790	83,62	22,01
140	3	322159143	322606123	446980	83,63	22,09
141	3	324574440	325159932	585492	83,63	22,00
142	3	328188332	328280543	92211	253,47	39,70
143	3	328188332	328636432	448100	253,47	39,78
144	4	328188332	328636432	448100	253,48	39,75
145	3	328188332	328636432	448100	253,48	39,75
146	3	328257432	328636432	378999	253,49	39,76
147	3	328359131	328896426	537295	83,58	22,02
148	3	331620710	331998672	377962	83,63	21,99
149	3	331832294	332245663	413369	83,58	21,99
150	3	331998672	332566398	567726	83,62	22,01
151	3	333328095	333748537	420442	83,64	22,02
152	3	333672637	334000533	327896	83,63	22,02
153	3	337062927	337412162	349235	83,63	22,03
154	3	341128449	341689649	561200	83,65	22,03
155	3	347110745	347533506	422761	253,43	39,76
156	3	347469547	347916632	447085	83,67	22,06
157	3	347510529	347832429	321900	253,44	39,76
158	3	351685584	351996588	311004	83,65	21,96
159	4	351685584	352031550	345967	83,63	21,98
160	5	351685584	352203059	517475	83,64	21,98
161	4	351835837	352203059	367222	83,64	21,97
162	3	351996588	352203059	206471	83,64	22,00
163	3	352796838	353042267	245429	253,42	39,74
164	4	352796838	353060271	263433	253,43	39,74
165	3	352796838	353060271	263433	253,50	39,78
166	3	352926910	353060271	133361	253,39	39,71
167	4	352926910	353478329	551419	253,39	39,72
168	3	353042267	353478329	436062	253,35	39,71
169	3	353732023	354320843	588820	243,78	-51,87
170	3	359993555	360313800	320245	166,15	38,09
171	3	360202437	360739737	537301	253,56	39,74
172	3	361013309	361564174	550865	83,61	22,02
173	3	361031525	361169034	137509	250,43	-46,41
174	3	361540364	361825689	285325	83,63	22,02
175	3	362189508	362768010	578501	165,95	38,22
176	3	362756119	362859211	103093	165,96	38,24
177	3	362767216	363349867	582651	83,64	22,01
178	3	362898728	363413547	514819	83,66	22,01
179	4	362898728	363432166	533438	83,69	22,00
180	3	363349867	363432166	82299	83,69	22,00

ID	$N_{photons}$	T_{start} (MET)	T_{stop} (MET)	duration (s)	RA°	DEC°
181	3	363575548	363734691	159143	166,11	38,26
182	3	363619992	364061609	441616	166,17	38,27
183	3	363575548	364061609	486061	166,05	38,24
184	4	363575548	364061609	486061	166,10	38,26
185	5	363575548	364097029	521480	166,11	38,25
186	4	363575548	364097029	521480	166,07	38,23
187	6	363575548	364109173	533625	166,09	38,25
188	4	363619992	364097029	477036	166,16	38,26
189	6	363575548	364109173	533625	166,03	38,16
190	5	363575548	364109173	533625	166,05	38,22
191	6	363575548	364121307	545759	166,06	38,22
192	7	363575548	364121307	545759	166,09	38,24
193	5	363619992	364121307	501315	166,16	38,25
194	7	363575548	364121307	545759	166,04	38,17
195	8	363575548	364132925	557377	166,09	38,23
196	8	363575548	364132925	557377	166,05	38,16
197	9	363575548	364132925	557377	166,08	38,19
198	7	363575548	364132925	557377	166,07	38,21
199	7	363619992	364132925	512933	166,13	38,23
200	3	363878579	364132925	254346	166,00	38,05
201	7	363734691	364132925	398234	166,08	38,15
202	8	363619992	364132925	512933	166,10	38,18
203	6	363619992	364132925	512933	166,15	38,24
204	9	363619992	364223249	603256	166,10	38,18
205	8	363619992	364223249	603256	166,12	38,22
206	7	363619992	364223249	603256	166,14	38,23
207	7	363734691	364223249	488558	166,10	38,20
208	8	363734691	364223249	488558	166,08	38,16
209	4	363878579	364223249	344669	166,02	38,07
210	7	363878579	364223249	344669	166,06	38,13
211	6	364061609	364223249	161640	166,08	38,19
212	8	363878579	364429558	550979	166,06	38,14
213	5	363878579	364429558	550979	166,03	38,09
214	7	364061609	364429558	367949	166,08	38,19
215	6	364097029	364429558	332530	166,09	38,18
216	5	364109173	364429558	320385	166,07	38,18
217	4	364121307	364429558	308251	166,11	38,18
218	3	364132925	364429558	296633	166,10	38,16
219	3	364223249	364797466	574218	166,12	38,21
220	3	365196880	365759529	562649	166,20	38,14
221	4	365196880	365759529	562649	166,25	38,12
222	3	365199642	365759529	559887	166,27	38,12
223	3	365403897	365842388	438492	110,74	71,40
224	3	366280015	366526981	246966	166,08	38,19
225	4	366280015	366584324	304309	166,11	38,19
226	5	366280015	366653720	373704	166,11	38,19
227	4	366526852	366653720	126867	166,11	38,19
228	5	366526852	366951442	424589	166,13	38,20
229	7	366526852	366963964	437112	166,12	38,19
230	6	366526852	366962170	435318	166,13	38,19

ID	$N_{photons}$	T_{start} (MET)	T_{stop} (MET)	duration (s)	RA°	DEC°
231	5	366526981	366962170	435189	166,13	38,19
232	6	366526981	366963964	436983	166,11	38,18
233	3	366526981	366963964	436983	165,96	38,11
234	4	366584324	366962170	377846	166,15	38,20
235	5	366584324	366963964	379640	166,13	38,19
236	3	366653720	366962170	308451	166,19	38,21
237	4	366653720	366963964	310245	166,13	38,18
238	3	366803133	367232148	429015	211,85	-61,56
239	3	366951442	367460132	508691	166,21	38,23
240	3	368452187	368818527	366340	166,08	38,19
241	3	368818527	369302053	483525	166,06	38,17
242	3	368850301	369399369	549068	271,23	-21,66
243	3	369590736	369884131	293396	83,64	21,99
244	4	369590736	369964676	373940	83,64	22,00
245	3	369598405	369964676	366271	83,64	22,02
246	3	373598480	374126275	527795	166,17	38,17
247	3	373957748	374286684	328936	166,14	38,19
248	4	373957748	374451394	493645	166,14	38,19
249	5	373957748	374515175	557427	166,13	38,19
250	6	373957748	374550985	593237	166,13	38,19
251	5	374126275	374550985	424710	166,13	38,19
252	6	374126275	374692417	566142	166,13	38,19
253	7	374126275	374722236	595961	166,12	38,20
254	6	374286684	374722236	435552	166,09	38,22
255	7	374286684	374744931	458246	166,09	38,22
256	6	374451394	374744931	293537	166,08	38,22
257	5	374515175	374744931	229755	166,09	38,23
258	4	374550985	374744931	193945	166,09	38,22
259	3	374692417	374744931	52514	166,10	38,24
260	4	374692417	375191428	499011	166,15	38,25
261	3	374722236	375191428	469192	166,15	38,26
262	3	374744931	375341449	596519	166,14	38,22
263	3	375191428	375444741	253313	166,17	38,22
264	3	375288874	375550592	261717	83,60	21,95
265	3	379504289	380105311	601022	83,69	22,03
266	3	379823574	380374078	550504	83,65	22,04
267	3	380105311	380615873	510561	83,63	22,03
268	3	381355182	381612991	257809	83,62	21,93
269	3	382929247	383260584	331337	253,50	39,78
270	3	384501879	384867878	365999	166,12	38,26
271	3	386151125	386641718	490593	299,50	65,24
272	3	386928617	387134911	206294	83,61	22,02
273	4	386928617	387375175	446558	83,61	22,02
274	3	387055277	387375175	319898	83,68	22,02
275	3	387901318	388260030	358712	110,49	71,30
276	3	387810438	388212870	402433	83,63	22,02
277	4	387901318	388406032	504714	110,52	71,29
278	3	388131123	388648627	517503	83,64	22,01
279	4	388131123	388715288	584165	83,65	22,00
280	3	388200628	388406032	205404	110,52	71,28

ID	$N_{photons}$	T_{start} (MET)	T_{stop} (MET)	duration (s)	RA°	DEC°
281	3	388212870	388715288	502418	83,67	21,99
282	3	388741648	388741886	238	173,15	27,72
283	3	390618093	391076710	458617	166,12	38,20
284	3	391740113	391975094	234981	83,69	22,01
285	3	392573573	392656651	83078	166,08	38,21
286	4	392573573	392826174	252601	166,09	38,22
287	5	392573573	392897978	324405	166,09	38,21
288	6	392573573	393162469	588896	166,09	38,21
289	5	392596495	393162469	565975	166,12	38,20
290	4	392656651	393162469	505819	166,12	38,21
291	5	392656651	393214233	557582	166,11	38,21
292	6	392656651	393254340	597690	166,10	38,21
293	5	392826174	393254340	428166	166,09	38,21
294	3	392883458	393467806	584348	253,50	39,76
295	4	392897978	393254340	356363	166,08	38,20
296	3	393162469	393254340	91871	166,06	38,20
297	3	393214233	393799400	585167	166,12	38,22
298	3	393799400	393987835	188435	166,14	38,27
299	3	395306256	395787518	481262	242,47	-66,87
300	3	396174217	396655043	480825	83,56	21,99
301	4	396174217	396700263	526046	83,60	22,00
302	5	396174217	396723253	549035	83,61	22,01
303	4	396540690	396723253	182562	83,64	22,01
304	5	396540690	396854312	313622	83,65	22,01
305	3	396849718	397124397	274679	166,13	38,18
306	4	396655043	396854312	199270	83,66	22,03
307	3	396700263	396854312	154049	83,66	22,03
308	4	396849718	397219490	369772	166,13	38,18
309	5	396849718	397309899	460181	166,13	38,19
310	4	396932232	397309899	377667	166,12	38,18
311	4	397124397	397537804	413406	166,13	38,21
312	5	397124397	397665714	541317	166,09	38,23
313	4	397219490	397665714	446223	166,07	38,24
314	6	397219490	397746491	527001	166,07	38,21
315	5	397219490	397746491	527001	166,10	38,19
316	5	397219490	397746491	527001	166,07	38,24
317	7	397219490	397754790	535299	166,08	38,23
318	6	397219490	397754790	535299	166,07	38,25
319	6	397219490	397754790	535299	166,10	38,21
320	6	397309899	397754790	444891	166,07	38,24
321	5	397309899	397754790	444891	166,10	38,22
322	5	397309899	397754790	444891	166,06	38,26
323	4	397537804	397754790	216986	166,05	38,27
324	5	397537804	397754790	216986	166,06	38,24
325	4	397537804	397754790	216986	166,09	38,22
326	3	397450626	397690538	239912	83,60	22,05
327	6	397537804	398021132	483329	166,07	38,23
328	5	397537804	398021132	483329	166,10	38,21
329	5	397537804	398021132	483329	166,07	38,25
330	5	397665714	398021132	355419	166,06	38,23

ID	$N_{photons}$	T_{start} (MET)	T_{stop} (MET)	duration (s)	RA°	DEC°
331	4	397665714	398021132	355419	166,05	38,25
332	4	397744800	398021132	276333	166,10	38,20
333	5	397744800	398316731	571931	166,12	38,22
334	4	397746491	398316731	570240	166,12	38,24
335	3	397754790	398316731	561941	166,14	38,25
336	3	398021132	398408922	387790	166,16	38,24
337	3	398316731	398666038	349307	166,24	38,28
338	4	398316731	398917871	601140	166,17	38,30
339	3	398408922	398917871	508948	166,17	38,30
340	3	399036655	399482789	446134	258,55	-39,51
341	3	399791310	400317427	526116	248,23	-48,07
342	3	400414071	400849410	435338	216,79	23,72
343	3	401250380	401581758	331378	166,15	38,17
344	4	401250380	401674451	424071	166,15	38,18
345	5	401250380	401788486	538106	166,15	38,19
346	4	401448405	401788486	340082	166,15	38,20
347	3	401581758	401788486	206729	166,15	38,22
348	3	402613795	402955952	342157	166,19	38,09
349	3	402497136	403086004	588868	83,58	22,10
350	4	402613795	403094590	480795	166,18	38,11
351	3	402613795	403094590	480795	166,20	38,10
352	3	402613795	403094590	480795	166,13	38,20
353	3	402946020	403094590	148569	166,18	38,09
354	3	404707753	405213145	505392	166,14	38,18
355	4	404707753	405304562	596808	166,13	38,19
356	3	404994309	405445579	451270	83,62	22,03
357	3	405200628	405304562	103934	166,13	38,20
358	4	405200628	405703287	502660	166,12	38,21
359	3	405213145	405703287	490142	166,13	38,21
360	3	405251989	405732753	480764	83,60	22,02
361	3	411491357	411642578	151221	83,69	21,90
362	3	412427168	412748458	321290	166,09	38,22
363	3	412505607	413079709	574101	83,66	22,02
364	3	412872593	413417384	544791	153,87	49,42
365	3	414650624	415102803	452179	247,71	-47,91
366	3	416226573	416416327	189754	83,66	22,04
367	3	415914278	416225702	311424	253,44	39,70
368	4	416226573	416485181	258608	83,66	22,03
369	3	416256928	416485181	228253	83,66	22,02
370	3	416416327	416902402	486076	83,63	22,01
371	3	417318893	417575109	256216	253,46	39,88
372	3	419558572	419959454	400883	166,09	38,20
373	3	419580430	419661931	81501	110,41	71,22
374	3	419600977	420087801	486824	238,84	11,22
375	3	419948867	420373468	424601	166,10	38,19
376	3	420108009	420417135	309125	83,62	21,96
377	3	420373468	420910934	537466	166,10	38,22
378	3	420602871	421025451	422580	166,20	38,25
379	4	420602871	421106233	503361	166,18	38,22
380	5	420602871	421197671	594800	166,18	38,22

ID	$N_{photons}$	T_{start} (MET)	T_{stop} (MET)	duration (s)	RA°	DEC°
381	4	420910934	421197671	286738	166,19	38,21
382	3	420943832	421139182	195349	83,63	22,00
383	3	421025451	421197671	172220	166,20	38,22
384	3	421106233	421642965	536732	166,15	38,18
385	3	421825568	422386120	560552	83,61	21,98
386	4	421825568	422396770	571202	83,61	22,00
387	3	421872851	422432628	559777	9,11	59,85
388	3	422294671	422500481	205809	166,16	38,23
389	3	422318235	422396770	78534	83,63	22,01
390	3	425201124	425658316	457192	83,74	22,13
391	4	425201124	425669757	468632	83,70	22,11
392	3	425652021	425669757	17735	83,66	22,04
393	3	426271049	426680786	409737	243,97	-50,75
394	3	426515977	427115472	599494	244,29	-50,93
395	3	426680786	427194691	513905	244,30	-50,99
396	3	426965303	427428796	463492	166,11	38,22
397	3	427073303	427672883	599579	83,64	22,02
398	3	427513314	427986647	473333	83,64	22,07
399	3	427672883	428142338	469456	83,65	22,08
400	3	429404818	429677845	273026	277,49	-11,91
401	3	429754901	429982896	227994	253,63	39,70
402	3	430466360	431033634	567274	83,61	22,08
403	3	431180264	431629904	449640	279,29	-7,43
404	3	431933696	432219759	286064	253,35	39,72
405	3	432540316	433077218	536902	238,86	11,18
406	3	432722982	433163412	440430	255,48	-32,31
407	3	432826491	433368970	542479	248,27	-48,00
408	3	432826491	433368970	542479	248,27	-48,00

Table 6.4: List of all the clusters detected in the space and time clustering with a slinding window of a week and at least three photons per cluster.

Bibliography

[1] Abdo, A.A. and *et al. The on-orbit calibration of the Fermi Large Area Telescope*,2010, Astroparticle Physics, 32, 193. 0904.2226.

[2] Abramowski, A.,*et al.*, 2011, A&A, 533, A103.

[3] Abramowski, A.,*et al.*, *Discovery of gamma-ray emission from the extragalactic pulsar wind nebula N?157B with H.E.S.S.*, 2012, A&A, 545, L2.

[4] Abramowski, A.,*et al.*, . 2015, A&A, 574, A27.

[5] Acciari,*et al.*, *Observation of Markarian 421 in TeV gamma rays over a 14-year time span*,2013; arXiv:1310.8150v.

[6] Acero *et al. Fermi Large Area Telescope Third Source Catalog*, 2015, ArXiv:1501.02003

[7] Ackermann *et al. Fermi LAT Second AGN Catalog*, 2011, ApJ...743..171A

[8] Ackermann, M.,*et al.* 2012, Science, 338, 1190

[9] Ackermann *et al.*, *Fermi-LAT Observations of the Gamma-ray Burst GRB 130427A*, 2013, arXiv:1311.5623

[10] Ackermann *et al. Fermi Large Area Telescope Third Source Catalog*, April 2015, http://arxiv.org/abs/1501.02003v2

[11] Ackermann, *et al.*, *2FHL: The Second Catalog of Hard Fermi-LAT Sources*, August 2015, http://arxiv.org/abs/1508.04449v1

[12] Actis *et al. Design concepts for the Cherenkov Telescope Array CTA: an advanced facility for ground-based high-energy gamma-ray astronomy*, 2011, arXiv:1008.3703.

[13] Aharonian F.A *TeV gamma rays from BL Lac objects due to synchrotron radiation of extremely high energy protons*, New Astron. 2000, 5, 377. arXiv:astro-ph/0003159.

[14] Albert J.,*et al.*, *VHE γ-Ray Observation of the Crab Nebula and its Pulsar with the MAGIC Telescope*, Astrophys. J. 2008, 674, 1037. 0705.3244.

[15] Atwood W.B., *et al. Design and initial tests of the Trackerconverter of the Gamma-ray Large Area Space Telescope*, 2007, Astroparticle Physics, 28, 422.

[16] Atwood W.B., Abdo, Ackermann, *et al. The Large Area Telescope on the Fermi Gamma-Ray Space Tel Mission*, ApJ,697:1071-1102, June 2009. doi:10.1088/0004-637X/697/2/1071esope

[17] Atwood, *et al.*, *Pass 8: Toward the Full Realization of the Fermi-LAT Scientific Potential*,2013, arXiv:1303.3514

[18] Baldini L., *et al.*, *Preliminary results of the LAT Calibration Unit beam tests.*,2007, The First GLAST Symposium, volume 921 of American Institute of Physics Conference Series, pp. 190?204. (Cite

[19] Bradley. M Peterson, *An Introduction to Active Galactic Nuclei*, Cambridge University Press, 1997, pp. 1-25, 32-60, 67-74, 93-95, 110-112

[20] Breiman*et al.*, *Classi?cation and Regression Trees*, 1984.

[21] Buson Sara, *The TeV AGN Portfolio: extending Fermi-LAT analysis into the CTA realm*, January 2013,paduaresearch.cab.unipd.it/5909/

[22] Cambes F., P.Boissè, A. Mazure, A. Blanchard, *Galaxies and Cosmology*, A^eA library, Ed. Springer, 1995.

[23] Collin S. Czerny b., *Active Galactic Nuclei*, Encyclopedia of Life Support Systems 2004

[24] Condon J. J., Cotton, W. D., Greisen, E. W., Yin,Q. F., Perley, R. A., Taylor, G. B., & Broderick, J. J., *The NRAO VLA Sky Survey* 1998, AJ, 115, 1693

[25] Davis, J.E. *The Formal Underpinnings of the Response Functions Used in X-Ray Spectral Analysis.*, 2001, Astrophys. J., 548, 1010. arXiv:astro-ph/0011068.

[26] Dermer and Schlickeiser, *Model for the High-Energy Emission from Blazars*, October 1993, http://adsabs.harvard.edu/abs/1993ApJ...416..458D

[27] Dwek, E., & Krennrich, F., *http://www.sciencedirect.com/science/article/pii/S09276505120* 2013, Astroparticle Physics, 43, 112

[28] Dominguez and Ajello *Spectral Analysis at Very High Energy of Fermi-LAT 2FHL Blazars*, in preparation

[29] Fanaroff B.L.,and Riley J.M., *The morphology of extragalactic radio sources of high and low luminosity* MNRAS, 162:31P-36P, May 1974

[30] Fossati, G., *et al.*, *A unifying view of the spectral energy distributions of blazars*, 1998, Mon. Not. R. Astron. Soc., 299, 433. arXiv: astro-ph/9804103.

[31] Fossati, G., *et al.*, *Multiwavelength Observations of Markarian 421 in 2001 March:An Unprecedented View on the X-Ray/TeV Correlated Variability*, 2008, Astrophys. J., 677, 906. 0710.4138.

[32] Funk S. Hintonb A. for the CTA collaboration, *Comparison of Fermi-LAT and CTA in the region between 10-100 GeV*, 2008, Astrophys. J., 677, 906. 0710.4138.

[33] Ghisellini G., Tavecchio, F.,*The blazar sequence: a new perspective.*Mon. Not. R. Astron. Soc., 387, 1669. 0802.1918.

[34] Ghisellini G., Tavecchio, Foschini, Ghirlanda,*The transition between BL Lac objects and flat spectrum radio quasars* MNRAS, 414:2674-2689, July 2011,doi:10.1111/j.1365-2966.2011.18578.x

[35] Ghisellini G., *et al.*,*A theoretical unifying scheme for gamma-ray bright blazars.* Mon. Not. R. Astron. Soc., 301, 451. arXiv: astro-ph/9807317.

[36] Giommi, Padovani *et al.*, *A Simpli?ed View of Blazars: Clearing the Fog around Long-Standing Selection Effect*, 2012, doi:10.1111/j.1365-2966.2011.20044.x

[37] Malcolm S. Longer, *High Energy Astrophysics vol II*, Cambridge University Press, 1994,

[38] Manchester *et al.*, *The Australia Telescope National Facility Pulsar Catalogue*, 2005, DOI: 10.1086/428488.

[39] Massaro *et al.*, *Roma-BZCAT: a multifrequency catalogue of blazars*2009, A&A, 495, 691

[40] Mattox *et al.*, *The Likelihood Analysis of EGRET data*, April 1996, http://adsabs.harvard.edu/abs/1996ApJ...461..396M

[41] Mauch, T., Murphy, T., Buttery, H. J., Curran,J., Hunstead, R. W., Piestrzynski, B., Robertson,J. G., & Sadler, E. M. 2003, MNRAS, 342,1117

[42] Nolan *et al.*, *Fermi Large Area Telescope Second Source Catalog*,2012, ApJS, 199, 31

[43] Pacciani *et al.*, *Exploring the Blazar Zone in High Energy Flares of FRSQ*, June 2013, http://arxiv.org/abs/1312.3998v2

[44] Rando R. , PhD Thesis (2004), pp. 23-33.

[45] Scarpa R., Urry, Falomo R.,*et al.*,*The Hubble Space Telescope Survey of BL Lacertae Objects: Gravitational Lens Candidates and Other Unsual Sources* ApJ: 521:134-144, August 1999, doi:10.1086/307552

[46] Shaw,*et al.*,*Spectroscopy of the largest ever γ-ray selected BL LAC sample*, 2013, ApJ, 764, 135

[47] Sreekumar *et al.*, *The Extragalactic Diffuse Gamma-Ray Emission* ,1997, arXiv:astro-ph/9709258

[48] Urry C.M. Padovani P. *Unified Schemes for Radio-Loud Active Galactic Nuclei*, Phy. Rev. Lett. (Vol. 107), Pubblications of the Astronomical Society of the Pacific (1995).

http://fermi.gsfc.nasa.gov/ssc/ http://fermi.gsfc.nasa.gov/ssc/data/analysis/scitools/overvi
http://fermi.gsfc.nasa.gov/docs/software/ftools/ftools?menu.html